

INTRINSIC INFRARED RADIATION OF THE SEA SURFACE

C. Bourlier, J. Saillard, and G. Berginc

IRESTE-Laboratoire SEI/EP CNRS 2018

Rue C. Pauc

La Chantrerie -BP 60601

44306 Nantes Cedex 3

France

Prologue— The infrared contrast of ships at sea is of importance for those who want to detect, identify and achieve target acquisition and for those who want to protect to enhance target vessel's first strike capability and hence its survivability. Infrared signature control or stealth technology is changing the face of naval warfare and is rapidly becoming a key performance parameter in warship design. The infrared contrast is determined by a large number of parameters. Temperatures of the ship structure and the ambient sea and air are important. But the infrared and visible signature is due not only to target emissions but to the immediate target background. Infrared signature designs are driven by signature generation mechanisms and threat sensors characteristics. Definition of threat sensor types (operating bands, resolution capability) helps to focus infrared and visual signature control on the spectral regions and spatial dimensions of greatest interest. One of the more common divisions of the visual or infrared signature definition is the separation based on so-called imaging versus non-imaging sensors. Imaging sensors threats are represented by the human eye and aids such as televisions, FLIRs (forward-looking infrared) and image intensifiers. These threats possess the ability to resolve and process silhouette and internal target pattern detail. Non imaging sensors depend on target signal strength and background separation. Nonimaging sensor threat are represented by missile seekers,IRSTs (infrared search and track) and terminally guided submunitions. The more recent generation IR missile seeker threats use the 3 to 5 μm band, future threat seekers are likely to use imaging focal plane arrays. Infrared search and track systems work in the same 3 to 5 μm band as do missile seekers. Future

systems may include the 8 to 12 μm band in addition to 3 to 5 μm in an effort to obtain more skin signature. These threats rely on radar or inertial navigation to place the IR seeker in position to acquire the target. The IR guidance can take over in the terminal phase after the target is confirmed. The threat tracker incorporates automatic gain control to adapt the background level. The target may appear as either negative or positive in contrast to the background. The global signature depends on the sea and sky clutters.

Unresolved signatures result from the difference between the signal received with the target present compared to that received with the target absent. Signature control design requires that the total radiation occluded by the target is supplied by the target. The suppression goal is to minimize target contrast.

Resolved signatures result from pattern-related features including not only the pattern of major recognizable components but also the internal texture of the components. Signature control design requires that such features be disguised. The suppression goal is pattern deception.

The concept of signature control includes everything that minimizes signatures and signal with the aim of delaying or preventing detection and identification. This signature control allows an increase of its own counter-measures and sensors. The benefits gained from reducing infrared signatures are an increased performance of its own sensors and an increase in the performance of its own counter-measures, provided that the radiated and scattered energy from the ship is substantially lower than that of the counter-measures. But the most important benefit of IR signature control is when the infrared signature is so low that even if it is possible to detect the vessel, identification and engagement are impossible. To obtain the later benefit, the infrared signatures must be at the same level as or lower than the environmental background noise (the sea clutter).

We have seen that target signature results from the difference between the target and its immediate background and clutter. The sky background may be reflected by the target. Clutter effects are determined by threat. Reflection from the ocean surface have the effect of altering the apparent shape and spectral content of the target. Reflection occurs in calm seas and in certain solar scenarios.

For nonimaging sensors target total emissions is reduced to match the background emission which is given by the sea emission. Unresolved target signatures depend on background intensity mean values as well as on intensity variations. Contrast should be reduced to some level compared with the sensor's internal noise level.

For resolved targets, imaging sensors see internal target detail and external shape detail. Target signatures are defined by their pattern

features. Resolved target signature depend on background intensity mean values, clutter intensity variations on the size scale of the internal target detail.

Infrared contrast complexity, as we have mentioned before, is due to a number of physical phenomena:

- spectral response of sensor
- spatial resolution of sensor
- range and aspect angle (azimuth and elevation)
- solar heating
- internal heating sources
- wind cooling determined by convective heat transfer
- radiation from exhaust gases
- sea clutter emissivity
- sea state and temperature
- sun glint at the sea surface
- sea surface reflection of cold sky or cloud background

These phenomena are in general difficult to model. Cold sky cooling is countered by water condense and wind effect. Exhaust gas emission peaks in CO₂ extinguishes at ranges 3–5 μm . But the most difficult phenomena to characterize are the sea surface emission and reflection. We present in this paper a self-consistent model of two-dimensional sea emissivity which is a key parameter in sea background model.

The ocean study requires the knowledge of several parameters in order to compute the scattering, the emissivity and the reflectivity of the sea surface. In theory, the ocean is represented by an ergodic and stationary process of second order with three dimensions: one temporal component and two spatial components. This description requires the knowledge of two functions. Firstly, either the two-dimensional sea spectrum or its inverse Fourier transform, the two-dimensional sea autocorrelation function. Secondly, the probability distribution function for either wave heights or slopes. Various sea spectrum found in literature [1, 3, 7, 9–13], e.g., the Pierson, Apel and Elfouhaily spectra established in the 70's, 94 and 97 respectively. These spectra have similar gravity waves but differ in capillary waves. On the opposite, the sea autocorrelation function is often modeled by a gaussian and exponential anisotropic behaviors [16], involving that all characteristics of the sea spectra are not included. With the aim to take them into account, the two-dimensional autocorrelation function of the heights is modeled rigorously as a function of the wind speed, the wind direction and the distance between two points located on the sea surface. The slope probability density assumed to be gaussian requires the calculus of the slope variances in the upwind and crosswind directions. They are determined from the Pierson, Apel and Elfouhaily spectra. The

results are compared with the Cox and Munk model [18]. These different concepts are developed in the first chapter.

Theories for wave scattering from rough surfaces generally assume that the whole surface is illuminated by the incident beam. In practice some regions of the sea surface may be screened by other parts of the surface. This phenomenon is quantified by the shadowing function equal to the ratio of the illuminated surface [23]. Early developments of shadowing theories (Wagner [19], Smith [20, 21]) assume that the shadowing and shadowed point are uncorrelated, involving that the shadowing function is independent of the autocorrelation function. They also suppose that the surface is one-dimensional and that the observed surface is infinite. Recently Ricciardi and Sato [25, 26] showed that the shadowing function is rigorously defined by Rice's infinite series of integrals. This series is computed for uncorrelated gaussian process. Wagner's approach retains only the first term of these series, whereas the Smith formulation uses the Wagner model by introducing a normalization function. In the second chapter we introduce the correlation on the Smith and Wagner shadowing functions, for any autocorrelation function, and for a given observation length. The obtained results are generalized in the monostatic and bistatic two-dimensional cases with and without correlation. The new method improves the previous results without correlation, and may be applied for any autocorrelation function and for any observed surface. For simulations in the two-dimensional case, we use the autocorrelation function modeled in the first chapter.

In the last chapter, the two-dimensional emissivity of the sea surface is computed. This magnitude characterizes the intrinsic radiation of the sea surface in the infrared frequencies. As the temperature measured by the infrared camera depends on the emissivity, it is an important parameter for retrieving the sea surface temperature from remotely sensed radiometric measurements, such as from satellites. In literature, articles [32–34] assume that the surface is isotropic and the shadow is not taken into account. The emissivity model developed by [35, 36] is valid when the average slopes of the sea surface are smaller than unity, involving the use of the Smith one-dimensional shadowing function. We present in the last chapter, our model of the emissivity based on [35, 36]. We do not introduce any hypothesis on the slopes, and we use the two-dimensional shadowing function with and without correlation developed in the second chapter. The polarization is also taken into account.

1. STUDY OF THE SEA BEHAVIOR

1.1 Introduction

1.2 Study of the Waves

- 1.2.1 The Wave Development
- 1.2.2 The Dispersive Relationship
 - 1.2.2.1 *Gravity Waves*
 - 1.2.2.2 *Capillary Waves*
 - 1.2.2.3 *Gravity and Capillary Waves*
- 1.2.3 Fetch
- 1.2.4 Conclusion

1.3 The Sea Statistical Approach

- 1.3.1 Statistics of Stochastic Processes
 - 1.3.1.1 *Second-order Properties*
 - 1.3.1.2 *Stationary Process*
 - 1.3.1.3 *Ergodicity*
 - 1.3.1.4 *Marginal Probability*
- 1.3.2 Configuration of the Problem
- 1.3.3 The Autocorrelation Function
- 1.3.4 The Probability Density
- 1.3.5 Two-Scale Model

1.4 Sea Spectra

- 1.4.1 Introduction
- 1.4.2 The Friction Speed
- 1.4.3 Gravity Spectra
- 1.4.4 Global Spectra: Gravity and Capillary
 - 1.4.4.1 *The Pierson Spectrum*
 - 1.4.4.2 *The Apel Spectrum*
 - 1.4.4.3 *The Elfouhaily, Chapron, Katsaros and Vandemark Spectrum*
 - 1.4.4.4 *Simulations*
- 1.4.5 The Angular Functions

1.5 The Autocorrelation Function

- 1.5.1 The Spatial Autocorrelation Function
 - 1.5.1.1 *Introduction*

1.5.1.2 The Analytical Determination of the Angular Integration

1.5.1.3 Simulation and Modeling

1.5.1.4 Conclusion

1.5.2 Slope Variances

1.5.2.1 The Variance Definition and Angular Integration

1.5.2.2 Numerical Integration over the Wave Number

1.5.2.3 Simulations

1.6 Conclusion

2. THE SHADOWING FUNCTION

2.1 Introduction

2.2 The One-dimensional Monostatic Shadowing Function without Correlation

2.2.1 Introduction

2.2.2 The Definition of the Shadowing Function

2.2.3 The Wagner, Smith and Ricciardi-Sato Approaches

2.2.3.1 Wagner and Smith

2.2.3.2 Ricciardi-Sato

2.2.4 Application for an Uncorrelated Process of the Infinite Surface

2.2.4.1 Wagner and Smith

2.2.4.2 Ricciardi-Sato

2.2.4.3 Simulation on a Gaussian Process

2.3 The One-dimensional Monostatic Shadowing Function with Correlation

2.3.1 Expressions of the Wagner and Smith Conditional Probabilities

2.3.1.1 Wagner

2.3.1.2 Smith

2.3.1.3 Conclusion

2.3.2 Expressions of the Wagner and Smith Shadowing Functions

2.3.2.1 The Wagner and Smith Averaged Shadowing Functions

2.3.2.2 Reduction of the Integration Domain

2.5.3 Conclusion

2.6 Conclusion

3. EMISSIVITY OF THE SEA SURFACE

3.1 Introduction

3.2 Preliminaries

3.2.1 Diffraction by a Facet

3.2.2 Definitions

3.2.2.1 *The Blackbody*

3.2.2.2 *The Wien Law*

3.2.2.3 *The Real Bodies-emissivity*

3.2.2.4 *Coefficients of Reflection, Absorption and Transmission*

3.2.2.5 *The Fresnel Reflection coefficients*

3.2.2.6 *The Sea Refractive Index*

3.2.3 Conclusion

3.3 The Two-dimensional Emissivity

3.3.1 The One-dimensional Emissivity

3.3.1.1 *Geometry of the Problem*

3.3.1.2 *The Average Emissivity*

3.3.1.3 *The Normalized Average Emissivity*

3.3.1.4 *Conclusion*

3.3.2 The Two-dimensional Emissivity

3.3.2.1 *The Problem Geometry*

3.3.2.2 *Determination of the Emissivity*

3.4 Simulations

3.4.1 Emissivity Determined with the Smith Uncorrelated Shadowing Function

3.4.1.1 *Calculus*

3.4.1.2 *Particular Cases*

3.4.1.3 *Simulations of the Emissivity*

3.4.1.4 *Simulations of the Infrared Temperature*

3.4.2 Emissivity Determined with the Smith Correlated Shadowing Function

3.4.2.1 *Calculus*

3.4.2.2 Notice

3.4.2.3 Simulations

3.5 Conclusion

Epilogue

Appendix 1. The Wagner and Smith Shadowing Functions of the Uncorrelated Process for an Infinite Surface

Appendix 2. The Ricciardi-Sato Shadowing Function of the Uncorrelated Process for an Infinite Surface

Appendix 3. The Wagner Conditional Probability of the Correlated Gaussian Process

Appendix 4. The Smith Conditional Probability of the Correlated Gaussian Process

Appendix 5. The Smith Uncorrelated Bistatic Shadowing Function for an Infinite Surface

Appendix 6. The Smith Two-dimensional Conditional Probability of the Correlated Gaussian Process

References

1. STUDY OF THE SEA BEHAVIOR

1.1 INTRODUCTION

The first part of this chapter deals with the fundamental concepts used for the study of the sea surface characterized by two regions: capillary and gravity waves. The fetch is also introduced. It is very difficult to model a sea deterministic representation due to non linear energy transfer between waves. Since the ocean presents an uncoordinate aspect, a statistical approach is used. This approach requires the knowledge of two-dimensional sea spectra giving the energy distribution as a function of the wave number and the wind direction. This aspect is introduced in the third paragraph. The last paragraph is the originality of this chapter. It presents the spatial autocorrelation function of the heights of the sea, which is a relevant information necessary to determine the electromagnetic scattering from a sea surface [8, 16] (Kirchhoff's model and shadowing function). The autocorrelation function is modeled from the Elfouhaily, Chapron, Katzaros and

Vandemark spectrum [9] established in 97's, which is a synthesis of the works have done since 70's about ocean behavior. In literature [16], the autocorrelation function is classically set to anisotropic gaussian or anisotropic exponential. We show that our results improve previous ones. The slope variances are also determined, in order to characterize the slope probability density.

1.2. STUDY OF THE WAVES

The first paragraph introduces the wave behavior, and the second part gives the dispersive equation of gravity and capillary waves. The definition of fetch is also introduced.

1.2.1 The Wave Development

As the wind blows, waves with short wavelength arise (capillary waves) supported by the surface tension. Their amplitude and the wavelength increase due to non linear energy transfer. Such waves are named gravity waves and are supported by the gravitational force. As the wind keeps on blowing waves become stationary. On the opposite, if the wind stops waves of short wavelength vanish quickly, whereas waves with long wavelength damp slowly, and can propagate on a long distance.

In general, we consider two types of sea surface: the wind sea, and the swell. The wind sea is the set of locally created waves, and the swell corresponds to a wind sea old, with regular amplitude and constant period waves longer than wind sea ones.

1.2.2 The Dispersive Relationship

Contrary to electromagnetic wave propagation in vacuum, gravity and capillary sea waves are dispersive, i.e., their propagation speed depends on the wavelength.

1.2.2.1 Gravity Waves

Gravity waves are ruled by a balance between the gravity and the waves inertia. Using a linear approximation, the angular frequency is given by the following equation [1, 2]:

$$\omega^2 = gk \tanh(kd) \quad (1.1)$$

where $g = 9,81\text{ms}^{-2}$ represents the gravitational acceleration, k the wave number in rad/m with $k = 2\pi/\lambda$, λ the wavelength in meter, and d the water depth in meter. In deep water ($kd > 3$), equation (1.1) becomes:

$$\omega = \sqrt{gk} \quad (1.2)$$

The wave velocity is defined by:

$$v_{ph} = \frac{\omega}{k} \Rightarrow v_{ph} = \sqrt{\frac{g}{k}} = \sqrt{\lambda} \sqrt{\frac{g}{2\pi}} \quad (1.3)$$

This shows that short wavelength waves propagate slower than waves with longer wavelength. The speed of gravity waves is proportional to the square root of the wavelength.

1.2.2.2 Capillary Waves

The behavior of capillary waves is characterized by the following dispersive equation [1, 3]:

$$\omega^2 = \frac{\tau}{\rho} k^3 \tanh(kd) \quad (1.4)$$

This behavior is very different from the gravity wave one, where $\tau = 74.10^{-3}\text{N} \cdot \text{m}^{-1}$ is the surface tension, and $\rho = 10^3\text{kg} \cdot \text{m}^{-3}$ its mass density. In deep water, (1.4) becomes:

$$\omega^2 = \frac{\rho}{\tau} k^3 \quad (1.5)$$

The speed in deep water is formulated as:

$$v_{ph} = \sqrt{\frac{\tau k}{\rho}} = \sqrt{\frac{2\pi\tau}{\tau}} \frac{1}{\sqrt{\lambda}} \quad (1.6)$$

Unlike gravity waves, the celerity of capillary waves is proportional to the inverse of the square root of the wavelength.

1.2.2.3 Gravity and Capillary Waves

In the transition zone, the speed in deep water is given by:

$$v_{ph}^2 = g/k + \tau k/\rho \quad (1.7)$$

The lowest speed v_{phm} is obtained from equation (1.7):

$$k_m = \sqrt{\frac{g\rho}{\tau}} \Rightarrow v_{phm} = \sqrt[4]{\frac{4g\tau}{\rho}} \quad \text{and} \quad \omega_m = \sqrt{2gk_m} \quad (1.8)$$

$k_m = 3,64 \text{ rad/cm}$; $v_{phm} = 23 \text{ cm/s}$; $\omega_m = 84,5 \text{ rad/s}$; $\lambda_m = 1,73 \text{ cm}$. Finally the pulsation ω , the velocity speed v_{ph} , and the group speed v_g are, in deep water:

$$\begin{aligned} \omega^2 &= gk \left(1 + \frac{k^2}{k_m^2} \right) & v_{ph} &= \sqrt{\frac{g}{k} \left(1 + \frac{k^2}{k_m^2} \right)} \\ v_g &= \frac{d\omega}{dk} = \frac{1}{2} \left(g + 3g \frac{k^2}{k_m^2} \right) / \sqrt{gk \left(1 + \frac{k^2}{k_m^2} \right)} \end{aligned} \quad (1.9)$$

In figure 1.1 the angular frequency is represented as a function of the wave number. Figure 1.2 shows the velocity speed as a function of the wavelength. We notice that capillary waves are predominant for short wavelengths, whereas gravity waves are predominant for long wavelengths.

1.2.3 Fetch

At a given location (figure 1.3), the sea state does not only depend on the wind local strength, but also on the distance, called fetch [4], on which the wind has blown. If we consider a wind blowing with a constant speed, V , from the coast, and a point far from the coast (point B), waves reach a maximum amplitude which does not depend on the wind speed V . Wave amplitudes increase with the fetch F_0 linked to V . On the contrary, if the point (point A) is close to the coast, the fetch will be smaller and wave amplitudes will depend on the distance from the coast. For a given wave speed, there exists a moving limit which separates two regions. The first one corresponds to the transitory state, i.e., where the wave height depends on the distance from the coast. The second one corresponds to the steady state, where the height is a function of the wind speed only.

1.2.4 Conclusion

At each point of the surface, waves result from a sum of waves locally generated by the wind, and waves coming from any areas. Due

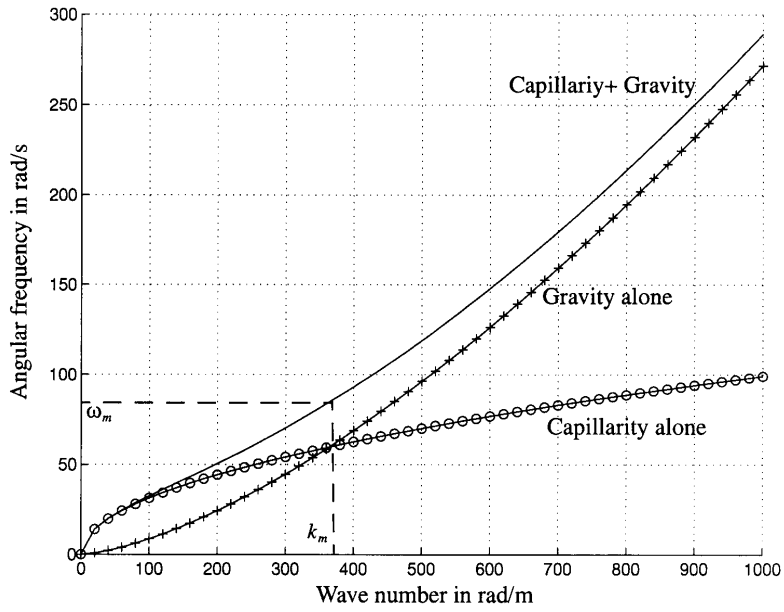


Figure 1.1 Angular frequency as a function of the wave number.

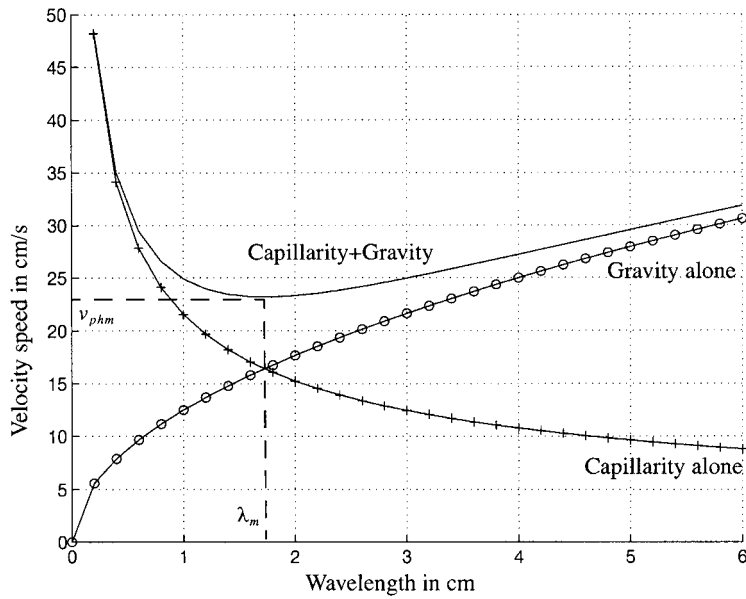


Figure 1.2 Velocity speed as a function of the wavelength.

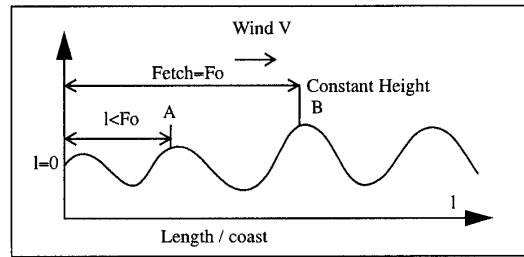


Figure 1.3 Fetch.

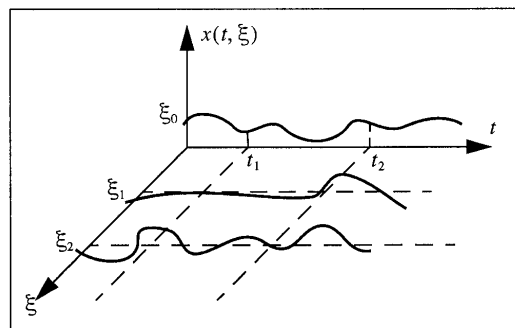


Figure 1.4 Random process.

to these interactions, the phenomenon can hardly be quantified. Since the ocean presents an uncoordinate aspect, the fluctuations of the sea are classically represented by a three dimensional random process.

1.3 THE SEA STATISTICAL APPROACH

1.3.1 Statistics of Stochastic Processes

A stochastic process (figure 1.4) can be represented by a family of real or complex functions $\{x(t, \xi)\}$ [5]. In this interpretation, t and ξ , are variables. If $\xi = \xi_i$ is fixed, then $x(t, \xi) = x(t, \xi_i)$ is a single time function. If $t = t_i$ is fixed, then $x(t, \xi) = x(t_i, \xi)$ is a random variable (RV) equal to the state of the given process at time t_i . Its statistical behavior is characterized by the distribution function $F(x, t_i)$ or by its probability density $p(x, t_i)$. Their knowledge gives the main orders of RV.

1.3.1.1 Second-order Properties

The statistic mean value of the RV $x_i = x(t_i, \xi)$ is equal to:

$$m(t_i) = E[x(t_i, \xi)] = \int x_i p(x, t_i) dx_i \quad (1.10)$$

where the symbol E denotes the expected value. Let $\{x_1 = x(t_1, \xi), x_2 = x(t_2, \xi)\}$ be two random variables assumed to be real, the auto-correlation function R is defined by:

$$R(t_1, t_2) = E[x(t_1, \xi)x(t_2, \xi)] = \iint x_1 x_2 p(x_1, x_2, t_1, t_2) dx_1 dx_2 \quad (1.10a)$$

where $p(x_1, x_2, t_1, t_2)$ denotes the second order probability density of the process $x(t, \xi)$ at the times $\{t_1, t_2\}$ for a ξ fixed.

1.3.1.2 Stationary Process

A stochastic process $x(t, \xi)$ is called strict-sense stationary, if its statistical properties are invariant to a shift of the origin. This means that the processes $x(t, \xi)$ and $x(t + \tau, \xi)$ have the same statistics for any τ . A stochastic process is stationary of second order if its one and second orders statistical are invariant in the time and equations (1.10) and (1.10a) become:

$$R(t_1, t_2) = R(\tau) \quad \text{and} \quad m(t_i) = m \quad \text{with} \quad \tau = t_2 - t_1 \quad (1.10b)$$

1.3.1.3 Ergodicity

A stochastic process $x(t, \xi)$ is called ergodic if the time averages are equal to the statistical means:

$$\overline{x^n} = \lim_{T \rightarrow \infty} \frac{1}{2T} \int_{-T}^T x^n(t, \xi_i) dt = \int x^n(t_i, \xi) p(x) dx \quad (1.10c)$$

1.3.1.4 Marginal Probability

Let $p(x, y)$ be a two variable probability density, the marginal probability $p(x)$ is defined by:

$$p(x) = \int p(x, y) dy \quad (1.10d)$$

1.3.2 Configuration of the Problem

The fluctuations of the sea are represented by a three dimensional random process $z(\vec{r}, t)$: one temporal and two spatial components. The vector $\vec{r}(x, y)$ stands for the spatial location of the point represented by its cartesian coordinates (x, y, z) at the time t . Furthermore, the process is supposed to be stationary and ergodic.

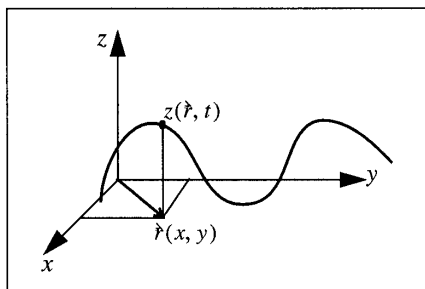


Figure 1.5 Mathematical representation of the sea.

For an ergodic and stationary process, the surface behavior is completely determined by the knowledge of its spectrum or its autocorrelation function, and its slope density probability [5]. Literature provides various sea spectra. The autocorrelation function is calculated from the spectrum by the way of an inverse Fourier transform.

1.3.3 The Autocorrelation Function

In a Cartesian coordinate system (x, y, z) , the surface shift $z(\vec{r}, t)$ at a point specified by $\vec{r}(x, y)$ and at time t may be generally expressed as a two-dimensional integral of a plane-wave mode of the surface wave [6], each mode being specified by a two-dimensional wave number vector \vec{k} :

$$z(\vec{r}, t) = \frac{1}{2} \int_{-\infty}^{\infty} \int_{-\infty}^{\infty} \left\{ a(\vec{k}) e^{j[\vec{k} \cdot \vec{r} - \omega(k)t]} + a^*(\vec{k}) e^{-j[\vec{k} \cdot \vec{r} - \omega(k)t]} \right\} d\vec{k} \quad (1.11)$$

with $a(\vec{k})$ the complex amplitude of the plane wave mode of a given wave number vector, and $a^*(\vec{k})$ the complex conjugate of $a(\vec{k})$. $\omega(k)$ is the angular frequency function of k . Since the function $z(\vec{r}, t)$ is real

we have $a^*(-\vec{k}) = a(\vec{k})$, moreover the average surface displacement $\langle z(\vec{r}, t) \rangle$ is chosen equal to zero. The spectrum $\Psi(\vec{k})$ is defined as follows:

$$\psi(\vec{k}) = \langle |a(\vec{k})|^2 \rangle = \psi(-\vec{k}) \quad (1.12)$$

where $\langle \rangle$ stands for the mean operator. Since the sea surface is supposed to be homogeneous in space i.e., the fetch is infinite, and to be stationary in time, the corresponding autocorrelation function Z is [6]:

$$Z(\vec{R}; \tau) = \langle z(\vec{r}, t) z(\vec{r}', t') \rangle = \int_{-\infty}^{\infty} \int_{-\infty}^{\infty} \psi(\vec{k}) \cos[\vec{k}(\omega)\vec{R} - \omega\tau] d\vec{k} \quad (1.13)$$

with $\vec{R} = \vec{r}' - \vec{r}$ and $\tau = t' - t$. Moreover (figure 1.6):

$$\vec{R} = \|\vec{R}\| \cdot \vec{\sigma} = R \cdot (\vec{x} \cos \phi + \vec{y} \sin \phi) \quad \vec{k} = \|\vec{k}\| \cdot \vec{s} = k \cdot (\vec{x} \cos \Theta + \vec{y} \sin \Theta) \quad (1.14)$$

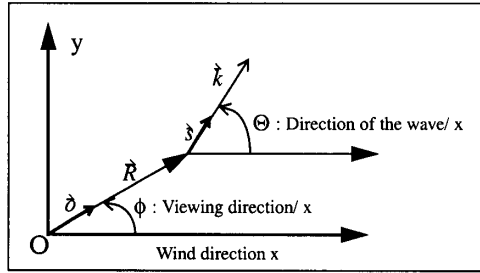


Figure 1.6 Polar coordinates.

where $\vec{\sigma}$ is the unitary vector of \vec{R} in the viewing direction ϕ with respect to x , and \vec{s} the unitary vector between the directions Θ and x . The axis (Ox) shows the wind direction. In polar coordinates the autocorrelation function becomes:

$$Z(R, \phi; \tau) = \int_0^{\infty} \int_{-\pi}^{\pi} S(k, \Theta) \cos[kR \cos(\Theta - \phi) - \omega\tau] d\Theta dk \quad (1.15)$$

The quantity $S(k, \Theta) = k\psi(k, \Theta)$ represents the sea spectrum. Spectra are often defined as a function of the angular frequency $S(\omega, \Theta)$.

The relation between $S(k, \Theta)$ and $S(\omega, \Theta)$ is given by:

$$S(\omega, \Theta) = S(k, \Theta) \frac{dk}{d\omega} = \frac{S(k, \Theta)}{v_g(k)} \quad (1.16)$$

The dispersive equation (1.9) is expressed as a function of the wave number k . We notice that the spatial autocorrelation function ($\tau = 0$) in cartesian coordinates is obtained from the real part of the inverse Fourier transform of the spectrum:

$$\begin{aligned} Z(R_x, R_y) &= \int_{-\infty}^{\infty} \int_{-\infty}^{\infty} \frac{S(k_x, k_y)}{\sqrt{k_x^2 + k_y^2}} \cos(k_x R_x + k_y R_y) dk_x dk_y \\ &= \Re \left\{ TF^{-1} \left[\frac{S(k_x, k_y)}{\sqrt{k_x^2 + k_y^2}} \right] \right\} \end{aligned} \quad (1.17)$$

$$\text{with } \Theta = \text{atan}(k_y/k_x) \quad \text{and} \quad k = \sqrt{k_x^2 + k_y^2} \quad (1.17a)$$

1.3.4 The Probability Density

The slope probability density of waves is assumed to be a zero mean gaussian:

$$p(\gamma_x, \gamma_y) = \frac{1}{2\pi\sigma_x\sigma_y\sqrt{1-\rho^2}} \exp\left(\frac{-1}{2(1-\rho^2)} \left[\frac{\gamma_x^2}{\sigma_x^2} + \frac{\gamma_y^2}{\sigma_y^2} - \frac{2\rho\gamma_x\gamma_y}{\sigma_x\sigma_y} \right]\right) \quad (1.18)$$

where $\{\sigma_x^2, \sigma_y^2\}$ are the slope variances in the upwind and crosswind directions, and ρ the crosscorrelation coefficient. The linearity of the gaussian process involves that the height probability density is gaussian [7], as depicted:

$$p(\xi) = \frac{1}{\sqrt{2\pi\omega}} \exp\left(-\frac{\xi^2}{2\omega^2}\right) \quad (1.19)$$

where ω^2 is the height variance. The knowledge of the gaussian signal spectrum implies the knowledge of its statistical distribution (paragraph 1.5.2).

1.3.5 Two Scale Model

In paragraph 1.2.2, we have seen that the sea surface is characterized by the capillary and gravity waves. In order to include these two behaviors, a two scale model [8] is used to represent the ocean surface. It is obtained by superposing two surfaces (figure 1.7):

$$z(x, t) = z_c(\vec{r}, t) + z_g(\vec{r}, t) \quad (1.20)$$

$z_c(\vec{r}, t)$ is the small scale structure ruled by capillary waves, and $z_g(x, t)$ is the high scale structure ruled by gravity waves. Supposing that the process is stationary in time and space, the autocorrelation function is ($\tau = t' - t$, $\vec{R} = \vec{r}' - \vec{r}$):

$$Z(\vec{R}, \tau) = \langle z(\vec{r}, t)z(\vec{r}', t') \rangle = Z_c(\vec{R}, \tau) + Z_g(\vec{R}, \tau) + 2Z_{cg}(\vec{R}, \tau) \quad (1.21)$$

$$\text{with} \quad \begin{cases} Z_c(\vec{R}, \tau) = \langle z_c(\vec{r}, t)z_c(\vec{r}', t') \rangle \\ Z_g(\vec{R}, \tau) = \langle z_g(\vec{r}, t)z_g(\vec{r}', t') \rangle \\ Z_{cg}(\vec{R}, \tau) = \langle z_c(\vec{r}, t)z_g(\vec{r}', t') \rangle \end{cases} \quad (1.21a)$$

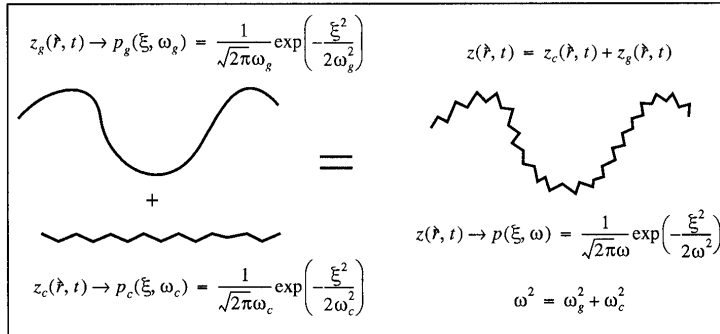


Figure 1.7 Two scales model.

Furthermore, the structures are independent, thus:

$$Z_{cg}(\vec{R}, \tau) = 0 \quad \Rightarrow \quad Z(\vec{R}, \tau) = Z_c(\vec{R}, \tau) + Z_g(\vec{R}, \tau) \quad (1.22)$$

In the spectral domain, the autocorrelation function $Z_g(\vec{R}, \tau)$ of the high scale structure is obtained by integrating the spectrum between $[0; k_{cg}]$, whereas the small scale structure $Z_c(\vec{R}, \tau)$ is integrated between $[k_{cg}; \infty]$. The calculus of the wave number k_{cg} between gravity

and capillary waves is the major issue of this model. Nevertheless this quantity is not necessary to determine the probability density of $z(\vec{r}, t)$.

Let $\{p_g(\xi, \omega_g), p_c(\xi, \omega_c)\}$ be the gaussian probability densities of independent random variables, respectively, $\{z_g, (\vec{r}, t), z_c(\vec{r}, t)\}$. The resulting probability density $p(\xi, \omega)$ ruling $z(\vec{r}, t)$ is equal to the convolution product $p_g(\xi, \omega_g) * p_c(\xi, \omega_c)$. Since, the convolution product of two gaussian processes is a gaussian process, $p(\xi, \omega)$ is gaussian with its variance equal to $\omega^2 = \omega_g^2 + \omega_c^2$ (equation (1.22)). Once the probability density is being known, the description of the sea necessitates either its spectrum or its autocorrelation function. The following paragraph introduces spectra presented in literature.

1.4 SEA SPECTRA

1.4.1 Introduction

During the 60's, sea spectra have been studied at various frequencies bands (L to Ku), i.e., between two and eighteen GHz. Classically, a sea spectrum is set to:

$$S(k, \Theta) = M(k)f(k, \Theta) \quad (1.23)$$

where $M(k)$ represents the isotropic part of the spectrum modulated by $f(k, \Theta)$ corresponding to the angular function.

Since this spectrum is even, the angular function is given by [9]:

$$f(k, \Theta) = \frac{1}{2\pi} [1 + \Delta(k) \times \cos(2\Theta)] \quad (1.24)$$

The first angular functions established in the 70's did not check this condition.

1.4.2 The Friction Speed

The wind friction speed u_f is defined by the boundary wind speed over the sea surface and does not depend on the height. Table 1.1 gives the relations between this speed and the Beaufort scale and the wind speed at ten meters above the sea. The wind speed u_z in cm/s, at an altitude z in cm, is given as a function of the friction speed u_f , in cm/s by [3]:

$$u_z \frac{u_f}{0,4} \ln \left(\frac{z}{z_0} \right) \quad \text{with} \quad z_0 = \frac{0,684}{u_f} + 4,28 \times 10^{-5} u_f^2 - 4,43 \times 10^{-2} \quad (1.25)$$

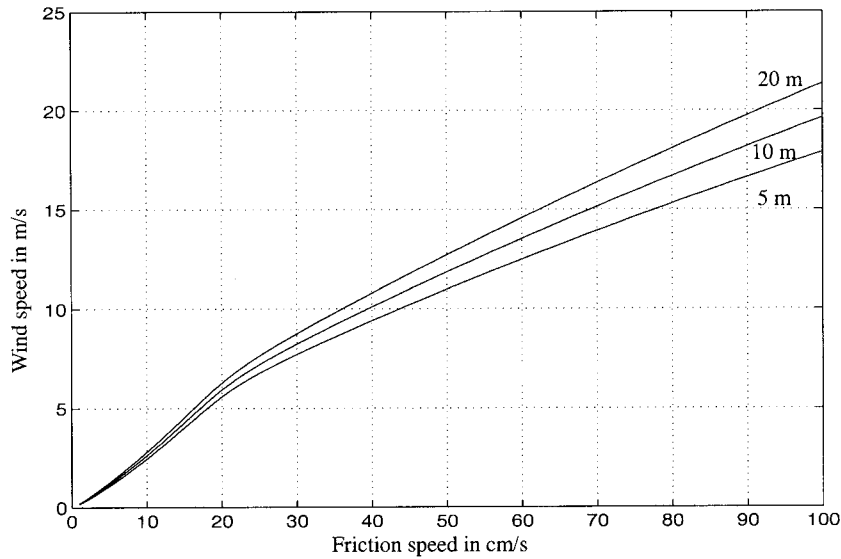


Figure 1.8. Wind speed as a function of the friction speed.

Table 1.1 Beaufort scale.

Beaufort scale	Descriptive terms	Friction speed in cm/s	Wind speed 10 m above the sea in m/s
0	Calm	< 1	< 0,2
1	Very slight breeze	2–6	0,4–1,4
2	Slight breeze	7–12	1,7–3,3
3	Little breeze	13–18	3,6–5,3
4	Breeze	19–28	5,6–7,8
5	Well breeze	28–43	7,8–10,6
6	Fresh	44–62	10,8–13,8
7	High fresh	63–83	14,0–17,1
8	Breakwind	84–108	17,3–20,7
9	High breakwind	109–136	20,9–24,4
10	Sorm	137–168	24,6–28,4
11	Storm fierce	169–206	28,5–32,6
12	Hurricane	> 207	32,7

In figure 1.8, the speed u_z above the sea is plotted as a function of the friction speed u_f , for $z = \{5, 10, 20\}$ meters.

1.4.3 Gravity Spectra

The first one-dimensional spectra $M(k)$ established in the 70's by Pierson- Moskowitz $M_{PM}(k)$ [1, 10–12] JONSWAP (Joint North Sea Wave Project) $M_J(k)$ [13], give the energy of gravity waves:

$$M_{PM}(k) = \frac{4,05 \times 10^{-3}}{k^3} \exp\left(-\frac{0,74g^2}{k^2u_{19}^4}\right) \quad (1.26)$$

$$M_J(k) = M_{PM}(k) \times 3,3 \exp\left[-\frac{(\sqrt{\frac{k}{k_0}}-1)^2}{2\delta^2}\right] \text{ avec } \delta = \begin{cases} 0,07 & \text{si } k < k_0 \\ 0,09 & \text{si } k > k_0 \end{cases} \\ k_0 = 0,769g/u_{19}^2 \quad (1.27)$$

where $g = 9,81 \text{ m} \cdot \text{s}^{-2}$ is the gravitational acceleration, u_{19} is the wind speed in m/s at an altitude of 19.5 m above the sea, and k the wave number. In the left part of figure 1.9 shows the Pierson-Moskowitz normalized spectrum as a function of the wave number k , for $u_f = \{84, 49, 12\}$ cm/s. We notice that all curves have a maximum k_{peak}^P corresponding to the velocity speed v_{ph}^{peak} :

$$k_{peak}^P = 0,702 \frac{g}{u_{19}^2} \quad \text{and} \quad v_{ph}^{peak} = 1,194u_{19} \quad (1.28)$$

When the velocity speed is inferior to the wind speed, the waves are strongly shaped by the wind, and their energy increases until the wave speed reaches a value close to v_{ph}^{peak} . Their energy is then maintained by the wind. We notice that as the friction speed increases, the wave number maximum decreases due to gravity waves.

In figure 1.9 (right), the Pierson-Moskowitz and JONSWAP spectra are compared for a friction speed $u_f = 49$ cm/s. We observe that the Pierson-Moskowitz and JONSWAP spectra are similar, excepted around the value $k_0 \approx k_{peak}^P = 4,4 \times 10^{-4}$ rad/cm corresponding to a friction speed equal to 49 cm/s.

In fact in this area, the exponent in equation (1.27) is maximum implying a peak overshoot (about 70%), which decreases quickly when one goes far from this value to tend to the Pierson-Moskowitz spectrum. All these spectra are right for a fully developed sea, i.e., for an infinite fetch. JONSWAP propose a new model developed from the

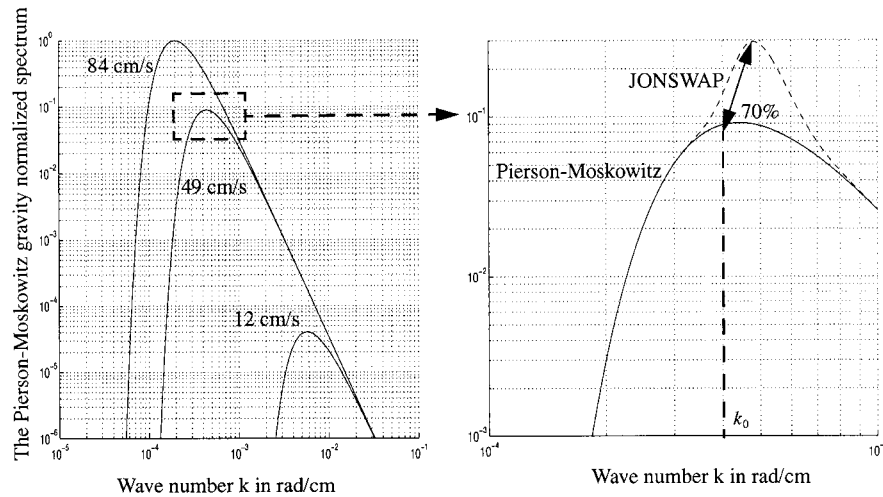


Figure 1.9 The Pierson-Moskowitz and JONSWAP spectra as a function of the wave number.

first one (1.27), which takes into account the fetch X in meter [13]:

$$S_{JM}(k) = \frac{\alpha}{2k^3} \exp\left(-\frac{5}{4} \frac{k_m^2}{k^2}\right) 3, 3 \exp\left[-\frac{\left(\sqrt{\frac{k}{k_m}} - 1\right)^2}{2\delta^2}\right] \quad (1.29)$$

$$avec \quad \begin{cases} \delta = \begin{cases} 0,07 & si \ k \leq k_m \\ 0,09 & si \ k > k_m \end{cases} \\ k_m = 483,6 \frac{g}{u_{10}^2} \bar{X}^{-0,66} \end{cases} \quad et \quad \begin{cases} \alpha = 0,076 \bar{X}^{-0,22} \\ \bar{X} = \frac{gX}{u_{10}^2} \end{cases} \quad (1.29a)$$

In figure 1.10, this spectrum is plotted as a function of the wave number k for different values of fetch $X = \{500, 100, 50\}$ km with $u_f = 30$ cm/s . As the fetch decreases, the peak moves to higher wave number, i.e., to shorter wavelengths.

1.4.4 Global Spectra: Gravity and Capillary

The Pierson spectrum [3, 10, 12] is one of the first spectra published in the literature to describe capillary waves. Today, its behavior remains invariant in gravity zone, but has been modified in capillary zone. The John R. Apel spectrum [7, 9] and scientists Donelan, Banner and Jahne is a synthesis of works done in 80's and 90's about ocean

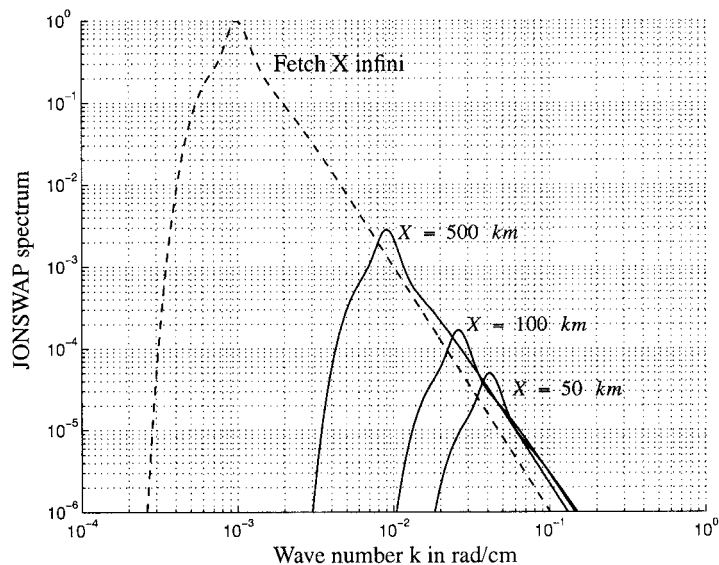


Figure 1.10 The JONSWAP spectrum as a function of the wave number k with $u_f = 30$ cm/s.

spectra modeling. Unfortunately this spectrum does not fit some physical criteria in capillary zone (paragraph 1.5.2).

So T. Elfouhaily, B. Chapron, K. Katsaros, D. Vandemark [9] have established a spectrum which agrees with the experiments and some physical conditions about the slopes given by capillary spectrum (paragraph 1.5.2).

1.4.4.1 The Pierson Spectrum

Pierson [3, 10, 12] depicts the wave spectrum as a function of the wave number k . It is obtained from the Pierson-Moskowitz expression:

$$M_P(k) = M_i(k) \quad k_{i-1} < k < k_i \text{ rad/cm} \quad (1.30)$$

with

$$M_1(k) = \frac{4,05 \times 10^{-3}}{k^3} \exp\left(-\frac{0,74g^2}{k^2 u_{19}^4}\right) \quad 0 < k < k_1 = \frac{k_2 u_m^2}{u_f^2} \quad (1.30a)$$

$$M_2(k) = \frac{4,05 \times 10^{-3}}{k_1^{1/2} k^{5/2}} \quad k_1 < k < k_2 = 0,359 \quad (1.30b)$$

$$M_3(k) = M_4(k_3) \left(\frac{k}{k_3} \right)^q \quad k_2 < k < k_3 = 0,942 \quad (1.30c)$$

$$M_4(k) = 0,875(2\pi)^{p-1} g^{\frac{1-p}{2}} \left(1 + \frac{3k^2}{k_m^2} \right) / \left[k \left(1 + \frac{k^2}{k_m^2} \right) \right]^{\frac{p+1}{2}} \quad k_3 < k < k_4 \quad (1.30d)$$

$$M_5(k) = 1,473 \times 10^{-4} u_f^3 \frac{k_m^6}{k^9} \quad k_4 < k \quad (1.30e)$$

$$k_m = 3,63 \quad p = 5 - \log u_f \quad u_m = 12 \text{ cm/s} \quad q = \frac{\log[M_2(k_2)/M_4(k_3)]}{\log(k_2/k_3)} \quad (1.30f)$$

k_4 can be found numerically by setting $M_4(k)$ equal to $M_5(k)$, and u_f is the friction velocity. The term $M_1(k)$ represents the gravity region (Pierson-Moskowitz) and $M_4(k)$ the capillary waves. u_{19} is the wind speed at an altitude of 19.5 meters above the sea.

1.4.4.2 The Apel Spectrum

The Apel spectrum $M_A(k)$ is given by:

$$M_A(k) = k^{-3} \cdot L_o(k) \cdot J_p(k) \cdot I_D(k) \cdot C_i(k, u_{10}) \quad (1.31)$$

with

$$L_o(k) = e^{-\frac{k^2}{k_p^2}} \quad k_p = g/(u_{10}^2 \sqrt{2}) \quad (1.31a)$$

$$J_p(k) = 1,7 \exp \left[\frac{\left(\sqrt{\frac{k}{k_p}} - 1 \right)^2}{2\delta^2} \right] \quad \delta = 0,40 \quad (1.31b)$$

$$I_D(k) = \Theta_S \sqrt{2\pi} \operatorname{erf} \left(\frac{\pi}{\Theta_S \sqrt{2}} \right) \quad \Theta_S = 1/\sqrt{0,28 + 10 \left(\frac{k}{k_p} \right)^{-1,3}} \quad (1.31c)$$

$$C_i = A(R_{ro} + S \cdot R_{res}) V_{dis} \quad (1.31d)$$

$$\begin{cases} R_{ro} = 1/[1 + (k/k_{ro})^2] & R_{res} = ak \operatorname{sech} \left(\frac{k - k_{res}}{k_w} \right) \\ S(u_{10}) = e^{\ln 10 [s_1 + s_2 (1 - e^{-u_{10}/u_n})]} & V_{dis} = e^{-k^2/k_{dis}^2} \end{cases} \quad (1.31e)$$

$$\begin{cases} k_{ro} = 100 & k_{res} = 400 & k_w = 450 & k_{dis} = 6283 \\ s_1 = -4,95 & s_2 = 3,45 & u_n = 4,7 & A = 0,00195 & a = 0,8 \\ \operatorname{sech}(x) = 2/(e^x + e^{-x}) \end{cases} \quad (1.31f)$$

k is in rad/m. The term $L_o(k)$ represents the gravity region and C_i the capillary waves. The function $J_p(k)$ describes the overshoot of wave energy near the sea spectral peak similarly to the JONSWAP modeling (equation (1.27)).

1.4.4.3 The Elfouhaily, Chapron, Katsaros and Vandemark Spectrum

The spectrum [9] established in 97's is a synthesis of the works done since the 70's on ocean behavior description. It is obtained from experimental and theoretical facts that Apel and Pierson did not take into account, like for example the Cox and Munk model [12] (paragraph 1.5.2). Moreover the fetch is included. This spectrum is formulated as:

$$M_E(k) = \frac{k^{-3}}{2v_{ph}} (\alpha_g v_g F_g + \alpha_c v_{phm} F_c) \kappa \exp \left[-\frac{(\sqrt{\frac{k}{k_p}} - 1)^2}{2\delta^2} \right] \exp \left(-\frac{5k_p^2}{4k^2} \right) \quad (1.32)$$

with:

$$\alpha_g = 6 \times 10^{-3} \sqrt{\Omega} \quad v_g = u_{10}/\Omega \quad F_g = \exp \left[-\frac{\Omega}{\sqrt{10}} \left(\sqrt{\frac{k}{k_p}} - 1 \right) \right] \quad (1.32a)$$

$$\kappa = \begin{cases} 1,7 & 0,84 < \Omega \leq 1 \\ 1,7 + 6 \log \Omega & 1 < \Omega \leq 5 \end{cases} \quad (1.32b)$$

$$\begin{cases} \delta = 0,08(1 + 4/\Omega^3) & k_p = \Omega^2 g / u_{10}^2 \\ \Omega = 0,84 \tanh [(X/2, 2 \times 10^4)^{0,4}]^{-0,75} \end{cases}$$

$$\alpha_c = 10^{-2} \begin{cases} 1 + \ln(u_f/v_{phm}) & u_f \leq v_{phm} \\ 1 + 3 \ln(u_f/v_{phm}) & u_f > v_{phm} \end{cases} \quad F_c = \exp \left[-\frac{1}{4} \left(\frac{k}{k_m} - 1 \right)^2 \right] \quad (1.32c)$$

$$k_m = 363 \text{ rad/m} \quad v_{phm} = 0,23 \text{ m/s} \quad v_{ph} = \sqrt{\frac{g}{k} \left(1 + \frac{k^2}{k_m^2} \right)} \quad (1.32d)$$

Equations (1.32d) coming from paragraph 1.2.2. The quantity X denotes the fetch in meter. So for a fully developed sea, i.e., an infinite fetch, the inverse wave age Ω is equal to 0.84, then $\delta = 0,62$; $k_p \approx g/(u_{10}^2 \sqrt{2})$; $\kappa = 1,7$. These values are close to Apel's ones. The first term (index g) of equation (1.32) represents the gravity zone.

1.4.4.4 Simulations

In figure 1.11 the Elfouhaily (equation (1.32)) with $\Omega = 0,84$), Apel (equation (1.31)) and Pierson (equation (1.30)) spectra are plotted as a function of the wave number, for a friction speed $u_f = 30$ cm/s.

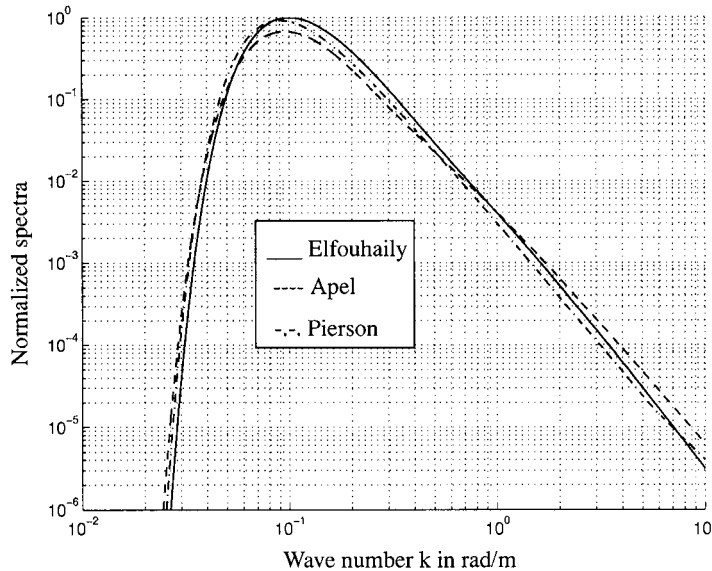


Figure 1.11 Spectra as a function of the wave number for a given friction speed $u_f = 30$ cm/s.

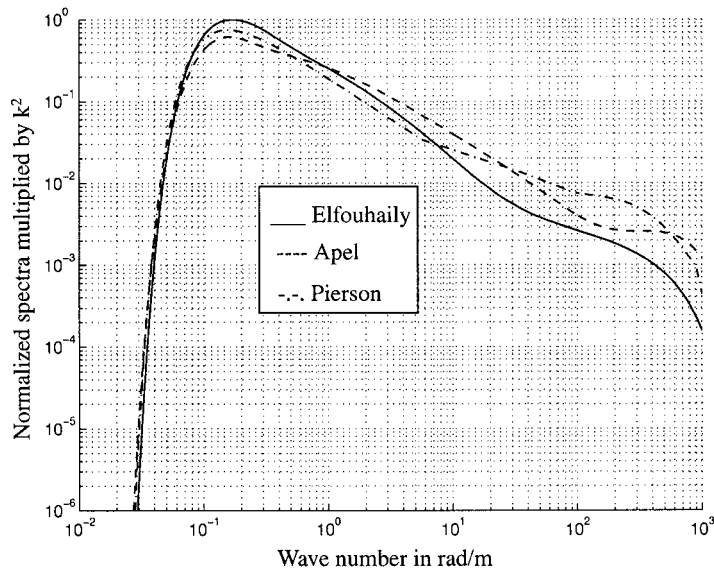
The curves are normalized by the maximum value of the Elfouhaily spectrum. We observe that the spectra have the same behavior. In fact they slightly differ around the peak. The wave number k_{peak} and the corresponding value of the spectrum M_{peak} are given in table 1.2.

We notice that the Apel spectrum maximum is smaller than the Elfouhaily and Pierson ones. The maxima are obtained from gravity waves, since capillary waves are negligible.

Physically the integration of the spectrum over the wave number k between zero and the infinite is equal to the height variance (table 1.2), where gravity waves are more important. This property is verified in paragraph 1.5.1.3. The slope variance is obtained by multiplying the spectrum by the square wave number k^2 . In this case, the capillary zone is not negligible. Figure 1.12 illustrates this notice.

Table 1.2 Spectra maxima values.

	Elfouhaily	Apel	Pierson
Peak wave number k_{peak} in rad/m	$0,976k_p$	$0,931k_p$	$0,876k_p$
Spectrum peak M_{peak} in rad^3/m^3	$0,001343/k_p^3$	$0,000966/k_p^3$	$0,001345/k_p^3$
Height variance $\int_0^\infty M(k)dk$	$0,00193/k_p^2$	$0,00140/k_p^2$	$0,00176/k_p^2$

**Figure 1.12** Spectra multiplied by k^2 as a function of the wave number, for a given friction speed $u_f = 30$ cm/s.

1.4.4.5 The Angular Functions

The spectra described in the last paragraph give a one-dimensional description of the waves propagation. In fact every spectral ray is propagating in the beam direction $\Theta \in [-\pi, \pi]$ according to the wind direction. The spectrum $S(k, \Theta)$ is two-dimensional:

$$S(k, \Theta) = M(k)f(k, \Theta) \quad (1.33)$$

where $f(k, \Theta)$ is the angular function, moreover, the spectrum being

even (equation (1.12)), $f(k, \Theta)$ must be written [9]:

$$f(k, \Theta) = \frac{1}{2\pi}[1 + \Delta(k) \times \cos(2\Theta)] \tag{1.34}$$

The first angular function developed in the 70's did not check the condition (1.34). The Elfouhaily [9], Apel [9] and Pierson [1] terms $\{\Delta_E(k), \Delta_A(k), \Delta_P(k)\}$ are respectively:

$$\begin{cases} \Delta_E(k) = \tanh \left[a_0 + a_g \left(\frac{v_{ph}}{v_g} \right)^{2,5} + a_c \left(\frac{v_{phm}}{v_{ph}} \right)^{2,5} \right] \\ \Delta_A(k) = \tanh \left[0,173 + 6,168 \left(\frac{k}{k_p} \right)^{-1,3} \right] \\ \Delta_P(k) = 1 \end{cases} \begin{cases} a_0 = 0,173 & a_g = 4 \\ a_c = 0,13 \frac{u_f}{v_{phm}} \end{cases} \tag{1.35}$$

We notice that $\Delta_P(k)$ is independent of the wave number k . The velocity speeds $\{v_g, v_{ph}, v_{phm}\}$ are given by equations (1.32a) and (1.32d). In figure 1.13 the functions $\{\Delta_E(k), \Delta_A(k), \Delta_P(k)\}$ of Elfouhaily ($\Omega = 0,84$), Apel and Pierson are plotted as a function of the wave number, and for a friction speed $u_f = 30$ cm/s, corresponding to a gravity peak about $k_{peak} = 0,1$ rad/m (table 1.2).

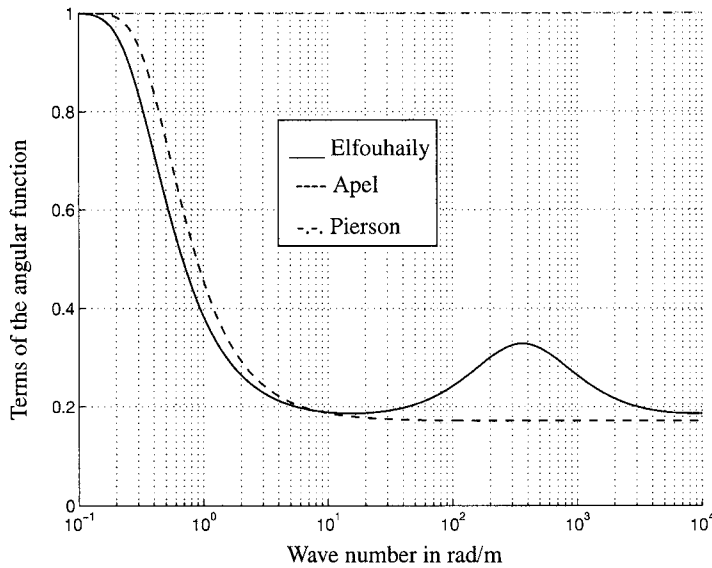


Figure 1.13 Angular function terms $\{\Delta_E(k), \Delta_A(k), \Delta_P(k)\}$ as a function of the wave number, for a friction speed $u_f = 30$ cm/s.

We observe that the Apel function decreases with the wave number, and is superior to the Elfouhaily one in gravity zone ($k \in [k_{pic}; 10k_{pic}]$), whereas in capillary waves, the Elfouhaily term reaches a maximum corresponding to the wave number value where the velocity is equal to the group speed.

1.4.6 Conclusion

The first sea spectra have been established in the 70's in order to determine the electromagnetic scattering from the sea rough surface. We can quote the Pierson and the JONSWAP gravity spectra. Today, these spectra are still identical in the gravity zone, whereas they have significantly evolved in capillary waves:

- The Apel spectrum is a synthesis of works done in the 80's and the 90's.
- The Elfouhaily spectrum which based on Apel's works including physical criteria in capillary zone.

In general, sea spectra depend on the wave number, the wind speed and the fetch. An other characteristic is their angular behavior which gives the energetic spreading of the waves as a function of the wind direction. This function has been also modified in order to be symmetric in the upwind and crosswind directions. This property is illustrated in figure 1.14.

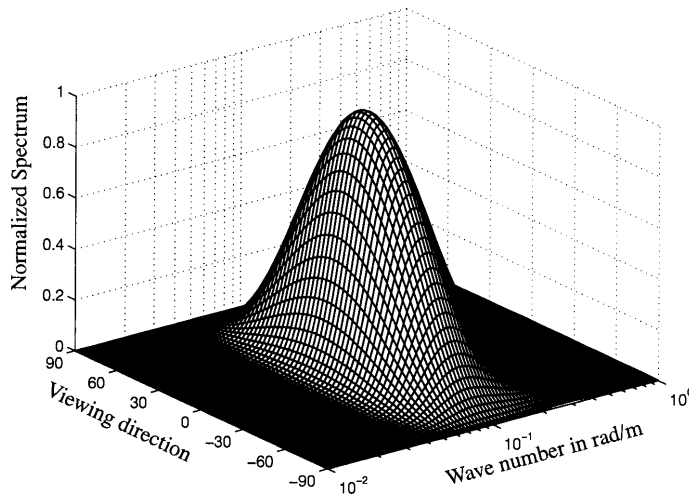


Figure 1.14 The Elfouhaily normalized two-dimensional spectrum for a friction speed $u_f = 30$ cm/s and $\Omega = 0,84$.

The statistical approach allows to characterize the sea either by its spectrum or its autocorrelation function. The subject of this paragraph is to model the autocorrelation function introduced in the correlated shadowing function.

1.5 THE AUTOCORRELATION FUNCTION

The goal of the paragraph is to model the spatial autocorrelation function of the heights, which represents an important parameter in the correlated shadowing function formulation. We use the Elfouhaily spectral configuration [9].

The slope variances calculated with the Pierson, Apel and [9] are also compared with the Cox and Munk model.

1.5.1 The Spatial Autocorrelation Function

1.5.1.1 Introduction

Substituting equation (1.24) into (1.23), the sea spectrum $S(k, \Theta)$ is given by:

$$S(k, \Theta) = \frac{1}{2\pi} M(k) [1 + \Delta(k) \times \cos(2\Theta)] \quad (1.36)$$

where $M(k)$ represents the spectrum isotropic part, and Θ the angle between the wave and wind directions. So, using equation (1.15), the autocorrelation function is:

$$\begin{aligned} Z(R, \phi; \tau) = & \frac{1}{2\pi} \int_0^{\infty} \int_{-\pi}^{\pi} M(k) [1 + \Delta(k) \\ & \times \cos(2\Theta)] \cos[kR \cos(\Theta - \phi) - \omega\tau] d\Theta dk \end{aligned} \quad (1.37)$$

The spatial autocorrelation function of the heights $R_0(R, \phi)$ is obtained for $\tau = 0$:

$$R_0(R, \phi) = \frac{1}{2\pi} \int_0^{\infty} \int_{-\pi}^{\pi} M(k) [1 + \Delta(k) \times \cos(2\Theta)] \cos[kR \cos(\Theta - \phi)] d\Theta dk \quad (1.38)$$

If the double integral is determined numerically in cartesian coordinates $\{k_x = k \cos \Theta, k_y = k \sin \Theta\}$ (equation (1.17)) by a FFT algorithm, $R_0(R, \phi)$ depends on the two parameters $\{R_x = R \cos \phi, R_y =$

$R \sin \phi$. In order to reduce the parameters number, the angular integration is analytic.

1.5.1.2 The Analytical Determination of the Angular Integration

We know that [14] (equation 9.1.44 Abramowitz):

$$\cos(x \cos \alpha) = J_0(x) + 2 \sum_{m=1}^{\infty} (-1)^m J_{2m}(x) \cos(2m\alpha) \quad (1.39)$$

where J_{2m} is the Bessel function of order $2m$ and the first kind, then we show:

$$\int_{-\pi}^{\pi} \cos[x \cos(\Theta - \phi)] \cdot \cos(a\Theta) d\Theta = \begin{cases} 0 & \text{if } a \text{ odd} \\ (-1)^p 2\pi J_a(x) \cos(a\phi) & \text{if } a = 2p \text{ even} \end{cases} \quad (1.40)$$

Using equation (1.40), the angular integration of the spatial autocorrelation function is equal to:

$$R_0(R, \phi) = I_0(R) - \cos(2\phi) I_2(R) \text{ with } \begin{cases} I_0(R) = \int_0^{\infty} M(k) J_0(Rk) dk \\ I_2(R) = \int_0^{\infty} M(k) J_2(Rk) \Delta(k) dk \end{cases} \quad (1.41)$$

Physically the term I_0 represents the isotropic part, whereas I_2 is the anisotropic part.

1.5.1.3 Simulation and modeling

In order to determine the numerical integration of R_0 , it is necessary to find the inferior boundary k_1 and the superior boundary k_2 . In fact only a study of the spectrum $M(k)$ can lead to these boundaries, since the function $\Delta(k)$ is contained between zero and one. We show that the values $\{k_1, k_2\}$ that reach the value of 10^{-5} of maximum are:

$$\begin{cases} k_1 = 0, 28k_p \\ k_2 = 64k_p \end{cases} \quad \text{with} \quad k_p = \frac{\Omega^2 g}{u_{10}^2} \quad (1.42)$$

In figure 1.15 the terms $\{I_0(R), I_2(R)\}$ are plotted as a function of the distance R , for friction speeds $u_f = \{20, 40, 60, 80\}$ cm/s. As the wind speed increases, we observe that the anisotropic term $I_2(R)$ moves towards higher wave numbers, but its maximum remains constant. We also observe that the autocorrelation function variations are identical. In figure 1.15 are plotted in crosses and in circles the functions $\{I_0(R), I_2(R)\}$ modeled by:

$$\begin{cases} I_0(R) = I_0(0) \cos\left(\frac{R}{L'_0}\right) / \left[1 + \left(\frac{R}{L_0}\right)^2\right] \\ I_2(R) = I_0(0) A J_2\left(\frac{R}{L'_2}\right) / \left[1 + \left(\frac{R}{L_2}\right)^2\right] \end{cases} \quad (1.43)$$

where J_2 is the Bessel function of second order and the first kind. On the right is represented the absolute error between the numerical (equation (1.41)) and modeled results as a function of the distance R , and the wind direction ϕ . We observe that the absolute error is very small. For modeling, the autocorrelation must be even and derivable at zero with respect to R . These conditions were not verified in [15].

In figure 1.16 the parameters $P_i = \{I_0(0), L_0, L'_0, A, L_2, L'_2\}$ are represented as functions of the speed u_{10} , defined at an altitude of ten meters above the sea. We notice a straight line with logarithmic scales, so P_i can be written:

$$P_i = a_i \cdot u_{10}^{b_i} \quad \text{with} \quad u_{10} \in [2; 17] \text{ m/s} \quad (1.44)$$

where the constants $\{a_i, b_i\}$ are given in table 1.3. and are obtained from the mean square method. In the same figure the new values are plotted. Since the root mean square RMS is small, the approximation by (1.44) of the different parameters $\{a_i, b_i\}$ is correct.

We notice that the height variance $\omega^2 = I_0(0)$ is proportional to the fourth power of the wind speed u_{10} . This value checks the given result in table 1.3, where $\omega^2 = 0,00193/k_p^2 = 4,011 \times 10^{-5} u_{10}^4$ has been found from gravity waves, instead of $3,953 \times 10^{-5} u_{10}^{4,04}$ for the totality spectrum. The correlation length L_0 is proportional to the square of u_{10} . The autocorrelation function is:

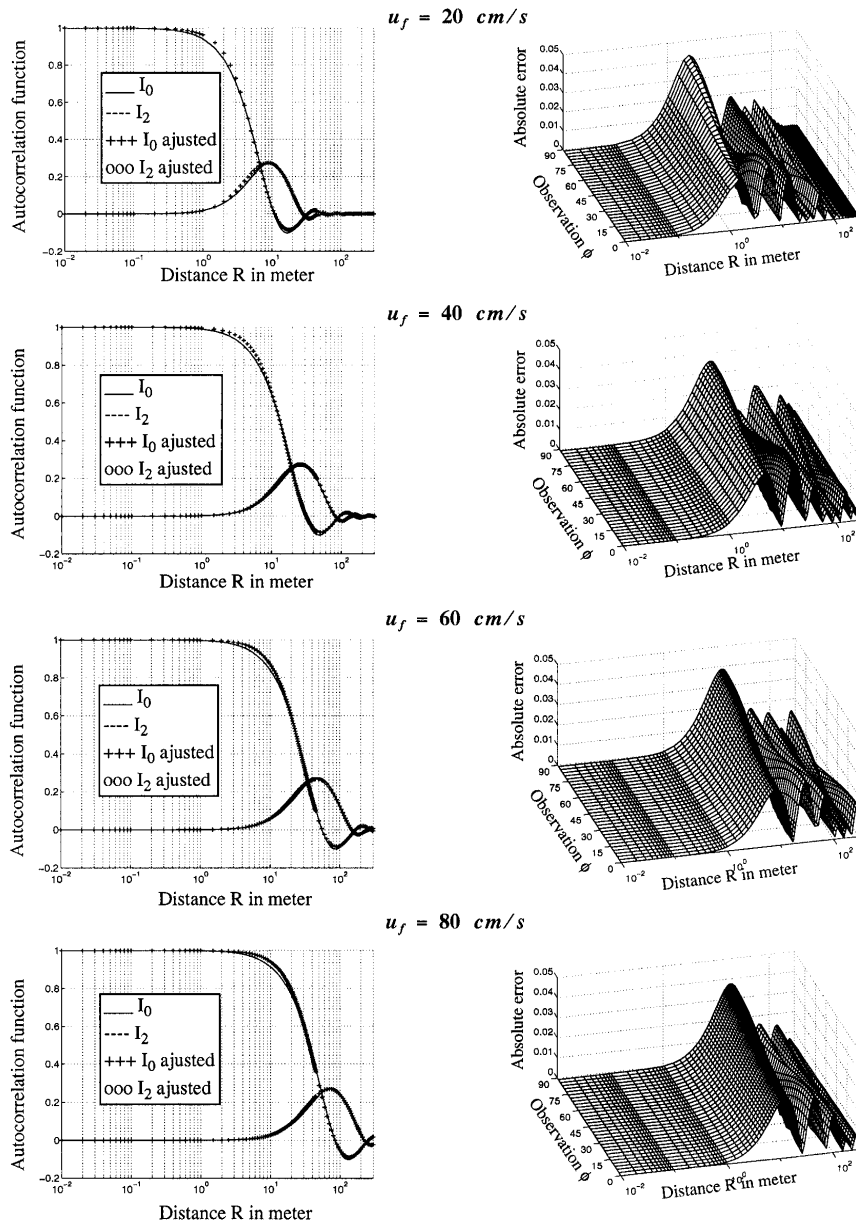


Figure 1.15 On the left, $\{I_0(R), I_2(R)\}$ are plotted as a function of R . On the right, the absolute error between the numerical and modeled results are represented as a function of the distance R , and the direction ϕ .

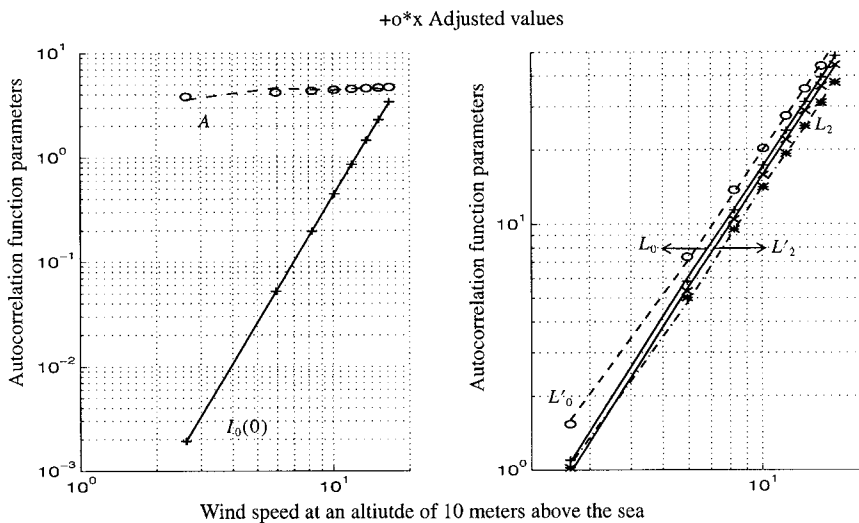


Figure 1.16 Autocorrelation function parameters as functions of the friction speed.

Table 1.3 Function autocorrelation parameters.

P_i	$I_0(0) = \omega^2$	L_0	L'_0	A	L_2	L'_2
a_i	$3,953 \times 10^{-5}$	0,154	0,244	3,439	0,157	0,138
b_i	4,04	2,04	1,91	0,11	1,95	2,05
RMS in %	0,4	1,0	2,1	3,5	1,9	1,1

$$R_0(R, \phi; u_{10}) = \omega^2 \left\{ \cos\left(\frac{R}{L_0}\right) / \left[1 + \left(\frac{R}{L_0}\right)^2\right] - A \cos(2\phi) J_2\left(\frac{R}{L'_2}\right) / \left[1 + \left(\frac{R}{L'_2}\right)^2\right] \right\} \quad (1.45)$$

In order to quantify the anisotropic effect of the autocorrelation function, we show that the maximum of $I_2(R)/\omega^2$ at abscissa R_{2M} of ordered I_{2M} which is nil at abscissa R_{20} is a function of the correlation length L_0 (in meter):

$$R_{2M} \approx 1,50L_0 \quad I_{2M} \approx 0,28 \quad R_{20} \approx 4,57L_0 \quad (1.45a)$$

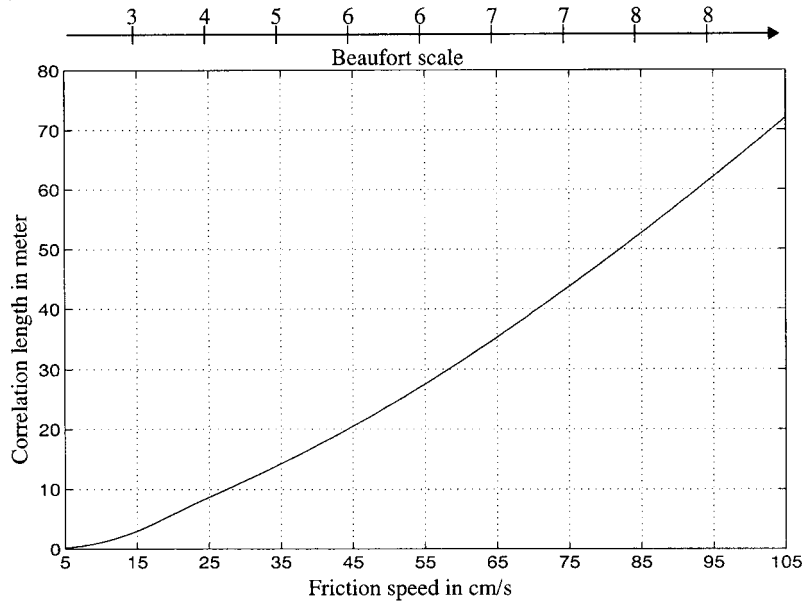


Figure 1.17 the correlation length is plotted as a function of the friction speed or the Beaufort scale.

In figure 1.17 the correlation length is plotted as a function of the friction speed or the Beaufort scale.

1.5.1.4 Conclusion

The behavior of the spatial autocorrelation function of the heights is modeled by a damped lorentzian for the isotropic part, whereas the anisotropic part is characterized by the product of the Bessel function (second order and first kind) and a lorentzian (equation (1.45)). The different lengths depend on the speed u_{10} defined at an altitude of ten meters above the sea (table 1.3). They are approximately proportional to the square of u_{10} , whereas the height variance ω^2 is function of the fourth power of u_{10} . For the Apel and Pierson spectra, we find the same autocorrelation function as Elfouhaily, but the parameters of table 1.3 change slightly. Physically, the shift of the spectrum centered on the wave number k_{peak} involves that the autocorrelation function is equal to zero for a given abscissa.

The gaussian and exponential autocorrelation functions [16] overestimate the low-frequency spectrum, because the Fourier transform

is gaussian and lorentzian respectively [8]. The calculus of the shadowing function requires the knowledge of the autocorrelation function and the slope probability density.

1.5.2 Slope Variances

To characterize a second order stationary process, we have to know its autocorrelation function and the slope statistical $p(\gamma_x, \gamma_y)$ supposed to be gaussian:

$$p(\gamma_x, \gamma_y) = \frac{1}{2\pi\sqrt{\sigma_x^2\sigma_y^2 - \sigma_{xy}^4}} \exp\left(-\frac{1}{2}[\gamma_x\gamma_y] \begin{bmatrix} \sigma_x^2 & \sigma_{xy}^2 \\ \sigma_{xy}^2 & \sigma_y^2 \end{bmatrix}^{-1} \begin{bmatrix} \gamma_x \\ \gamma_y \end{bmatrix}\right) \quad (1.46)$$

$$\begin{aligned} \sigma_x^2 &= \left. \frac{\partial^2}{\partial x^2}[-P(x, y)] \right|_{\substack{x=0 \\ y=0}} \\ \sigma_y^2 &= \left. \frac{\partial^2}{\partial y^2}[-P(x, y)] \right|_{\substack{x=0 \\ y=0}} \\ \sigma_{xy}^2 &= \left. \frac{\partial^2}{\partial x \partial y}[-P(x, y)] \right|_{\substack{x=0 \\ y=0}} \end{aligned} \quad (1.46a)$$

where $P(x, y)$ is the slope autocorrelation function, $\{\sigma_x^2, \sigma_y^2\}$ are the slope variances in the upwind and crosswind directions, and is σ_{xy}^2 the crossvariance. The spectrum is even with respect to $\{x, y\}$, the autocorrelation function is also even, so P (or H) depend on $X = x^2$, $Y = y^2$, then, we show:

$$\sigma_{xy}^2 = \left. \frac{\partial^2}{\partial x \partial y}[-P(x^2, y^2)] \right|_{\substack{x=0 \\ y=0}} = 4xy \left. \frac{\partial^2}{\partial X \partial Y}[-P(XY)] \right|_{\substack{x=0 \\ y=0}} = 0 \quad (1.46b)$$

If $\{X = |x|, Y = |y|\}$, the autocorrelation function is even, but is not derivable at zero. So, we have to give up this solution. Substituting, equation (1.46b) into (1.46), $p(\gamma_x, \gamma_y)$

$$p(\gamma_x, \gamma_y) = \frac{1}{2\pi\sigma_x\sigma_y} \exp\left(-\frac{\gamma_x^2}{2\sigma_x^2} - \frac{\gamma_y^2}{2\sigma_y^2}\right) \quad (1.46c)$$

1.5.2.1 The Variance Definition and Angular Integration

The slope autocorrelation functions $\{P_x(R, \phi; \tau); P_y(R, \phi; \tau)\}$ in the upwind and crosswind directions $\{x, y\}$ are in polar coordinates respectively [6]:

$$\left\{ \begin{array}{l} P_x(R, \phi; \tau) = \int\limits_{0-\pi}^{\infty} \int\limits_{-\pi}^{\pi} S(k, \Theta) [k \times \cos(\Theta - \phi)]^2 \\ \quad \cdot \cos[kR \cos(\Theta - \phi) - \omega\tau] d\Theta dk \\ P_y(R, \phi; \tau) = \int\limits_{0-\pi}^{\infty} \int\limits_{-\pi}^{\pi} S(k, \Theta) [k \times \sin(\Theta - \phi)]^2 \\ \quad \cdot \cos[kR \cos(\Theta - \phi) - \omega\tau] d\Theta dk \end{array} \right. \quad (1.47)$$

The slope variances are defined for $\{\tau = 0, R = 0, \phi = 0\}$:

$$\begin{aligned} \sigma_x^2 &= \int\limits_{0-\pi}^{\infty} \int\limits_{-\pi}^{\pi} S(k, \Theta) [k \times \cos \Theta]^2 d\Theta dk \\ \sigma_y^2 &= \int\limits_{0-\pi}^{\infty} \int\limits_{-\pi}^{\pi} S(k, \Theta) [k \times \sin \Theta]^2 d\Theta dk \end{aligned} \quad (1.48)$$

Using the symmetry of the spectrum $S(k, \Theta)$ (equation (1.36)), we show that the integration of the variance over Θ gives:

$$\left\{ \begin{array}{l} \sigma_x^2 = \alpha + \beta \\ \sigma_y^2 = \alpha - \beta \end{array} \right. \quad \text{with} \quad \left\{ \begin{array}{l} \alpha = \frac{1}{2} \int\limits_0^{\infty} k^2 \times M(k) dk \\ \beta = \frac{1}{4} \int\limits_0^{\infty} k^2 \times M(k) \Delta dk \end{array} \right. \quad (1.49)$$

The slope variances are obtained from the integration of the spectrum $M(k)$ multiplied by the squared wave number.

1.5.2.2 Numerical Integration over the Wave Number

In the case of slopes, the studied spectrum is $k^2 M(k)$. Gravity waves determine the lower value of the numerical integration. Applying

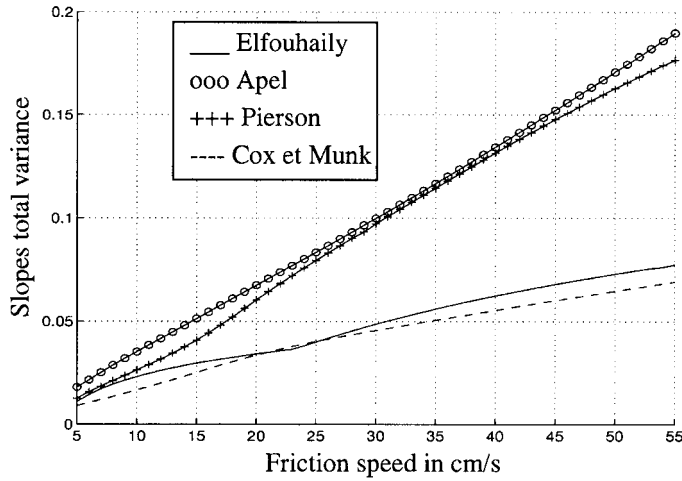


Figure 1.18 Slope total variance calculated from the Elfouhaily, Apel, Pierson spectra and the Cox-Munk, model as a function of the friction speed.

the same approach as in paragraph 1.5.1.3, the value k_1 reaching the value of 10^{-5} of the maximum is equal to:

$$k_1 = 0,29k_p \quad (1.50)$$

Unlike the height variance, capillary wave is not negligible. The superior boundary k_2 is chosen to 10^{-4} of the maximum:

$$k_2 = 2000 \text{ rad/m} \quad (1.50a)$$

1.5.2.3 Simulations

In figure 1.18 the Elfouhaily, Apel and Pierson total variance equal to $\sigma_x^2 + \sigma_y^2 = 2\alpha$ [17] is plotted as a function of the friction speed. It also represents the Cox and Munk model obtained from aerial photographs [18]:

$$\begin{cases} \sigma_x^2 = 3,16 \times 10^{-3} \cdot u_{12} \\ \sigma_y^2 = 0,003 + 1,92 \times 10^{-3} \cdot u_{12} \end{cases} \quad (1.51)$$

where u_{12} is the wind speed in m/s, at an altitude 12,5 m above the sea.

We observe that the Apel and Pierson models overestimate the slope total variance, because they have an inaccurate gravity wave, whereas the Elfouhaily results agree with Cox and Munk ones.

1.6 CONCLUSION

The ocean presents an uncoordinate aspect, so the fluctuations of the sea are represented by a three dimensional random variable: one temporal and two spatial components. This process is also supposed to be ergodic and stationary. The stationarity involves that the autocorrelation function is obtained from the spectrum by an inverse Fourier transform. Moreover, we suppose that the density probability of the heights is gaussian characterized by its variances and its mean values. The linearity of this process involves a gaussian distribution of the slopes.

The main difficulty is the determination of the sea spectra. In the literature, the JONSWAP and Pierson spectra are widely used to describe gravity waves. For capillary waves, the Pierson-Moskowitz spectrum is the most used. Recently these models have been improved. The Apel and Elfouhaily spectra are a synthesis of works done in 80's and between 1990 and 1996 respectively.

Generally spectra depend on the wave number, the wind speed and the fetch. Another characteristic of the spectrum is its angular distribution, which gives the waves energetic spreading as a function of the wind direction.

The slope variances have been calculated analytically and simulated in order to compare with different sea spectra (Elfouhaily, Apel, Pierson), and the Cox and Munk model. The Elfouhaily results are close to Cox and Munk ones, whereas for both other spectral configurations, the results are very different, due to inaccuracy in capillary zone.

Finally, the spatial autocorrelation function of the heights has been modeled from the Elfouhaily spectrum. Its behavior is a damped lorentzian for its isotropic part, whereas its anisotropic part is characterized by the product of a Bessel function (second order and the first kind) and a lorentzian (equation (1.45)). Their variations are represented In figure 1.19. For the Apel and Pierson spectra, the autocorrelation function is the same as obtained from the Elfouhaily spectrum, but the parameters change slightly.

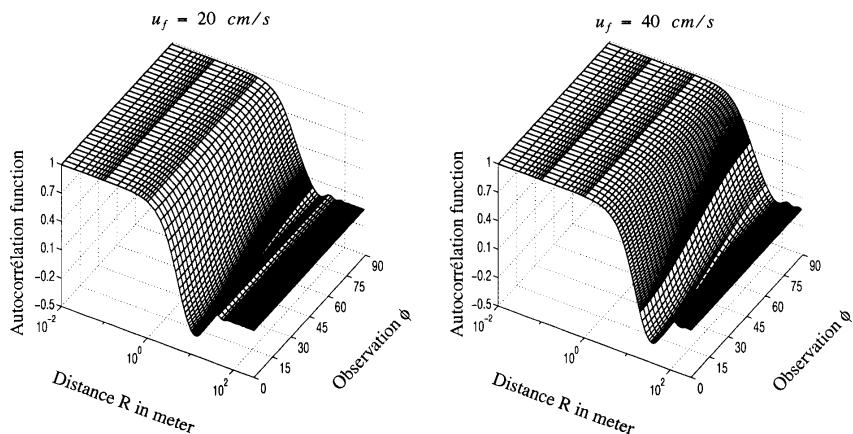


Figure 1.19 Modeled autocorrelation function from the Elfouhaily spectrum, as a function of the wind direction ϕ , for a given friction speed u_f .

2. THE SHADOWING FUNCTION

2.1 INTRODUCTION

The goal of this chapter is to generalize the methods developed by Wagner [19] and Smith [20, 21] concerning the calculus of the shadowing function and to extend them to the two-dimensional case. Their approach is rigorously studied, in order to quantify the hypothesis introduced by these authors, since the shadowing function is a relevant parameter introduced in the electromagnetic scattering, emissivity, reflectivity of sea surface.

First, the Smith and Wagner models are exposed for a **monostatic** configuration, and are obtained from an **uncorrelated gaussian** process. Physically, this hypothesis involves that the shadowing function is independent of the autocorrelation function and the viewed surface is infinite. Moreover Ricciardi and Sato [25, 26] proved that the shadowing function is rigorously defined by Rice's infinite series of integrals. We observe that the approach proposed by Wagner retains only the **first** term of these series, whereas the Smith formulation uses the Wagner model by introducing a normalization function. The Wagner and Smith models are generalized for **any uncorrelated** probability

densities. The shadowing function based on the Ricciardi-Sato works is also determined to consider an **uncorrelated gaussian** process. Since the correlation is not taken into account, the result has not physical meaning.

In the second section, the Wagner and Smith formalisms are modified by introducing the **correlation**. The correlated and uncorrelated results are compared with the reference solution, obtained by generating an **infinite** surface of a gaussian process, for lorentzian and gaussian autocorrelation functions. We show that the correlation improves results and is negligible above $\mu = 2\sigma$, where μ represents the slope of the incident beam and σ the slope standard deviation. A **general** method is established for calculating the shadowing function for a **known-length** surface and, for **any** autocorrelation functions. This method is applied on damped autocorrelation functions.

In the third part, the correlated and uncorrelated results are generalized to the **bistatic** case. Finally, the **two-dimensional** shadowing functions with and without correlation are simulated for a real sea from the autocorrelation function modeled in the first chapter.

2.2 THE ONE-DIMENSIONAL MONOSTATIC SHADOWING FUNCTION WITHOUT CORRELATION

In this part, in order to introduce the Wagner and Smith hypothesis, we describe their approach for the determination of the one-dimensional shadowing function.

2.2.1 Introduction

In the monostatic case (transmitter and receiver at the same location), the shadowing function characterizes the surface fraction which is invisible from the receiver. In the bistatic case (transmitter and receiver at different location), the surface fraction is invisible from both transmitter and receiver. Work about the shadowing function has been done from the 60's, in order to determine the electromagnetic scattering from a randomly rough surface. To take into account this phenomenon, the scattered energy by the total surface is multiplied by the shadowing function S [22].

The analytic shadowing function proposed by Beckmann [23] is equal to the illuminated surface portion of the surface, and it varies from one at normal incidence to zero at grazing angle. Another shad-

owing function given by Brokelman and Hagfors [24], corresponding to ratio of illuminated point number having a specular reflexion over the entire surface points. Both authors [24] do not propose any analytic solution of the shadowing function, since their results are obtained from numerical simulations. They showed that the analytic function suggested by Beckman [23] is correct for grazing and quasi-normal incidence angles, whereas it exists a difference for intermediate values.

Today, there are two approaches developed by [19] and Smith [20, 21] in 1967 to model the shadowing function based on an identical mathematical approach about conditional probabilities.

2.2.2 The Definition of the Shadowing Function

The shadowing function is equal to the fraction of the **illuminated** surface over the total surface. For an observation length L , the shadowing function $S(\theta, F)$ is equal to the probability that an arbitrary point $F(\xi_0, \gamma_0)$ at abscissa $\tau = 0$ on a random rough surface, of given height ξ_0 above the mean plane, and with local slope $\gamma = \partial z / \partial y$ is illuminated, when the surface is crossed by an incident beam from direction θ according to the vertical z (figure 2.1):

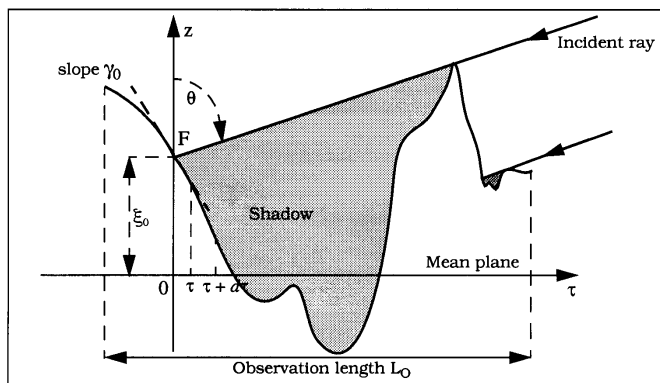


Figure 2.1 Shadowing function for a monostatic configuration.

The shadowing function for a surface length L_0 [19–21] is:

$$S(\theta, F) = \Upsilon(\mu - \gamma_0) \cdot \exp \left[- \int_0^{L_0} g(\tau|F, \theta) d\tau \right] \quad (2.1)$$

with

$$\Upsilon(\mu - \gamma_0) = \begin{cases} 0 & \text{si } \gamma_0 \geq \mu \\ 1 & \text{si } \gamma_0 < \mu \end{cases} \quad \mu = \cot \theta \quad (2.1a)$$

where $g(\tau|F, \theta)d\tau$ is the conditional probability that the ray **intercepts** the surface in the interval $[\tau; \tau + d\tau]$, knowing that it is **not cross** in the interval $[0; \tau]$. Υ is represented in figure 2.2.

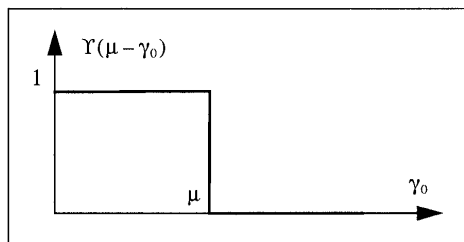


Figure 2.2 Variation of Υ .

The average shadowing function $S(\theta)$ over the slopes and heights is given by:

$$S(\theta) = \int_{-\infty}^{\infty} \int_{-\infty}^{\infty} S(\theta, F\{\xi_0, \gamma_0\}) p(\xi_0, \gamma_0) d\xi_0 d\gamma_0 \quad (2.2)$$

where $p(\xi_0, \gamma_0)$ is the joint probability density of the slopes and heights. $S(\theta)$ is the experimentally measured quantity. The main difficulties to calculate the shadowing function is based on the determination of g . The analytic expression of $g(\tau)$ is rigorously enounced by Ricciardi and Sato [25, 26], previous works has been done in 1967 by Wagner and Smith [19–21]. There are two main approaches to calculate the shadowing function, Smith and Wagner formulations are particular cases of the Ricciardi-Sato works.

2.2.3 The Wagner, Smith and Ricciardi-Sato Approaches

2.2.3.1 Wagner and Smith

The conditional probability $g(\tau|F, \theta)d\tau$ of Wagner is the conditional probability for the studied point $F(\xi_0, \gamma_0)$ to be darkened at the abscissa $\tau + d\tau$ of slope superior to the slope ray incident ($\gamma > \mu$),

conditionally to the knowledge of the studied point. Mathematically we have [19]:

$$g_W(\tau|F, \theta) = \int_{\mu}^{\infty} (\gamma - \mu) \cdot p(\xi = \xi_0 + \mu\tau, \gamma|\xi_0, \gamma_0; \tau) d\gamma \quad (2.3)$$

The conditional probability $g(\tau|F, \theta)d\tau$ of Smith is the conditional probability for the studied point $F(\xi_0, \gamma_0)$ to be darkened at the abscissa $\tau + d\tau$ (circumstance of Wagner) knowing it is not cut it by the abscissa surface τ . It is given by [20, 21]:

$$\begin{aligned} g_S(\tau|F, \theta) &= \frac{\int_{\mu}^{\infty} (\gamma - \mu) \cdot p(\xi = \xi_0 + \mu\tau, \gamma|\xi_0, \gamma_0; \tau) d\gamma}{\int_{-\infty}^{\infty} d\gamma \int_{-\infty}^{\xi_0 + \mu\tau} p(\xi, \gamma|\xi_0, \gamma_0; \tau) d\xi} \\ &= \frac{g_W(\tau|F, \theta)}{\int_{-\infty}^{\infty} d\gamma \int_{-\infty}^{\xi_0 + \mu\tau} p(\xi, \gamma|\xi_0, \gamma_0; \tau) d\xi} \end{aligned} \quad (2.4)$$

Smith uses the Wagner formulation combined with a normalization function.

2.2.3.2 Ricciardi-Sato

Ricciardi and Sato give the rigorous expression of the function g without any hypothesis [25, 26]:

$$\begin{aligned} g_R(\tau|F, \theta) &= W_1(\tau|F, \theta) - \int_0^{\tau} W_2(\tau_1, \tau|F, \theta) d\tau_1 \\ &\quad + \int_0^{\tau} d\tau_1 \int_{\tau_1}^{\tau} W_3(\tau_2, \tau_1, \tau|F, \theta) d\tau_2 \\ &\quad - \dots + (-1)^{n-1} \int_0^{\tau} d\tau_1 \int_{\tau_1}^{\tau} d\tau_2 \dots \int_{\tau_{n-3}}^{\tau} d\tau_{n-2} \end{aligned}$$

$$\cdot \int_{\tau_{n-2}}^{\tau} W_n(\tau_{n-1}, \tau_{n-2}, \dots, \tau_1, \tau | F, \theta) d\tau_{n-1} \quad (2.5)$$

$$W_n(\tau_{n-1}, \tau_{n-2}, \dots, \tau_1, \tau | F, \theta) = \int_{\mu}^{\infty} d\gamma_1 \int_{\mu}^{\infty} d\gamma_2 \dots \int_{\mu}^{\infty} d\gamma_n \prod_{i=1}^n (\gamma_i - \mu) \cdot p_{2n+2}(\vec{S}, \vec{G} | \xi_0, \gamma_0; \tau) \quad n \geq 2 \quad (2.5a)$$

where $W_n(\tau_{n-1}, \tau_{n-2}, \dots, \tau_1, \tau | F, \theta) d\tau_{n-1} d\tau_{n-2} \dots d\tau_2 d\tau_1$ is the joint probability that the incident ray of equation $S_n = \xi_0 + \mu l_n$ ($\mu = \cot \theta$) crosses the surface $\xi(\tau_n)$, with a slope μ inferior to the slope γ_n of at abscissa τ_n , in the intervals $\{[\tau_1; \tau_1 + d\tau_1], [\tau_2; \tau_2 + d\tau_2], \dots, [\tau_{n-1}; \tau_{n-1} + d\tau_{n-1}]\}$, conditionally to the knowledge of $F(\xi_0, \gamma_0)$. The joint probability density of vectors $\vec{S}^T = [S_1, S_2, \dots, S_n]$ and $\vec{G}^T = [\gamma_1, \gamma_2, \dots, \gamma_n]$ at abscissa points $\{\tau_1, \tau_2, \dots, \tau_n\}$ knowing $\{\xi_0, \gamma_0\}$ is $p_{2n+2}(\vec{S}, \vec{G} | \xi_0, \gamma_0; \tau)$. The problem is slightly different from these presented by Ricciardi and Sato, because the probability density p_{2n+2} is conditioned in our case by the variables $\{\xi_0, \gamma_0\}$, whereas they only consider the term ξ_0 .

The Wagner formulation is obtained for $n = 1$ and $\gamma = \gamma_1$.

2.2.4 Application for an Uncorrelated Process of the Infinite Surface

The different formulations of the function g are applied for an **uncorrelated** process, and for an **infinite observation length**. We calculate the average shadowing function, given by (equation (2.1) into (2.2) with $L_0 \rightarrow \infty$):

$$S(\theta) = S(\theta)_{L_0 \rightarrow \infty} = \int_{-\infty}^{\infty} \int_{-\infty}^{\mu} p(\xi_0, \gamma_0) \cdot \exp\left(-\int_0^{\infty} g(\tau | F, \theta) d\tau\right) d\xi_0 d\gamma_0 \quad (2.6)$$

$S(\theta)$ is first determined in the Wagner and Smith cases, for **any** uncorrelated process, and the results are then compared with Ricciardi-Sato ones, for uncorrelated **gaussian** process.

2.2.4.1 Wagner and Smith

The Wagner and Smith shadowing functions calculated in appendix 1 are valid for an **any** uncorrelated process, and for an infinite observation length:

$$\begin{cases} S_W(v) = \Lambda' \times \frac{1 - e^{-\Lambda}}{\Lambda} \\ S_S(v) = \Lambda' \times \frac{1}{\Lambda + 1} \end{cases} \begin{cases} \Lambda = \frac{1}{\mu} \int_{\mu}^{\infty} (\gamma - \mu) p(\gamma) d\gamma & \Lambda' = \int_{-\infty}^{\mu} p(\gamma) d\gamma \\ v = \mu / (\sigma\sqrt{2}) = \cot \theta / (\sigma\sqrt{2}) \end{cases} \quad (2.7)$$

where $p(\gamma)$ is the slope density probability. The general expression of $S_S(v)$ is identical to [27]. According to the following inequalities:

$$\frac{x}{1+x} < 1 - e^{-x} < x \quad \text{and} \quad x > 0 \quad \Rightarrow \quad \frac{1}{1+x} < \frac{1 - e^{-x}}{x} < 1 \quad (2.7a)$$

we have:

$$\frac{1}{1+\Lambda} < \frac{1 - e^{-\Lambda}}{\Lambda} < 1 \quad \Rightarrow \quad S_S(v) < S_W(v) < \Lambda' < 1 \quad (2.8)$$

with $\Lambda > 0$. The Smith shadowing function is then always inferior to the Wagner one.

2.2.4.2 Ricciardi-Sato

We show in appendix 2 that the Ricciardi-Sato shadowing function for an uncorrelated **gaussian** process and for an infinite observation length is:

$$S_R(v) = \left[1 - \frac{\text{erfc}(v)}{2} \right] \left[\frac{E_1(-e^{-\Lambda}) - E_1(-1)}{\Lambda e^1} \right] \begin{cases} E_1(x) = \int_1^{\infty} \frac{e^{-xt}}{t} dt \\ v = \frac{\mu}{\sqrt{2}\sigma} = \frac{\cot \theta}{\sqrt{2}\sigma} \end{cases} \quad (2.9)$$

where σ^2 is the slope variance.

2.2.4.3 Simulation on a Gaussian Process

In the gaussian case, the probability density is written:

$$p(\gamma) = \frac{1}{\sigma\sqrt{2\pi}} \exp\left(-\frac{\gamma^2}{2\sigma^2}\right) \quad (2.10)$$

Substituting equation (2.10) into (2.7), the Wagner and Smith shadowing functions for an uncorrelated gaussian process are:

$$\left\{ \begin{array}{l} S_W(v) = \Lambda' \times \frac{1 - e^{-\Lambda}}{\Lambda} \\ S_S(v) = \Lambda' \times \frac{1}{\Lambda + 1} \end{array} \right. \text{ with } \left\{ \begin{array}{l} \Lambda = \left[e^{-v^2} - v\sqrt{\pi}\text{erfc}(v) \right] / (2v\sqrt{\pi}) \\ \Lambda' = 1 - \frac{1}{2}\text{erfc}(v) \quad v = \frac{\mu}{\sqrt{2}\sigma} \end{array} \right. \quad (2.11)$$

For an uncorrelated gaussian process, the shadowing functions $\{S_W(\theta), S_S(\theta), S_R(\theta)\}$ given by equations (2.11) and (2.9) depend only on parameter v equal to the ratio of the incident ray slope over the surface standard deviation, multiplied by $\sqrt{2}$. In figure 2.3 the shadowing functions are plotted as a function of v . We observe that Smith's results are inferior to Wagner's and verify equation (2.8). The Wagner and Ricciardi-Sato curves have an identical behavior for $v \geq 0,6$, whereas they differ for smaller values, corresponding to incidence angles close to 90° . Indeed:

$$S_R(0) = e^{-1}/2 = 0,184 \quad \text{and} \quad S_W(0) = 0 \quad (2.12)$$

Physically the shadowing function is equal to zero at a grazing angle of 90° . So, when the correlation is not included, the Sato-Ricciardi results do not give satisfying results at grazing angles, whereas the Wagner results are correct but overestimate the shadowing function. The modeling of this phenomenon being inaccurate, it is then essential to include the correlation. Unfortunately the complexity of equation (2.5) does not allow to analytically determine the function g_R . Nevertheless, the analytic calculus of the Wagner and Smith uncorrelated functions g are possible.

2.3 THE ONE-DIMENSIONAL MONOSTATIC SHADOWING FUNCTION WITH CORRELATION

The goal of this part, is to quantify the hypothesis introduced by Smith and Wagner for the determination of the monostatic one-dimensional shadowing function. They assume that the joint probability density of the slopes and heights is **uncorrelated**, involving that the shadowing function is independent of the autocorrelation function. The Wagner and Smith approaches are applied for a **correlated** gaussian process.

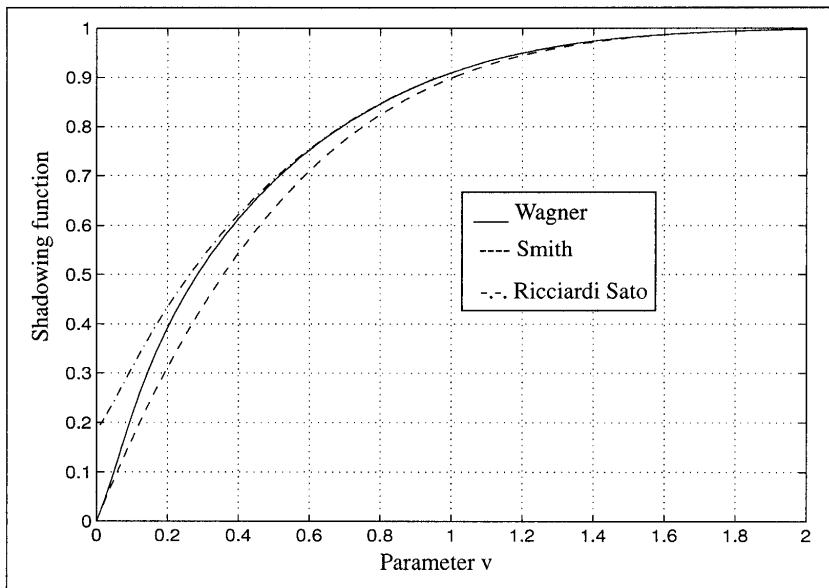


Figure 2.3 The Wagner, Smith and Ricciardi-Sato shadowing functions as a function of v .

2.3.1 Expressions of the Wagner and Smith Conditional Probabilities

This part gives the theoretical expressions of the Wagner and Smith **correlated** conditional probabilities, for a **given observation length**.

2.3.1.1 Wagner

We show that the joint probability $p(\xi, \gamma | \xi_0, \gamma_0; \tau)$ expression is (appendix 3):

$$\begin{aligned}
 p(\xi, \gamma | \xi_0, \gamma_0; \tau) = & \frac{\sigma\omega}{2\pi\sqrt{|[C]|}} \times \exp \left[-\frac{C_{i11}(\xi_0^2 + \xi^2) + C_{i33}(\gamma_0^2 + \gamma^2)}{2|[C]|} \right. \\
 & + \frac{\xi_0^2}{2\omega^2} + \frac{\gamma^2}{2\sigma^2} \\
 & \left. - \frac{2C_{i12}\xi_0\xi + 2C_{i34}\gamma_0\gamma + 2C_{i13}(\xi_0\gamma_0 - \xi\gamma) + 2C_{i14}(\xi_0\gamma - \xi\gamma_0)}{2|[C]|} \right]
 \end{aligned}
 \tag{2.13}$$

and

$$\begin{cases} C_{i11} = \omega^2 (\sigma^4 - R_2^2) - R_1^2 \sigma^2 \\ C_{i12} = R_0 (R_2^2 - \sigma^4) - R_1^2 R_2 \\ C_{i13} = -R_1 (R_0 \sigma^2 + \omega^2 R_2) \end{cases} \quad \begin{cases} C_{i14} = R_1 (R_1^2 - R_0 R_2 - \omega^2 \sigma^2) \\ C_{i33} = \sigma^2 (\omega^4 - R_0^2) - R_1^2 \omega^2 \\ C_{i34} = R_2 (\omega^4 - R_0^2) + R_1^2 R_0 \end{cases}$$

$$|[C]| = \frac{C_{i33}^2 - C_{i34}^2}{\omega^4 - R_0^2} \quad (2.13a)$$

where R_0 is the autocorrelation function assumed **even** and **derivable at the origin**, and $\{R_1, R_2\}$ are its first and second derivatives. The height variance ω^2 is equal to $R_0(0)$ and the slope variance σ^2 is $-R_2(0)$. $|[C]|$ is the determinant of the covariance matrix $[C]$. The first index i in C_{ij} denotes the elements of the inverse matrix $[C]^{-1}$.

From equation (2.3), the Wagner conditional probability $g_W(\tau|F, \theta)$ is:

$$g_W(\tau|F, \theta) = \frac{\sigma \omega \exp[-D - \mu(\mu A + 2B)]}{4\pi A \sqrt{|[C]|}} \cdot \left[1 - e^{\frac{(B+\mu A)^2}{A}} \sqrt{\pi} \frac{B + \mu A}{\sqrt{A}} \operatorname{erfc} \left(\frac{B + \mu A}{\sqrt{A}} \right) \right] \quad (2.14)$$

with

$$\begin{cases} A = \frac{C_{i33}}{2|[C]|} \\ B = \frac{\xi_0 C_{i14} - \xi C_{i13} + \gamma_0 C_{i34}}{2|[C]|} \quad \xi = \xi_0 + \mu\tau \\ D = \frac{(\xi_0^2 + \xi^2) C_{i11} + 2\xi_0 \xi C_{i12} + 2\gamma_0 (\xi_0 C_{i13} - \xi C_{i14}) + \gamma_0^2 C_{i33}}{2|[C]|} \\ \quad - \frac{\xi_0^2}{2\omega^2} - \frac{\gamma_0^2}{2\sigma^2} \end{cases} \quad (2.14a)$$

2.3.1.2 Smith

From equations (2.4) and (2.13), the Smith conditional probability is given by:

$$g_S(\tau|F, \theta) = \frac{1}{\pi} \sqrt{\frac{A_1}{A}} \times \left(\frac{\exp \left[-D - \mu(\mu A + 2B) - \frac{\xi_0^2}{2\omega^2} - \frac{\gamma_0^2}{2\sigma^2} \right] \times \left[1 - e^{\frac{(B+\mu A)^2}{A}} \sqrt{\pi} \frac{B + \mu A}{\sqrt{A}} \operatorname{erfc} \left(\frac{B + \mu A}{\sqrt{A}} \right) \right]}{\exp \left(\frac{B_1^2}{A_1} - C_1 \right) \left\{ \operatorname{erf} \left(\frac{A_1 \xi + B_1}{\sqrt{A_1}} \right) + 1 \right\}} \right) \quad (2.15)$$

$$\begin{cases} A_1 = (C_{i11}C_{i33} - C_{i13}^2) E_1 & E_1 = \frac{1}{2C_{i33}|[C]|} \\ B_1 = [\xi_0 (C_{i12}C_{i33} + C_{i14}C_{i13}) + \gamma_0 (C_{i13}C_{i14} - C_{i14}C_{i34})] E_1 \\ C_1 = [\xi_0^2 (C_{i11}C_{i33} - C_{i14}^2) + \gamma_0^2 (C_{i33}^2 - C_{i34}^2) \\ \quad + 2\xi_0\gamma_0 (C_{i13}C_{i33} - C_{i14}C_{i34})] E_1 \end{cases} \quad (2.15a)$$

The function introduced in the denominator of equation (2.15) represents the Smith normalization.

2.3.1.3 Conclusion

The Wagner and Smith classical shadowing functions assume that the correlation is null, involving (equation (2.13)):

$$\begin{cases} R_0 = 0 \\ R_1 = 0 \\ R_2 = 0 \end{cases} \Rightarrow \begin{cases} C_{i12} = 0 \\ C_{i13} = 0 \\ C_{i14} = 0 \\ C_{i34} = 0 \end{cases} \quad \text{and} \quad (2.16)$$

$$\begin{cases} |[C]| = \sigma^4 \omega^4 \\ C_{i11} = \sigma^4 \omega^2 \\ C_{i33} = \sigma^2 \omega^4 \end{cases} \Rightarrow \begin{cases} A = 1/(2\sigma^2) \\ B = 0 \\ D = \xi^2/(2\omega^2) \end{cases} \quad \begin{cases} A_1 = 1/(2\omega^2) \\ B_1 = 0 \\ C_1 = \frac{\xi_0^2}{2\omega^2} + \frac{\gamma_0^2}{2\sigma^2} \end{cases}$$

Substituting relations (2.16) into (2.14) and (2.15), the Wagner and Smith uncorrelated conditional probabilities are:

$$\begin{cases} g_W(\tau|F, \theta) = \Lambda \mu \frac{1}{\omega \sqrt{2\pi}} \exp \left(-\frac{\xi^2}{2\omega^2} \right) \\ g_S(\tau|F, \theta) = g_W(\tau|F, \Theta) \frac{2}{1 + \operatorname{erf}(\xi/[\sqrt{2}\omega])} \geq g_W(\tau|F, \Theta) \end{cases} \quad (2.16a)$$

The conditional probability depends on $\{\omega, \sigma\}$. In the gaussian and lorentzian cases (table 2.1) the value of $\{\omega, \sigma\}$ are equal, involving an identical shadowing function. On the contrary, when the correlation is included, the shadowing functions are not equal, due to the functions $\{R_0, R_1, R_2\}$ which are different in each case.

Table 2.1 Gaussian and lorentzian autocorrelation functions.

	Functions R_0 and f_0	Functions R_1 and f_1	Functions R_2 and f_2	Standard Deviation of slopes σ
Gaussian	$R_0 = \omega^2 e^{-\frac{\tau^2}{L^2}}$ $f_0 = e^{-y^2}$	$R_1 = -\frac{2\omega^2}{L} \frac{\tau}{L} e^{-\frac{\tau^2}{L^2}}$ $f_1 = \sqrt{2} y e^{-y^2}$	$R_2 = -\frac{2\omega^2}{L^2} e^{-\frac{\tau^2}{L^2}} \left(1 - 2\frac{\tau^2}{L^2}\right)$ $f_2 = e^{-y^2} (1 - 2y^2)$	$\sigma = \frac{\omega\sqrt{2}}{L}$ $\eta = \frac{\sigma L}{\omega} = \sqrt{2}$
Lorentzian	$R_0 = \frac{\omega^2}{1 + \frac{\tau^2}{L^2}}$ $f_0 = \frac{1}{1 + y^2}$	$R_1 = -\frac{2\omega^2}{L} \frac{\tau}{L \left(1 + \frac{\tau^2}{L^2}\right)^2}$ $f_1 = \frac{y\sqrt{2}}{(1 + y^2)^2}$	$R_2 = -\frac{2\omega^2}{L^2} \frac{1 - 3\frac{\tau^2}{L^2}}{\left(1 + \frac{\tau^2}{L^2}\right)^3}$ $f_2 = \frac{1 - 3y^2}{(1 + y^2)^3}$	$\sigma = \frac{\omega\sqrt{2}}{L}$ $\eta = \frac{\sigma L}{\omega} = \sqrt{2}$

2.3.2 Expressions of the Wagner and Smith Shadowing Functions

In this part, we show that the Wagner and Smith averaged one-dimensional monostatic shadowing functions only depend on one parameter $v = \mu/(\sigma\sqrt{2})$ whatever the autocorrelation function. μ is the slope of the incident beam and σ the slope standard deviation. The introduction of the variable v permits to reduce the number of degrees of freedom from two $\{\theta, \sigma\}$ to one v .

2.3.2.1 The Wagner and Smith Averaged Shadowing Functions

In order to give the shadowing function as a function of v , define the following relations:

$$R_0 = \omega^2 f_0 \quad R_1 = -\sigma\omega f_1 \quad R_2 = -\sigma^2 f_2 \quad (2.17)$$

$\{R_1; R_2\}$ are set to negative sign so that the functions $\{f_1; f_2\}$ are positive at the neighborhood of zero. Substituting equations (2.17)

into (2.13a), we show:

$$\left\{ \begin{array}{l} \frac{C_{i11}}{2|[C]|} = \frac{1}{2\omega^2} \cdot \frac{f_{11}}{f_M} \\ \frac{C_{i12}}{2|[C]|} = \frac{1}{2\omega^2} \cdot \frac{f_{12}}{f_M} \\ \frac{C_{i33}}{2|[C]|} = \frac{1}{2\sigma^2} \cdot \frac{f_{33}}{f_M} \\ \frac{C_{i34}}{2|[C]|} = \frac{1}{2\sigma^2} \cdot \frac{f_{34}}{f_M} \\ \frac{C_{i13}}{2|[C]|} = \frac{1}{2\sigma\omega} \cdot \frac{f_{13}}{f_M} \\ \frac{C_{i14}}{2|[C]|} = \frac{1}{2\sigma\omega} \cdot \frac{f_{14}}{f_M} \end{array} \right. \quad \text{with} \quad \left\{ \begin{array}{l} f_M = \frac{f_{33}^2 - f_{34}^2}{1 - f_0^2} = \frac{|[C]|}{(\omega\sigma)^4} \\ f_{11} = 1 - f_2^2 - f_1^2 \\ f_{12} = f_0 f_2^2 + f_1^2 f_2 - f_0 \\ f_{33} = 1 - f_0^2 - f_1^2 \\ f_{34} = f_0^2 f_2 + f_1^2 f_0 - f_2 \\ f_{13} = f_1(f_0 - f_2) \\ f_{14} = f_1(1 - f_1^2 - f_0 f_2) \end{array} \right. \quad (2.17a)$$

For a finite surface L_0 the shadowing function is (equation (2.1)):

$$S(\theta, F) = \Upsilon(\mu - \gamma_0) \cdot \exp \left[- \int_0^{L_0} g(\tau|F, \theta) d\tau \right] \quad (2.17b)$$

For a **gaussian** process, the average shadowing function over the slopes and heights is:

$$S(\theta) = \frac{1}{2\pi\sigma\omega} \int_{-\infty}^{\infty} \int_{-\infty}^{\mu} \exp \left(- \frac{\xi_0^2}{2\omega^2} - \frac{\gamma_0^2}{2\sigma^2} \right) \cdot \exp \left(- \int_0^{L_0} g(\tau|F\{\xi_0, \gamma_0\}, \theta) d\tau \right) d\xi_0 d\gamma_0 \quad (2.18)$$

Performing the following variable transformation:

$$h_0 = \frac{\xi_0}{\sqrt{2}\omega} \quad \frac{\gamma_0}{\sqrt{2}\sigma} = v - p_0 \quad y = \frac{\tau}{L} \quad (2.18a)$$

where L is the length of correlation, we have:

$$S(v) = \frac{1}{\pi} \int_{-\infty}^{\infty} \int_0^{\infty} \exp [-h_0^2 - (v - p_0)^2] \cdot \exp \left[-L \int_0^{y_0} g(y|F\{h_0, p_0\}, \theta) dy \right] dh_0 dp_0 \quad (2.19)$$

The variable transformation allows to reduce the integration boundaries, then:

$$\begin{cases} -\infty < h_0 < \infty \rightarrow -3 < h < 3 & \text{due to } \exp(-3^2) = 1,23 \times 10^{-4} \\ 0 < p_0 < \infty \rightarrow 0 < p < 3 + v & \text{due to } \exp(-3^2) = 1,23 \times 10^{-4} \end{cases} \quad (2.19a)$$

When the normalized observation length y_0 is infinite, the integration domain of the function g is contained between zero and infinite. In order to reduce this domain, the integral is split in two parts. The analytic integration of the second term becomes then possible.

2.3.2.2 Reduction of the Integration Domain

We can write:

$$L \int_0^{y_0} g dy = L \int_0^{y_t} g dy + L \int_{y_t}^{y_0} g dy = G + G_t \quad (2.20)$$

The integration boundary of transition y_t is defined by:

$$f_{ij} = 0 \quad \text{for } i \neq j \quad f_{ij} = 1 \quad \text{for } i = j \quad (2.20a)$$

In figure 2.4 the terms f_{ij} are represented as a function of y , for gaussian and lorentzian autocorrelation functions (table 2.1). We observe that the intercorrelation functions $\{f_{12}; f_{34}; f_{13}; f_{14}\}$ become null when $y \geq y_{tG} = 3$ in the gaussian case, $y \geq y_{tL} = 6$ for the lorentzian case, whereas the correlations terms $\{f_{11}; f_{33}\}$ become independent of y and are equal to unity. The limits $\{y_{tG}, y_{tL}\}$ are obtained when equations (2.20a) are verified involving that $\{y_{tG} = 3, y_{tL} = 6\}$. Wagner and Smith assumed that equations (2.20a) are verified for any values of y , involving that equation (2.20) is reduced to G_t with $y_t = 0$. This condition is plotted in solid line in figure 2.4. Making variable transformations given by equations (2.18a), the Wagner and Smith conditional probabilities are (equations (2.16a)) (without correlation):

$$g_W(h) = \frac{\Lambda v}{L\sqrt{\pi}} \cdot e^{-h^2} \quad g_S(h) = \frac{g_W(h)}{1 - \frac{\text{erfc}(h)}{2}} \quad (2.21)$$

with

$$\begin{cases} \Lambda = \left[e^{-v^2} - v\sqrt{\pi}\text{erfc}(v) \right] / (2v\sqrt{\pi}) \\ h = h_0 + y \frac{\mu L}{\omega\sqrt{2}} = h_0 + y \times v\eta \quad \eta = \frac{\sigma L}{\omega} \end{cases} \quad (2.21a)$$

Substituting equations (2.21) into the second integral (2.20), the analytic integration of g on the range $[y_t; y_0]$ is:

$$\left\{ \begin{array}{l} G_{tW}(h_0, v) = \int_{y_t}^{y_0} g_W(h_0, v) dy = \frac{\Lambda}{2} [\text{erf}(h_f) - \text{erf}(h_t)] \\ G_{tS}(h_0, v) = \int_{y_t}^{y_0} g_S(h_0, v) dy = -\ln \left[\frac{1 - \frac{\text{erfc}(h_t)}{2}}{1 - \frac{\text{erfc}(h_f)}{2}} \right]^\Lambda \end{array} \right. \quad (2.21b)$$

$$\left\{ \begin{array}{l} h_t = h_0 + y_t v \eta \\ h_f = h_0 + y_0 v \eta \end{array} \right.$$

In table 2.1, we notice that $\eta = \sqrt{2}$, but this equation is not always checked (damped autocorrelation functions). Substituting equation (2.20) into (2.19), the shadowing function is given by:

$$S(v) = \frac{1}{\pi} \int_{-\infty}^{\infty} I(h_0) \left[\int_0^{\infty} J(h_0, p_0) dp_0 \right] dh_0$$

$$\left\{ \begin{array}{l} I(h_0) = \exp[-h_0^2 - G_t(h_0, v)] \\ J(h_0, p_0) = \exp \left[-(v - p_0)^2 - L \int_0^{y_t} g(y, h_0, p_0, v) dy \right] \end{array} \right. \quad (2.22)$$

2.3.2.3 Note

The Wagner and Smith models assume that the surface is infinite $y_0 = \infty$ involving that $h_f = \infty$ and $y_t = 0 \Rightarrow h_t = h_0$, thus:

$$\left\{ \begin{array}{l} S_W(v) = \frac{1}{\pi} \int_{-\infty}^{\infty} e^{-h_0^2 - \Lambda \text{erfc}(h_0)} dh_0 \int_0^{\infty} e^{-(v-p_0)^2} dp_0 = \Lambda' \times \frac{1 - e^{-\Lambda}}{\Lambda} \\ S_S(v) = \frac{1}{\pi} \int_{-\infty}^{\infty} e^{-h_0^2} \cdot \left[1 - \frac{\text{erfc}(h_0)}{2} \right]^\Lambda dh_0 \int_0^{\infty} e^{-(v-p_0)^2} dp_0 = \Lambda' \times \frac{1}{\Lambda + 1} \end{array} \right. \quad (2.22a)$$

We have the same solution as in (2.11).

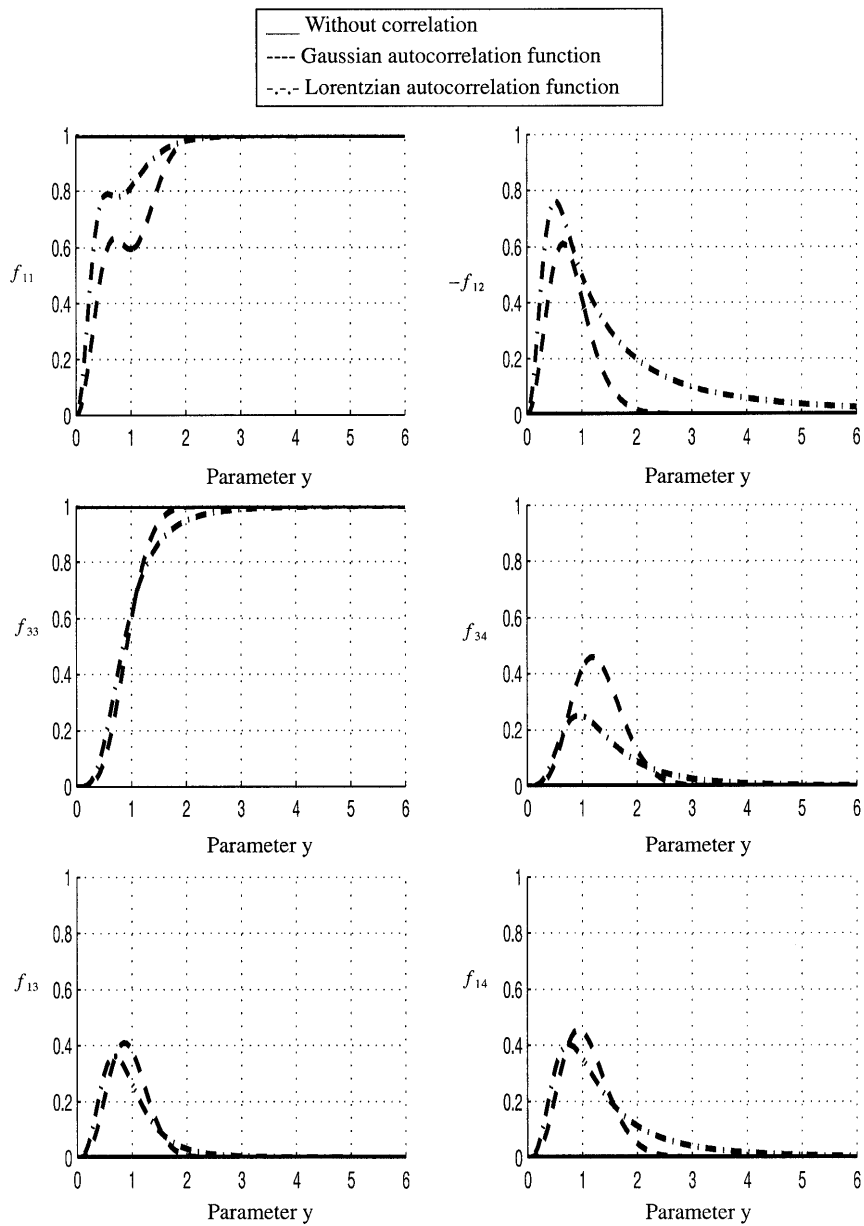


Figure 2.4 Gaussian and lorentzian autocorrelation functions.

2.3.2.4 Conclusion

In table 2.2 is summarized the calculus of Wagner and Smith average one-dimensional monostatic shadowing functions for a gaussian process and for any autocorrelation function. Their determination requires three linked integrations. First is performed the exact integration of the function g on the interval $[0; y_t]$. The second one is done over $J(h_0, p_0)$ according to the variable p_0 . The last obtained result is multiplied by $I(h_0)$, and integrated over h_0 . The terms f_{ij} given by equations (2.17a) contain the complete information about the autocorrelation function. The integration of the function g must respect the following convergence criteria:

$$f_M > 0 \quad f_{33} > 0 \tag{2.23}$$

The Wagner and Smith classical shadowing functions do not take into account the correlation, i.e., y_t is equal to zero. The $J(h, p)$ integration over p then becomes independent of h , both integrations over $\{p, h\}$ of $\{J(p), I(h)\}$ are independent and resolved analytically (equations (2.22a)). Finally for any autocorrelation function, the shadowing function depends on parameter $v = \mu/\sigma\sqrt{2}$ and on the observation length y_0 normalized to the correlation length. μ represents the slope of the incident beam and σ the slope standard deviation. With the aim of comparing the Smith and Wagner results, with or without correlation, and to estimate their hypothesis, the shadowing function is calculated numerically with any hypothesis. It is the reference solution, but the surface has to be generated.

2.3.3 Generation of the Random Surface

The numerical shadowing function requires to generate a random surface.

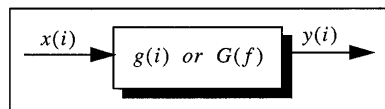


Figure 2.5 Issue configuration.

Table 2.2 Summary of the calculus of the average one-dimensional shadowing function for any autocorrelation function.

Shadowing function	$S(\nu) = \frac{1}{\pi} \int_{-\infty}^{\infty} I(h_0) \left[\int_0^{\infty} J(h_0, p_0) dp_0 \right] dh_0$ $I(h_0) = \exp[-h_0^2 - G_t(h_0, \nu)] \quad J(h_0, p_0) = \exp\left[-(\nu - p_0)^2 - L \int_0^{y_t} g(y, h_0, p_0, \nu) dy\right]$
Intergration	$h_0 \in [-3; 3] \quad p_0 \in [0; 3 + \nu] \quad h = h_0 + y \times \nu \eta$
Wagner g_{WL} funcion	$\frac{\eta \sqrt{f_M}}{2\pi f_{33}} \cdot e^{-D - \nu(\nu A + 2B)} \cdot \left[1 - e^{S^2} \sqrt{\pi} \text{Serfc}(S) \right] \quad \text{with} \quad \begin{cases} S = \frac{B + \nu A}{\sqrt{A}} \\ \eta = \frac{\sigma L}{\omega} = cste \end{cases}$ <p>and</p> $\begin{cases} D = \frac{(h_0^2 + h^2) f_{11} + 2h_0 h f_{12} + 2(\nu - p_0)(h_0 f_{13} - h f_{14}) + (\nu - p_0)^2 f_{33}}{f_M} - h_0^2 - (\nu - p_0)^2 \\ S = \frac{h_0 f_{14} - h f_{13} + (\nu - p_0) f_{34} + \nu f_{33}}{\sqrt{f_{33} f_M}} \\ \mu(\mu A + 2B) = \frac{\nu^2 f_{33} + 2\nu(h_0 f_{14} - h f_{13}) + 2\nu f_{34}(\nu - p_0)}{f_M} \end{cases}$
Wagner G_t function	$\frac{\Lambda}{2} [\text{erf}(h_0 + y_0 \nu \eta) - \text{erf}(h_0 + y_t \nu \eta)]$
Smith g_{SL} funcion	$\frac{\eta}{\pi} \frac{\sqrt{f_{11} f_{33} - f_{13}^2}}{f_{33}} \cdot \frac{e^{-D - \nu(\nu A + 2B) - h_0^2 - (\nu - p_0)^2} \cdot \left[1 - e^{S^2} \sqrt{\pi} \text{Serfc}(S) \right]}{e^{\frac{B_1^2}{A_1}} - C_1 \cdot \text{erfc}\left(-\frac{A_1 h + B_1}{\sqrt{A_1}}\right)}$ $\begin{cases} C_1 = h_0^2 \cdot \frac{f_{11} f_{33} - f_{14}^2}{f_{33} f_M} + (\nu - p_0)^2 \cdot \frac{f_{33}^2 - f_{34}^2}{f_{33} f_M} + 2h_0(\nu - p_0) \cdot \frac{f_{13} f_{33} - f_{14} f_{34}}{f_{33} f_M} \\ \frac{B_1}{\sqrt{A_1}} = \frac{h_0(f_{12} f_{33} + f_{14} f_{13}) + (\nu - p_0)(f_{13} f_{34} - f_{14} f_{33})}{\sqrt{f_{33} f_M (f_{11} f_{33} - f_{13}^2)}} \quad \sqrt{A_1} = \sqrt{\frac{f_{11} f_{33} - f_{13}^2}{f_{33} f_M}} \end{cases}$
Smith G_t funcion	$-\ln \left[\frac{1 - \text{erfc}(h_0 + y_t \nu \eta)/2}{1 - \text{erfc}(h_0 + y_0 \nu \eta)/2} \right]^\Lambda$

2.3.3.1 The Problem Configuration

Let $x(i)$ be the known sampled input signal, $y(i)$ the output signal (figure 2.5) to determine and $\{g(i), G(f)\}$ the spatial and frequential impulse response of the filter. The goal of this paragraph is to calculate the filter coefficients knowing the autocorrelation functions $\{R_x(i), R_y(i)\}$ of samples $\{x(i), y(i)\}$ respectively. The Fourier trans-

form method [28, 29] is used. If $x(i)$ is a stationary random process of second order with a power spectral density $\Phi_x(f)$ then $y(i)$ is a stationary random second order process, whose power spectral density $\Phi_y(f)$ checks:

$$m_y = G(0) \cdot m_x \quad \Phi_y(f) = |G(f)|^2 \cdot \Phi_x(f) \quad (2.24)$$

where m_x and m_y are respectively the means of input and output samples of the filter. If the impulse response is real, we have:

$$G(f) = \sqrt{\frac{\Phi_y(f)}{\Phi_x(f)}} \quad (2.24a)$$

Furthermore:

$$y(i) = g(i) * x(i) \quad (2.25)$$

where $*$ is the convolution product. Substituting equation (2.24a) into (2.25). $y(i)$ leads to:

$$y(i) = TF^{-1} \left[\sqrt{\Phi_y(f)/\Phi_x(f)} \right] * x(i) \quad (2.25a)$$

Applying to the input of the filter a gaussian white noise, then its power spectral density is defined by:

$$\Phi_x(f) = \omega_b^2 \quad (2.26)$$

where ω_b^2 is noise variance. The signal $y(i)$ is:

$$y(i) = \frac{1}{\omega_b} \cdot w(i) * x(i) \quad \text{with} \quad w(i) = TF^{-1} \left[\sqrt{\Phi_y(f)} \right] \quad (2.27)$$

The filter coefficients $\{w_G(i), w_L(i)\}$ are for gaussian and lorentzian autocorrelation functions (table 2.1), respectively:

$$w_G(i) = \omega_y \cdot \sqrt{\frac{2}{L\sqrt{\pi}}} \cdot \exp\left(-\frac{2i^2}{L^2}\right) \quad w_L(i) = \omega_y \cdot 2\sqrt{\frac{1}{L\pi}} \frac{1}{1 + (2i/L)^2} \quad (2.27a)$$

where L is the correlation length and ω_y^2 the sample variance.

2.3.3.2 Simulations in the Lorentzian and Gaussian Cases

In figure 2.6 are represented the input and output characteristics of the filter for a gaussian and lorentzian unitary variance ω_y^2 autocorrelation functions. For this instance, the correlation length L is equal to 200, the input of the filter is a white noise with $100000 = 500L$ samples, its variance is unitary and its mean m_b is equal to zero. In the top left of figure, the output sample normalized histogram is compared with its theoretical distribution. Both curves show a gaussian behavior. We also notice that the mean is null (centered to zero) and whole energy is concentrated between $-3\omega_b$ and $3\omega_b$. In top center and top right of figures, are plotted the output samples normalized histograms and their theoretical distribution for each autocorrelation function. We observe a gaussian behavior (because the filter is linear) with a null mean value m_y , checking the equation (2.24) with $m_x = m_b = 0$.

In center figures are represented respectively the behavior of input $x(i)$ and output surfaces $\{y_G(i), y_L(i)\}$. The input is very noisy whereas the output becomes smoother due to the correlation. Finally, in bottom figures the input and output samples normalized autocorrelation functions are plotted. At the input, we observe a centered peak at zero, which theoretically is Dirac function $\delta(i)$, whereas at the output we obtain the expected autocorrelation functions. Indeed, the difference between theoretical curve and the curve obtained from filter coefficients is weak.

2.3.3.3 The Numerical Shadowing Function: Reference Solution

In order to estimate the hypothesis introduced by Wagner and Smith, the one-dimensional shadowing function is determined numerically from the algorithm [8, 24] summarized in figure 2.7. The procedure of calculus is checked by substituting a sinusoidal surface of equation $z(y) = A \sin(By)$ to the random surface. Indeed the point y_1 where the surface is in the shadow verifies:

$$\left. \frac{dz}{dy} \right|_{y=y_1} = A \cdot B \cdot \cos(By_1) = -\cot \theta \Rightarrow y_1 = \text{acos} \left(\frac{-\cot \theta}{AB} \right) / B \quad (2.28)$$

The point y_2 where the surface emerges of the shadow checks the following equation:

$$z(y_1) - z(y_2) + (y_1 - y_2) \cot \theta = 0 \quad (2.28a)$$

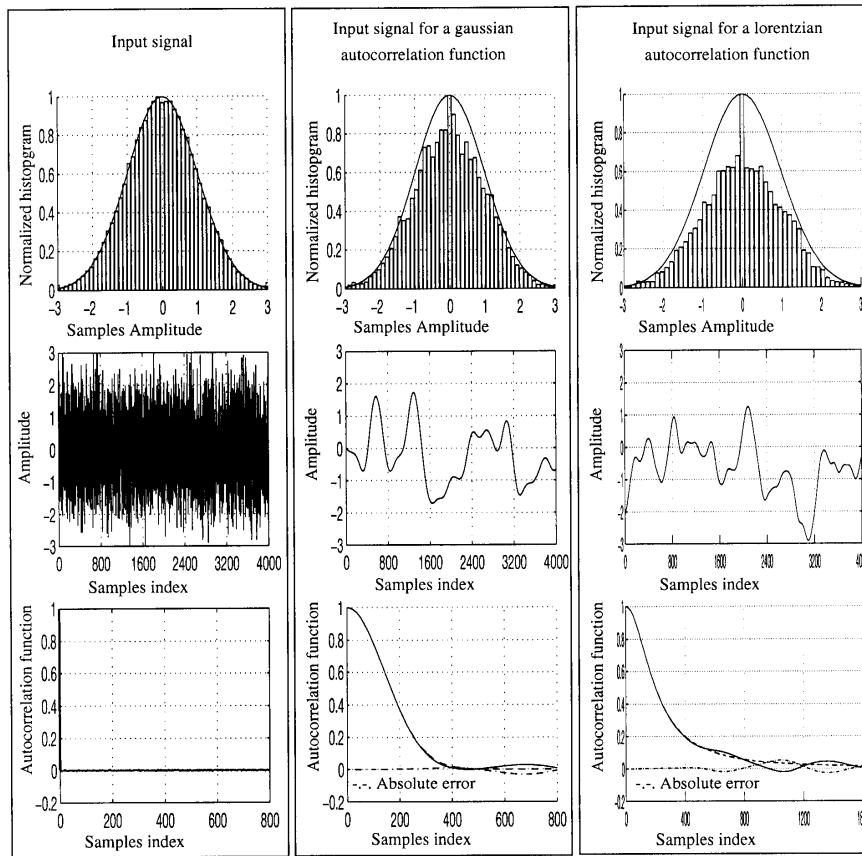
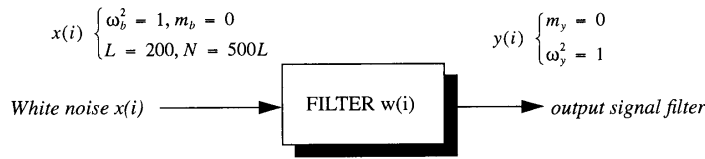


Figure 2.6 Random surfaces for different autocorrelation functions.

This equation is resolved by dichotomy. Then the shadowing function over one period is equal to:

$$S_N(\theta) = 1 - \frac{B[y_2(\theta) - y_1(\theta)]}{2\pi} \tag{2.28b}$$

In figure 2.8 are compared the shadowing functions obtained from both methods with $\{A = 0, 5; B = 5\}$. The number of samples is 5000. The

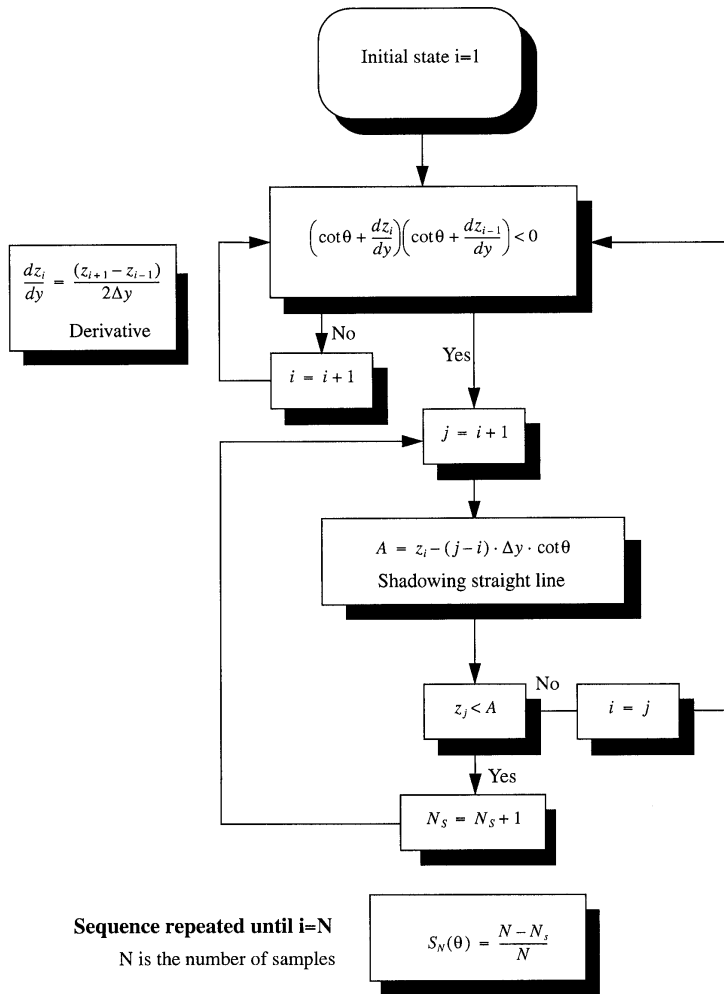


Figure 2.7 Algorithm of the shadowing function.

similarity of both curves validates the algorithm.

2.3.4 Simulations on an Infinity Surface

In this section, the Smith and Wagner shadowing functions (table 2.2) with and without correlation (equations (2.22a)) are simulated for an infinite surface ($y_0 = \infty$). With the aim to quantify the hypothesis of Wagner and Smith classical approaches (without correlation),

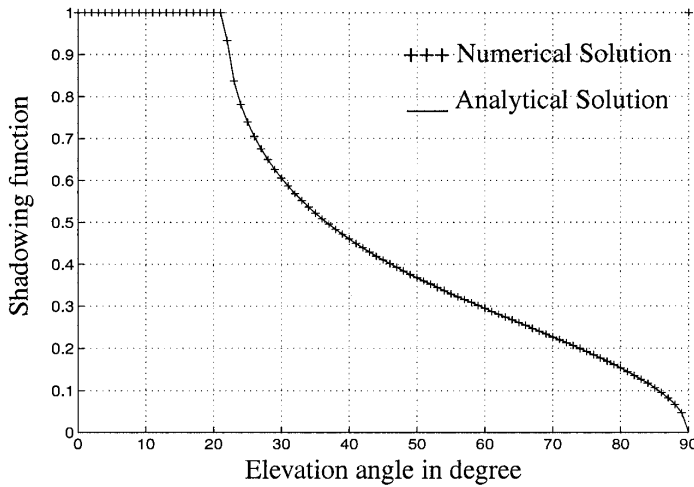


Figure 2.8 Comparison of the two methods of the determination of the shadowing function for a sinusoidal surface.

they are compared to the reference solution. This shadow is obtained from generating surfaces (paragraph 2.3.3.3) for lorentzian and gaussian autocorrelation functions. Finally, damped behaviors of gaussian and lorentzian envelopes are simulated.

2.3.4.1 The Gaussian Autocorrelation Function

In figure 2.9 are represented the shadowing functions for a gaussian surface. The reference solution is in solid line. The Wagner and Smith results are plotted in dashed line without taking into account the correlation, whereas in circles and crosses the correlation is included. We observe that the correlation involves a decreasing of the shadowing function. In figure 2.10 the absolute errors between shadowing functions and the reference solution are plotted. For $v \geq 1,4$, the correlation is negligible when the incidence angle is inferior to $\theta_c = \text{atan}(0.505/\sigma)$, with σ the slope standard deviation. For $v < 1,4$, the correlation divides the absolute error by about three. Finally, the Smith results are better than the Wagner ones.

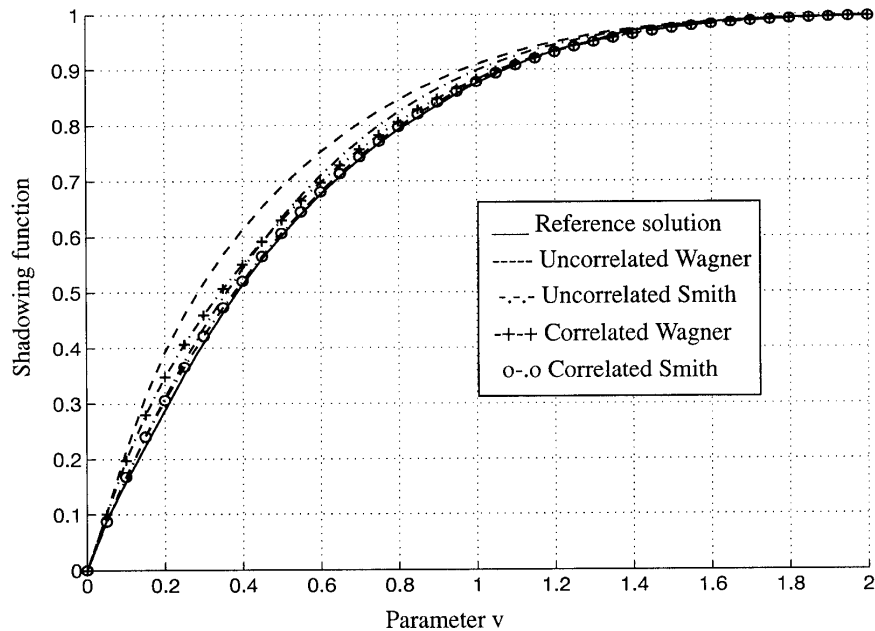


Figure 2.9 One-dimensional monostatic shadowing functions as a function of v for a gaussian surface.

2.3.4.2 The Lorentzian Autocorrelation Function

In figure 2.11 are represented the same curves as in figure 2.9, but for a lorentzian surface. We also notice that the results including the correlation are very close to the reference solution. In figure 2.12 the absolute error between the shadowing functions and the reference solution are compared. We observe that the Smith results are better than the Wagner ones. Like for the case of a gaussian autocorrelation function, the correlation is negligible for $v \geq 1,4$, and divides the absolute error by about three.

Since in table 2.2, the slope variance σ^2 is the same for a lorentzian and gaussian autocorrelation function, the Wagner and Smith classical shadowing functions are equal in each case due to the fact that $v = \cot \theta / (\sigma \sqrt{2})$. On the contrary, correlated shadowing functions are different (figure 2.13 and figure 2.14), because the terms f_{ij} are not identical for gaussian and lorentzian surfaces (figure 2.4).

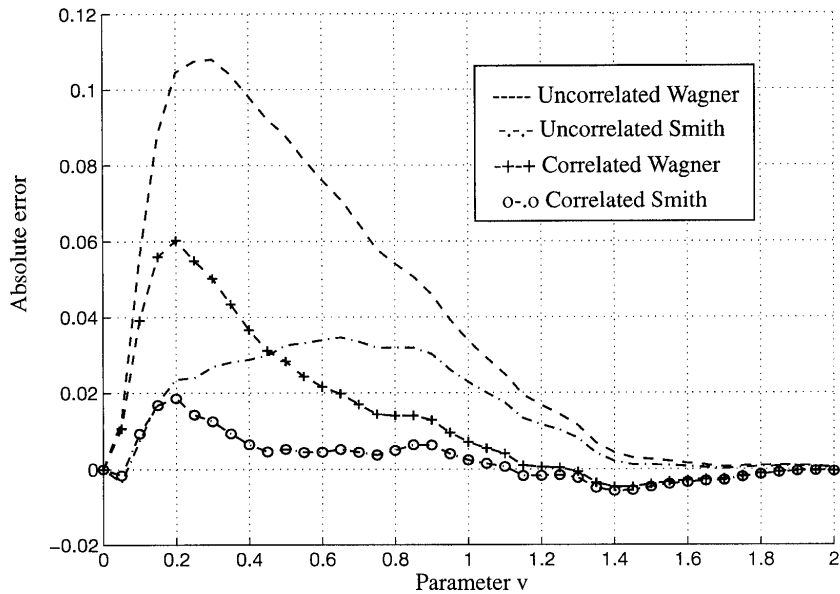


Figure 2.10 Absolute errors between shadowing functions and the reference solution as a function of v for a gaussian surface.

2.3.4.3 The Damped Autocorrelation Functions

In the first chapter, we have shown that the isotropic part of the autocorrelation function is damped lorentzian (paragraph 1.5.1.3). In order to show this property, simulations are realized on the following surfaces:

$$\begin{cases} R_0(\tau) = \omega^2 \exp\left(-\frac{\tau^2}{L^2}\right) \cos\left(\frac{a\tau}{L}\right) & \text{Damped gaussian} \\ R_0(\tau) = \omega^2 \cos\left(\frac{a\tau}{L}\right) / \left(1 + \frac{\tau^2}{L^2}\right) & \text{Damped lorentzian} \end{cases} \quad (2.29)$$

For each autocorrelation function, table 2.3 gives the functions $\{f_0, f_1, f_2, \sigma, \eta\}$. Since the analytical determination of the filter coefficients is not possible, the reference solutions are not simulated. Moreover, we only keep the Smith model. In figure 2.15, the Smith shadowing functions with and without correlation are represented as a function of v , and for $a = \{1, 2\}$. We observe that the correlated results are slightly different according to the autocorrelation functions, whereas the more a increases the more the gap between the correlated and

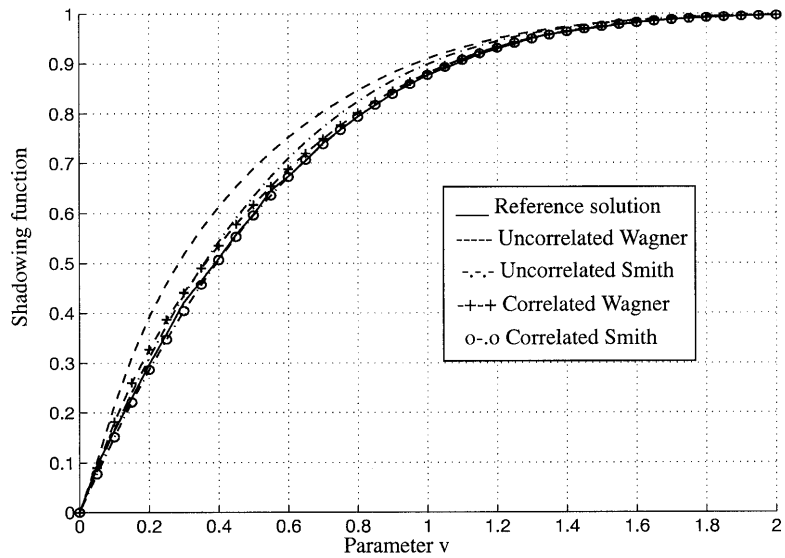


Figure 2.11 One-dimensional monostatic shadowing functions as a function of v for a lorentzian surface.

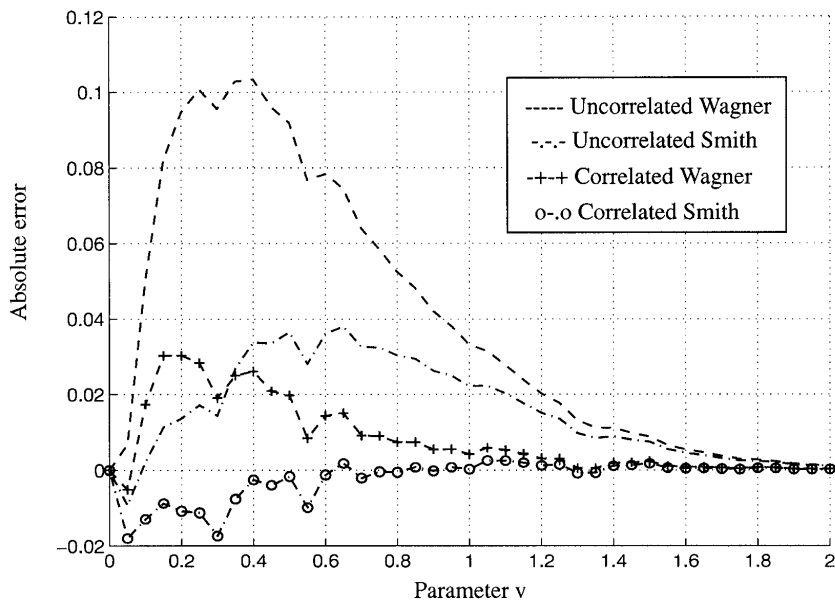


Figure 2.12 Absolute errors between shadowing functions and the reference solution as a function of v for a lorentzian surface.

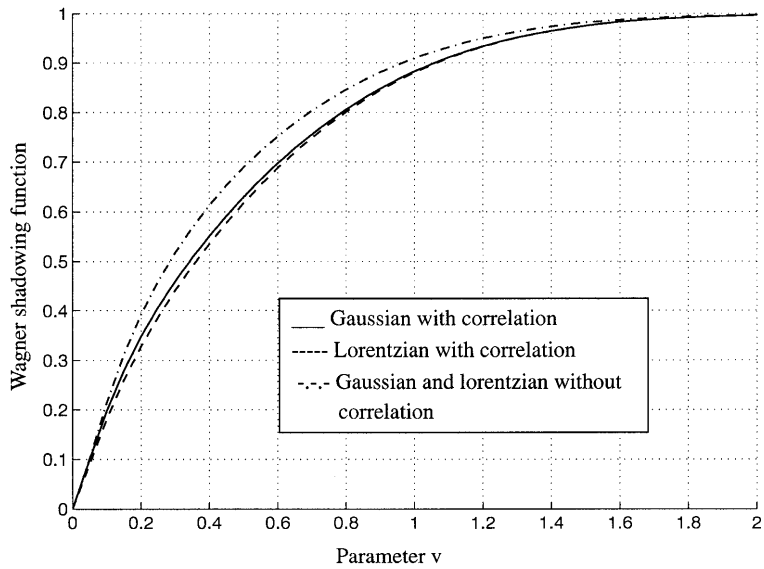


Figure 2.13 Monostatic one-dimensional shadowing function of Wagner according to v .

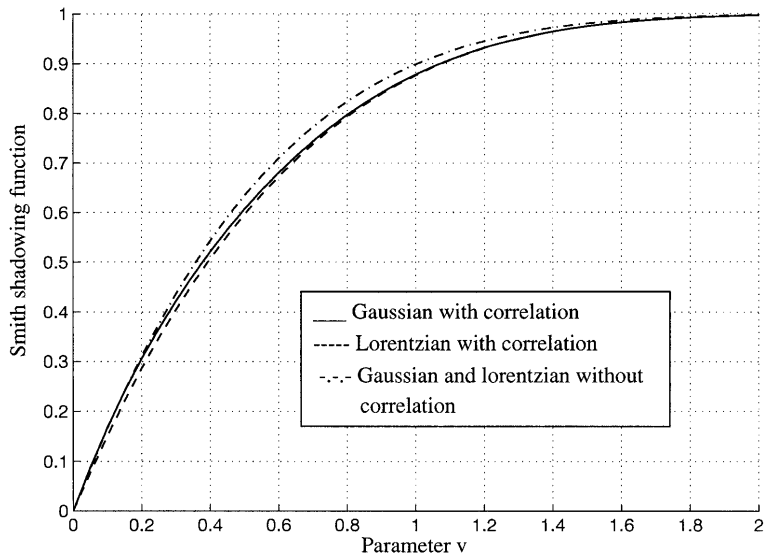


Figure 2.14 Monostatic one-dimensional shadowing function of Smith according to v .

Table 2.3 Damped autocorrelation functions.

	Damped gaussian	Damped lorentzian
f_0	$e^{-y^2} \cos(ay)$	$\cos(ay)/(1+y^2)$
f_1	$\frac{e^{-y^2} [2y \cos(ay) + a \sin(ay)]}{\sqrt{2+a^2}}$	$\frac{1}{\sqrt{2+a^2}} \left[\frac{2y \cos(ay)}{(1+y^2)^2} + \frac{a \sin(ay)}{1+y^2} \right]$
f_2	$\frac{e^{-y^2} [(2+a^2-4y^2) \cos(ay) - 4ay \sin(ay)]}{2+a^2}$	$\frac{1}{2+a^2} \left\{ \cos(ay) \left[\frac{a^2}{1+y^2} + \frac{2(1-3y^2)}{(1+y^2)^3} \right] - \frac{4ay \sin(ay)}{(1+y^2)^2} \right\}$
$\{\sigma, \eta\}$	$\sigma = \frac{\omega\sqrt{2}}{L} \sqrt{1 + \frac{a^2}{2}} \quad \eta = \sqrt{2+a^2}$	$\sigma = \frac{\omega\sqrt{2}}{L} \sqrt{1 + \frac{a^2}{2}} \quad \eta = \sqrt{2+a^2}$

uncorrelated shadowing functions increases. We also notice that the correlation becomes negligible when $v \geq 1,4$. In figure 2.16, The Smith correlated shadowing function of damped lorentzian surface are compared with the parameter $a = \{0, 1, 2\}$. We observe that the results vary slightly with a .

2.3.5 Conclusion

The Wagner and Smith classical approaches neglect the correlation, and overestimate the shadowing function. It physically means it is independent of the autocorrelation function.

The simulations realized on lorentzian and gaussian infinite surfaces show the correlated results are better than uncorrelated ones, and the correlation can be negligible for incidence angles inferior to $\theta_c = \text{atan}(0.505/\sigma)$. Moreover, the advantage to include the correlation is to take into account the surfaces which have the same slope variance (tables 2.2 and 2.3). The results obtained from the Smith correlated shadowing effect for the lorentzian and gaussian autocorrelation functions are similar and vary slightly with a . On the contrary, when a increases, the gap between correlated and uncorrelated results increases, but becomes null when the incidence angle is inferior to θ_C . Finally, in the rest of this chapter, we only keep the Smith model since its results are better than Wagner's ones.

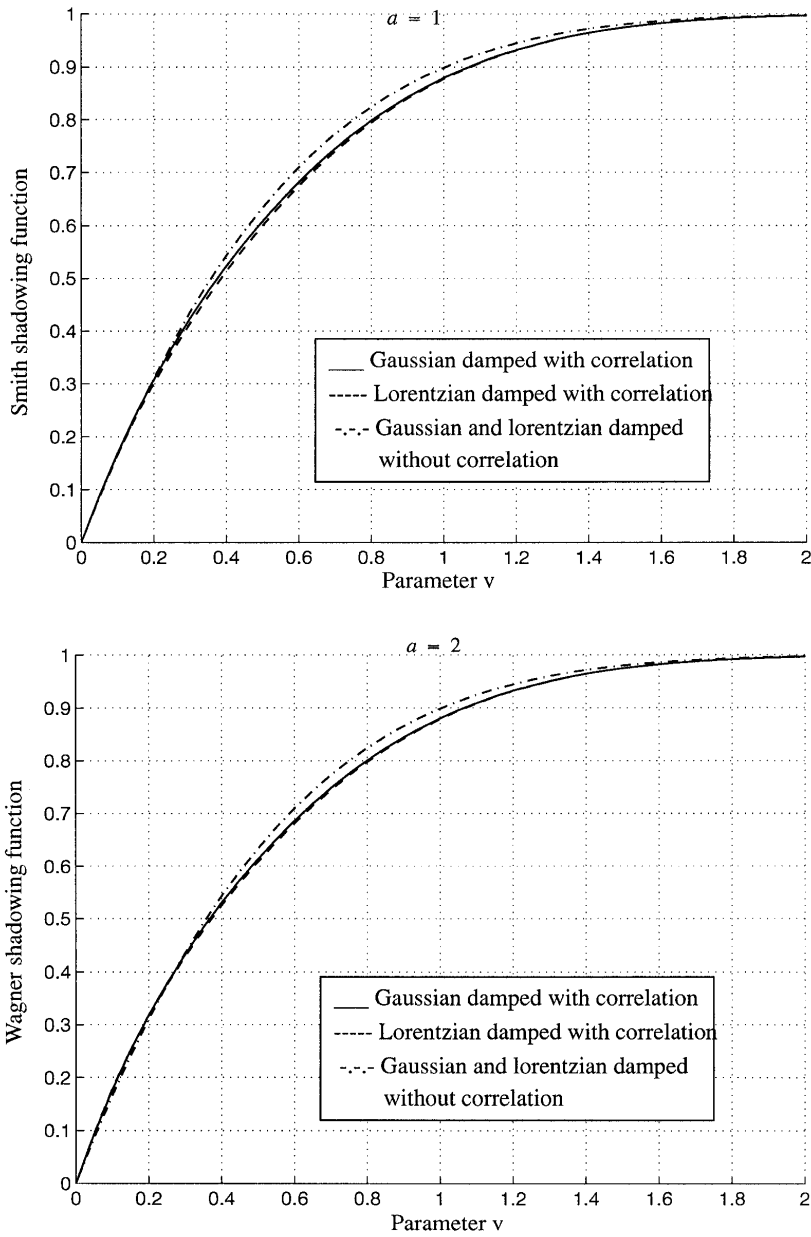


Figure 2.15 The Smith one-dimensional monostatic shadowing function of damped autocorrelation function for $a = \{1, 2\}$ as a function of v .

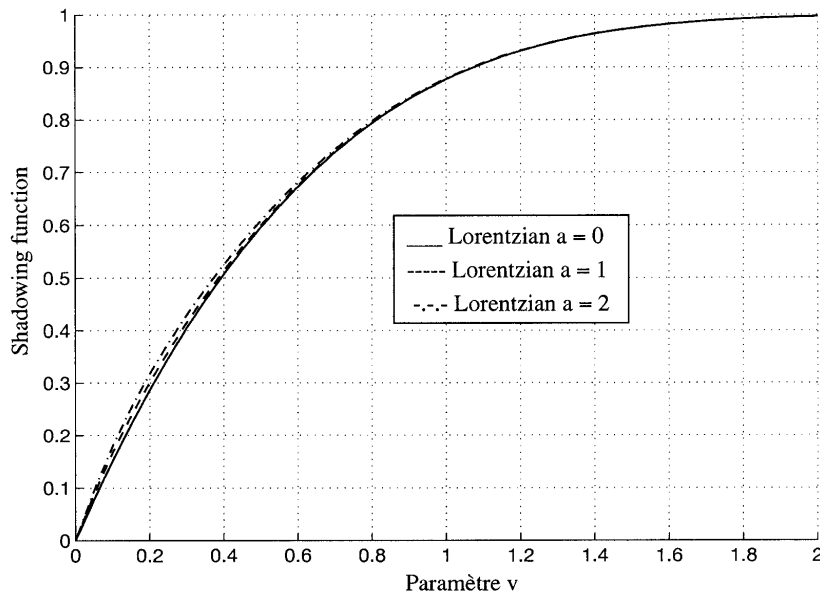


Figure 2.16 The Smith correlated one-dimensional monostatic shadowing function of damped lorentzian autocorrelation function for $a = \{0, 1, 2\}$ as a function of v .

2.4 THE ONE-DIMENSIONAL BISTATIC SHADOWING FUNCTION

The formalism exposed in previous paragraphs, is extended to the bistatic case for a **gaussian** process. So, the bistatic problem is equivalent to two independent monostatic configurations, defined by the transmitter and by the receiver. The Smith monostatic solutions with or without correlation are extended to bistatic case, then compared with the reference solution obtained by generating the surface.

2.4.1 Determination of the Bistatic Shadowing Function

2.4.1.1 Problem Description

For a stationary process, the bistatic shadowing function represents the probability $S(\theta_1, \theta_2|F)$ that the incident ($y < 0$) and reflected ($y > 0$) rays for respective observation angles $\{\theta_1, \theta_2\}$ are not crossed by the surface, knowing that they cross each other at the point F located on the surface with height ξ_0 and slope γ_0 (figure 2.17).

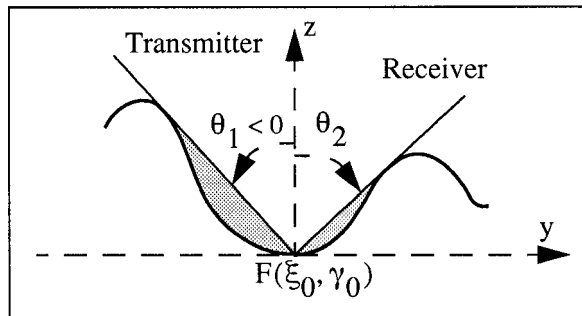


Figure 2.17 Bistatic configuration of the shadowing function.

Let $S(\theta_1|\theta_2, F)$ be the probability that the incident ray does not intercept the surface, knowing that the reflected ray does not cross the surface, and that the two rays cut each other at the point F . $S(\theta_2|\theta_1, F)$ is defined by analogy with $S(\theta_1|\theta_2, F)$. Applying the Bayes theorem, we have:

$$S(\theta_1, \theta_2, |F) = S(\theta_1|\theta_2, F) \cdot S(\theta_2|F) = S(\theta_2|\theta_1, F) \cdot S(\theta_1|F) \quad (2.30)$$

where $\{S(\theta_1|F), S(\theta_2|F)\}$ are the conditional probabilities. According to the value of θ_2 , we have to distinguish three cases [19] (figure 2.18). We set θ_1 to negative values.

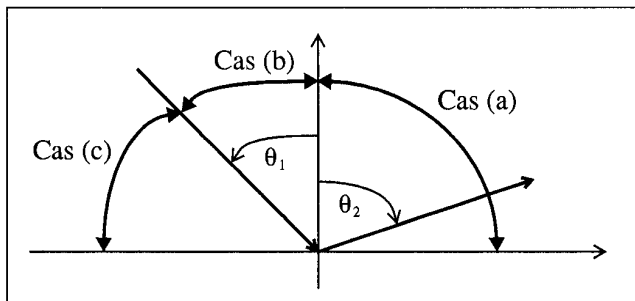


Figure 2.18 Geometric representation of the three cases.

2.4.1.2 Study of the Three Cases

Case (a) $\theta_2 \in [0; \pi/2]$

Assuming that the probability to cut the incident ray is independent of the probability to cut the reflected ray, we have:

$$S(\theta_1, \theta_2, |F) = S(\theta_1|F) \cdot S(\theta_2|F) \quad (2.30a)$$

Case (b) $\theta_2 \in [\theta_1; 0]$

Using equation (2.30), the conditional probability is:

$$S(\theta_1, \theta_2, |F) = S(\theta_2|\theta_1, F) \cdot S(\theta_1|F) = 1 \cdot S(\theta_1|F) \quad (2.30b)$$

Case (c) $\theta_2 \in [-\pi/2; \theta_1]$

Using equation (2.30), the conditional probability is:

$$S(\theta_1, \theta_2, |F) = S(\theta_1|\theta_2, F) \cdot S(\theta_2|F) = 1 \cdot S(\theta_2|F) \quad (2.30c)$$

2.4.1.3 Conclusion

The bistatic conditional probability is for angles $\{\theta_1; \theta_2\}$:

$$S(\theta_1, \theta_2, |F) = \begin{cases} S(\theta_1|F) \cdot S(\theta_2|F) & \text{for } \theta_2 \in \left[0; \frac{\pi}{2}\right] \\ S(\theta_1|F) & \text{for } \theta_2 \in [\theta_1; 0] \\ S(\theta_2|F) & \text{for } \theta_2 \in \left[-\frac{\pi}{2}; \theta_1\right] \end{cases} \quad (2.31)$$

The bistatic shadowing function is obtained from two monostatic shadowing functions defined by the angular positions of the transmitter and the receiver. The average shadowing function over the slopes is:

$$S(\theta_1, \theta_2) = \frac{1}{2\pi\sigma\omega} \int_{-\infty}^{\infty} \int_{-\infty}^{\infty} S(\theta_1, \theta_2, |F) \cdot \exp\left(-\frac{\xi_0^2}{2\omega^2} - \frac{\gamma_0^2}{2\sigma^2}\right) d\xi_0 d\gamma_0 \quad (2.32)$$

2.4.2 Application on the Smith Shadowing Function

2.4.2.1 The Reference Solution-Algorithm

In order to determine the bistatic shadowing function obtained by generating the surface with N samples, is built a table indexed to

the number of the sample. Table 2.4 gives two fields defining the transmitter and the receiver.

Table 2.4 Fields definition.

Index i	Transmitter E	Receiver R
$[1; N]$	$E_i = 1$ illuminated $E_i = 0$ hidden	$R_i = 1$ illuminated $R_i = 0$ hidden

Sample i is said to be “hidden” if it is invisible for the transmitter or the receiver. So, the numerical shadowing function is:

$$S_N(\theta_1, \theta_2) = \frac{1}{N} \sum_{i=1}^N E_i \cdot R_i \quad \text{if } \theta_2 > 0 \text{ then } R_i = R_{N-i} \quad (2.33)$$

Note that if the receiver angle is positive, the surface is then flip in the left/right direction.

2.4.2.2 The Uncorrelated Shadowing Function

For an infinite surface the Smith bistatic uncorrelated shadowing function is (appendix 5):

$$S_S(v_1, v_2) = \begin{cases} \frac{1 - \frac{1}{2}[\text{erfc}(v_1) + \text{erfc}(v_2)]}{\Lambda_1 + \Lambda_2 + 1} & \text{for } 0 \leq v_2 < \infty \\ \frac{1 - \frac{1}{2}\text{erfc}(v_2)}{\Lambda_2 + 1} & \text{for } -v_1 \leq -v_2 < 0 \\ \frac{1 - \frac{1}{2}\text{erfc}(v_1)}{\Lambda_1 + 1} & \text{for } -\infty \leq -v_2 < -v_1 \end{cases} \quad (2.34)$$

with

$$\begin{cases} v_i = \frac{\cot(|\theta_i|)}{\sqrt{2}\sigma} \\ \Lambda_i = [e^{-v_i^2} - v_i\sqrt{\pi}\text{erfc}(v_i)] / (2v_i\sqrt{\pi}) \end{cases} \quad i = \{1, 2\} \quad (2.34a)$$

2.4.2.3 The Correlated Shadowing Function

For a surface with length L_0 , the shadowing function is (equation (2.1)):

$$S_S(\theta, \xi_0, \gamma_0) = \Upsilon(\mu - \gamma_0) \cdot \exp \left[- \int_0^{L_0} g(\tau) d\tau \right] \quad (2.35)$$

Case (a) $\theta_2 \in [0; \pi/2]$

Substituting equation (2.35) into (2.30a), the Smith shadowing function is given by:

$$\begin{aligned} S_S(\theta_1, \theta_2 | F) &= \Pi_{[\mu_1; \mu_2]} \cdot \exp \left[- \int_{-L_0}^0 g_{S1}(\tau) d\tau - \int_0^{L_0} g_{S2}(\tau) d\tau \right] \\ &= \Pi_{[\mu_1; \mu_2]} \cdot \exp \left[- \int_0^{L_0} [g_{S1}(-\tau) d\tau + g_{S2}(\tau)] d\tau \right] \end{aligned} \quad (2.36)$$

where $\{g_{S1}; g_{S2}\}$ are respectively the receiver and transmitter conditional probabilities. The definition of $\Pi_{[\mu_1; \mu_2]}$ is given in appendix 5. From generalizing the monostatic results contained in table 2.2, we show that the Smith averaged monostatic shadowing function is:

$$\begin{aligned} S_S(v_1, v_2) &= \frac{1}{\pi} \int_{-\infty}^{\infty} e^{-h_0^2} \left\{ \left[\frac{1 - \frac{\operatorname{erfc}(h_0 + y_t v_1 \eta)}{2}}{1 - \frac{\operatorname{erfc}(h_0 + y_0 v_1 \eta)}{2}} \right]^{\Lambda_1} \right. \\ &\quad \cdot \left. \left[\frac{1 - \frac{\operatorname{erfc}(h_0 + y_t v_2 \eta)}{2}}{1 - \frac{\operatorname{erfc}(h_0 + y_0 v_2 \eta)}{2}} \right]^{\Lambda_2} \left[\int_{-v_1}^{v_2} J(h_0, p_0) dp_0 \right] \right\} dh_0 \end{aligned} \quad (2.37)$$

with

$$J(h_0, p_0) = \exp \left\{ -p_0^2 - L \int_0^{y_t} [g_{S1}(-y) + g_{S2}(y)] dy \right\}$$

The parameters $\{v_1 \geq 0, v_2 \geq 0, \Lambda_1, \Lambda_2\}$ are given by equations (2.34a).

Conditional probabilities

Using equation (2.4), the Smith receiver conditional probability ($y > 0$) is:

$$g_{S2}(y) = \frac{\int_{-\infty}^{\infty} (\gamma - \mu_2) \cdot \exp[-A \cdot \gamma^2 - 2B \cdot \gamma - D] d\gamma}{\int_{-\infty}^{\infty} \int_{-\infty}^{\xi_0 + \mu_2 y L_0} \exp[-A \cdot \gamma^2 - 2B \cdot \gamma - D] d\xi d\gamma} \quad (2.38)$$

Its expression is given in table 2.2 by substituting $\{v - p_0 \rightarrow p_0; v \rightarrow v_2\}$. Applying the same principle for the emitter, the conditional probability ($y < 0$) becomes:

$$g_{S1}(-y) = \frac{\int_{-\infty}^{-|\mu_1|} (-\gamma - |\mu_1|) \cdot \exp[-A \cdot \gamma^2 - 2B \cdot \gamma - D] d\gamma}{\int_{-\infty}^{\infty} \int_{-\infty}^{\xi_0 + |\mu_1| y L_0} \exp[-A \cdot \gamma^2 - 2B \cdot \gamma - D] d\xi d\gamma} \quad (2.38a)$$

Setting $\gamma' = -\gamma$ in the numerator integral, we have:

$$g_{S2}(-y) = \frac{\int_{-\infty}^{\infty} (\gamma' - |\mu_1|) \cdot \exp[-A \cdot \gamma'^2 + 2B \cdot \gamma' - D] d\gamma'}{\int_{-\infty}^{\infty} \int_{-\infty}^{\xi_0 + |\mu_1| y} \exp[-A \cdot \gamma^2 - 2B \cdot \gamma - D] d\xi d\gamma} \quad (2.38b)$$

$g_{S2}(y)$ become $g_{S1}(-y)$ to permute B to $-B$ at the numerator and to permute μ_2 to $|\mu_1|$ at the numerator and at the denominator.

Synthesis

- When $0 \leq v_2 < \infty$, the shadowing function is given by equation (2.37). $g_{S2}(y)$ is calculated from the monostatic expression of g_S listed in table 2.2, by replacing $\{v \rightarrow v_2; v_2 - p_0 \rightarrow p_0\}$. $g_{S1}(-y)$ is determined by substituting $\{v \rightarrow v_1; v_1 - p_0 \rightarrow p_0; f_{ij}(y) \rightarrow$

$f_{ij}(-y)$. Moreover, B is changed by its opposite $-B$, which is equivalent to replace in the expressions of $\{S; \mu(\mu A + 2B)\}$, the $\{f_{13}; f_{14}; f_{34}\}$ by their opposite. In the case where the autocorrelation is even, we show that the functions $\{f_{12}; f_{11}; f_{33}; f_{34}\}$ are even, whereas $\{f_{13}; f_{14}\}$ are odd. It is then equivalent to replace in $\{S; \mu(\mu A + 2B)\}$, f_{34} by $-f_{34}$ and in C , $\{f_{13}; f_{14}\}$ by $\{-f_{13}; -f_{14}\}$.

- When $-v_1 \leq -v_2 < 0$ the shadowing function is obtained from the monostatic expression of g_S given in table 2.2, by changing $v \rightarrow v_2$.
- When $-\infty \leq -v_2 < -v_1$ the shadowing function is obtained from the monostatic expression of g_S given in table 2.2, by making $v \rightarrow v_1$.

2.4.2.4 Simulation on an Infinite Surface

In this part, the Smith bistatic one-dimensional shadowing function without correlation (equation (2.34)) and with correlation (equation (2.37)) are simulated, for an infinite surface ($y_0 = \infty$) of damped gaussian autocorrelation function (equation (2.29)).

In figure 2.19 is plotted the bistatic shadowing function obtained by generating a gaussian surface ($a = 0$). For a very rough surface (high standard deviation of slopes σ , i.e., $v_i = \mu_i / \sigma \sqrt{2}$ small), the shadowing function decreases quickly. For incidences near 90° , corresponding to $v_i \rightarrow 0$, the surface is highly shaded ($S \rightarrow 0$). On the contrary, for normal incidences (v_i near to two), all the surface is illuminated ($S = 1$). The variation between these two asymptotes values equal to 0 as much as σ .

In figure 2.20 the absolute errors between the reference solution and the correlated and correlated bistatic shadowing functions are compared. For $|v_i| \geq 1.4$, the effect of the correlation is negligible. We also see for $|v_i| < 1.2$ that the absolute error is divided by about three.

In figure 2.21, the absolute errors between the correlated and the uncorrelated results are represented for $a = \{1, 2\}$. We observe that the error varies weakly with a , and becomes null for $|v_i| \geq 1.4$. In figure 2.22 are plotted the differences between the shadowing functions obtained for $a = 0$ (gaussian case) and the ones determined for $a = \{1, 2\}$.

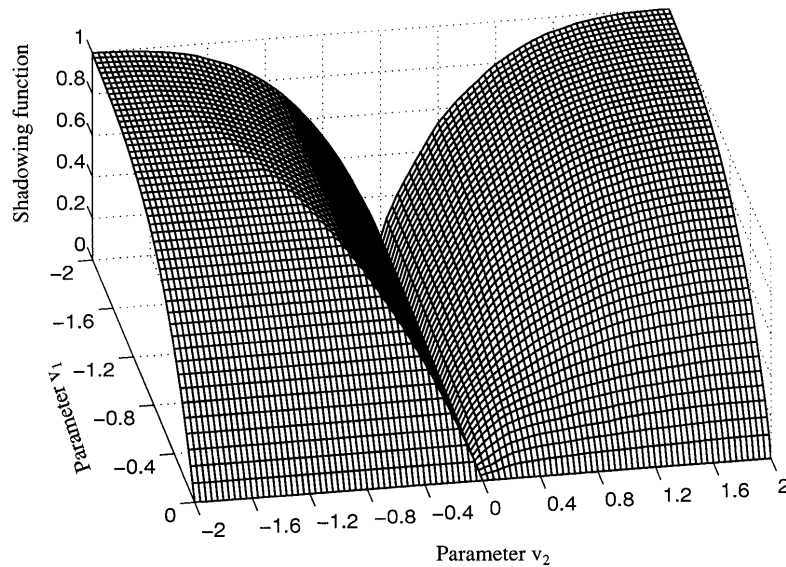


Figure 2.19 One-dimensional bistatic shadowing function obtained by generating a gaussian infinite surface with $a = 0$.

2.4.3 Conclusion

The formalism exposed in the previous paragraphs has been generalized to the one-dimensional bistatic case. The bistatic problem is equivalent to two independent monostatic configurations defined by the transmitter and by the receiver. The correlated and uncorrelated monostatic solutions of Smith have been extended and compared with the reference solution obtained by generating a surface. The simulations realized on an infinite surface for a gaussian autocorrelation function show that the Smith correlated results are close to the ones obtained with the reference solution. The absolute error between the Smith uncorrelated shadowing function and the reference solution is multiplied by about three when the parameters $|v_i|$ are inferior to 1.4, corresponding to incidence angles inferior to $|\theta_{ic}| = \text{atan}(0.505/\sigma)$.

2.5 THE TWO-DIMENSIONAL SHADOWING FUNCTION

We have shown that one-dimensional shadowing function depends on the autocorrelation function in the correlated case, or on the slope variance only when the correlation is not included. For an anisotropic

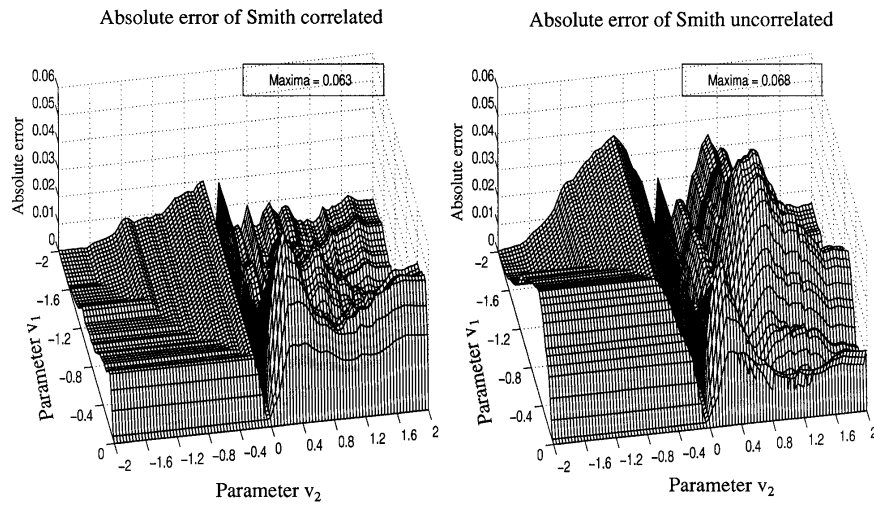


Figure 2.20 Absolute error between the uncorrelated and correlated bistatic shadowing functions of Smith and the numerical solution obtained from a gaussian surface ($a = 0$).

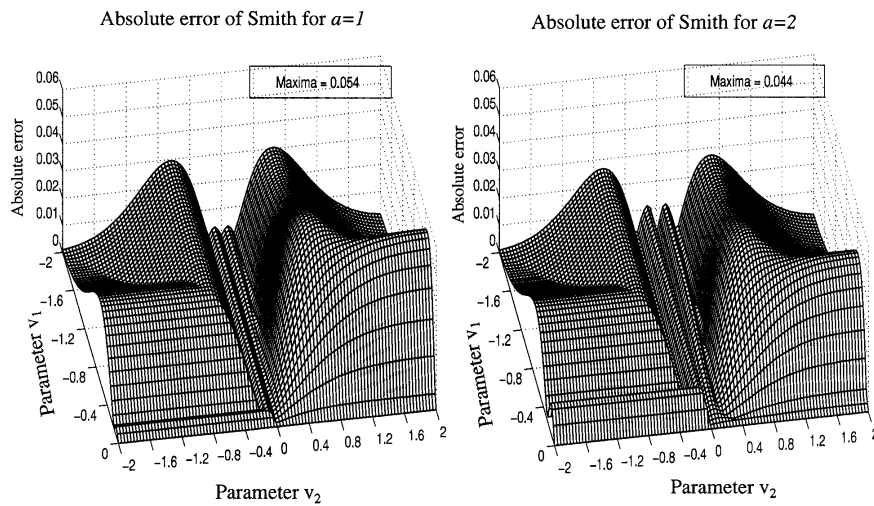


Figure 2.21 Absolute error between the correlated and uncorrelated one-dimensional bistatic shadowing functions of Smith for $a = \{1, 2\}$.

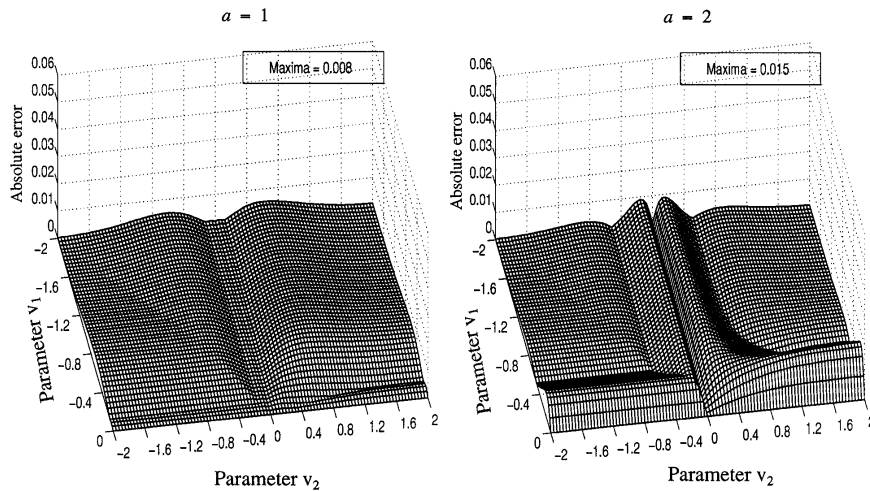


Figure 2.22 Difference between the Smith one-dimensional bistatic shadowing function obtained for $a = 0$ and the ones determined for $a = \{1, 2\}$.

surface these parameters depend on the observation direction ϕ according to the wind direction. This paragraph introduces this concept in the shadowing function.

2.5.1 Generalization of the Monostatic and Bistatic Cases without Correlation

The two-dimensional shadowing function is characterized in polar coordinates by the azimuth ϕ (observation direction according to the wind), and the incidence angle θ (figure 2.23). For a constant direction ϕ , the issue is one-dimensional. So, the idea is to extend the one-dimensional results to the two-dimensional case by executing a rotation with an angle ϕ around the (Oz) axis.

2.5.1.1 Expression of the Slope Probability Density

The slope probability density in cartesian coordinates (x, y, z) (see paragraph 1.5.2) is:

$$p(\gamma_x, \gamma_y) = \frac{1}{2\pi\sigma_x\sigma_y} \exp\left(-\frac{\gamma_x^2}{2\sigma_x^2} - \frac{\gamma_y^2}{2\sigma_y^2}\right) \quad \text{and} \quad \begin{cases} \sigma_x^2 = \alpha + \beta \\ \sigma_y^2 = \alpha - \beta \end{cases} \quad (2.39)$$

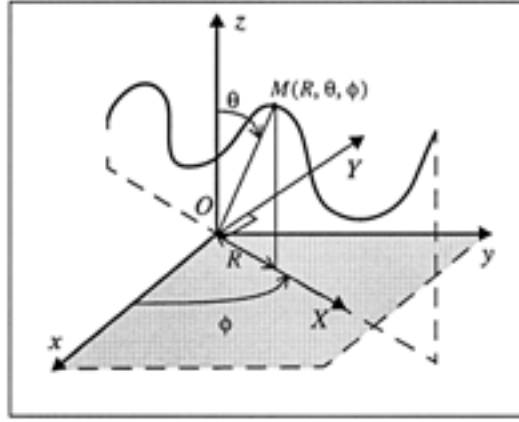


Figure 2.23 Two-dimensional configuration.

In order to determine the slope probability density $p(\gamma_X, \gamma_Y)$ in the direction ϕ , we make a base transformation (X, Y, z) . The former coordinates (γ_x, γ_y) are expressed the new ones (γ_X, γ_Y) as:

$$\begin{cases} \gamma_x = \gamma_X \cos \phi - \gamma_Y \sin \phi \\ \gamma_y = \gamma_X \sin \phi + \gamma_Y \cos \phi \end{cases} \quad (2.39a)$$

Substituting equations (2.39a) into (2.39), we have:

$$p(\gamma_X, \gamma_Y) = \frac{1}{2\pi\sqrt{\alpha^2 - \beta^2}} \exp(-a\gamma_Y^2 - 2b\gamma_Y - c) \cdot J \quad (2.40)$$

with

$$a = \frac{\alpha + \beta \sin(2\phi)}{2(\alpha^2 - \beta^2)} \quad b = \frac{\beta \sin(2\phi)}{2(\alpha^2 - \beta^2)} \gamma_X \quad c = \frac{\alpha - \beta \cos(2\phi)}{2(\alpha^2 - \beta^2)} \gamma_X^2 \quad (2.40a)$$

where J is the jacobian. The probability in the direction ϕ is obtained by calculating the marginal probability $p(\gamma_X)$ defined by:

$$p(\gamma_X) = \int_{-\infty}^{\infty} p(\gamma_X, \gamma_Y) d\gamma_Y \quad (2.40b)$$

Knowing that:

$$\int_{-\infty}^{\infty} \exp(-a\gamma_Y^2 - 2b\gamma_Y - c) d\gamma_Y = \sqrt{\frac{\pi}{a}} \exp\left(\frac{b^2}{a} - c\right) \quad (2.40c)$$

then ($J = 1$) :

$$p(\gamma_X) = \frac{1}{\sigma_X \sqrt{2\pi}} \exp\left(-\frac{\gamma_X^2}{2\sigma_X^2}\right) \quad \text{with} \quad \sigma_X^2 = \alpha + \beta \cos(2\phi) \quad (2.41)$$

The marginal probability in the direction ϕ is gaussian and its variance is σ_X^2 .

2.5.1.2 Simulations

For an infinite surface, the Smith monostatic one-dimensional shadowing function without correlation is for a gaussian process:

$$S_S(v) = \left[1 - \frac{\text{erfc}(v)}{2}\right] \frac{1}{\Lambda + 1} \quad \Lambda = \frac{[e^{-v^2} - v\sqrt{\pi}\text{erfc}(v)]}{2v\sqrt{\pi}} \quad v = \frac{\cot \theta}{\sqrt{2}\sigma} \quad (2.41a)$$

Therefore, the one-dimensional case becomes two-dimensional, changing σ by σ_X . For the bistatic case the reasoning is similar to the one used in (2.34) where $\{v_1, v_2\}$ are defined by:

$$v_1 = \frac{\cot(|\theta_1|)}{\sqrt{2[\alpha + \beta \cos(2\phi_1)]}} \quad v_2 = \frac{\cot(|\theta_2|)}{\sqrt{2[\alpha + \beta \cos(2\phi_2)]}} \quad (2.41b)$$

In the left part of figure 2.24, the slope standard deviation σ obtained from the Cox and Munk model (equation (1.51)) is plotted as a function of the friction speed u_f , and the direction ϕ . In the right part of figure is represented the **inferior** limit angle $\theta_c = \text{atan}(0.505/\sigma)$ where the correlation is negligible as a function of the direction ϕ , for different friction speeds. We see that the limit is contained between $[64; 76]^\circ$ with $u_f \in [20; 80]$ cm/s, and that it is inversely proportional to the friction speed.

In figure 2.25, the two-dimensional **monostatic** shadowing function is represented as a function of directions $\{\theta, \phi\}$, and for different values of the wind speeds $u_f = \{20, 40, 60, 80\}$ cm/s. We notice that the shadowing effect is important for angles close to 90° , i.e., when the correlation becomes not negligible. We also observe that the results are hardly appreciable according to ϕ , so the shadowing function does not depend in a significant way on the anisotropic medium.

In figure 2.26, the two-dimensional **bistatic** shadowing function is plotted as a function of directions $\{\theta_2, \phi\}$ with $\phi = \phi_1 = \phi_2$, for

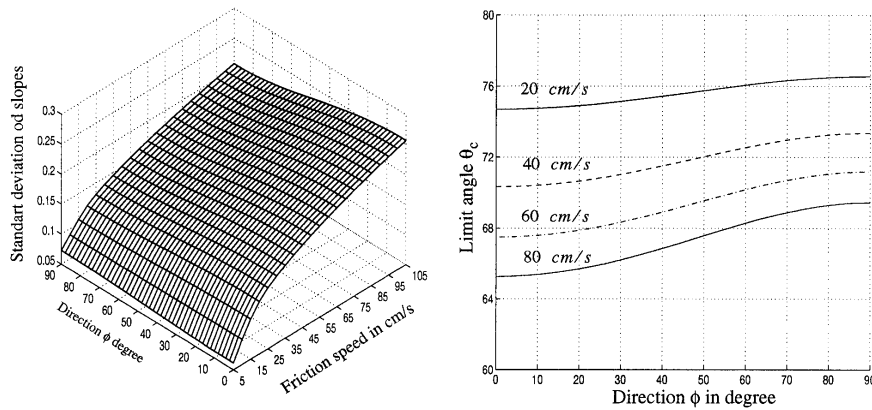


Figure 2.24 Standard deviation of slopes as a function of the friction speed and the direction ϕ Limit angle as a function of the observation direction ϕ .

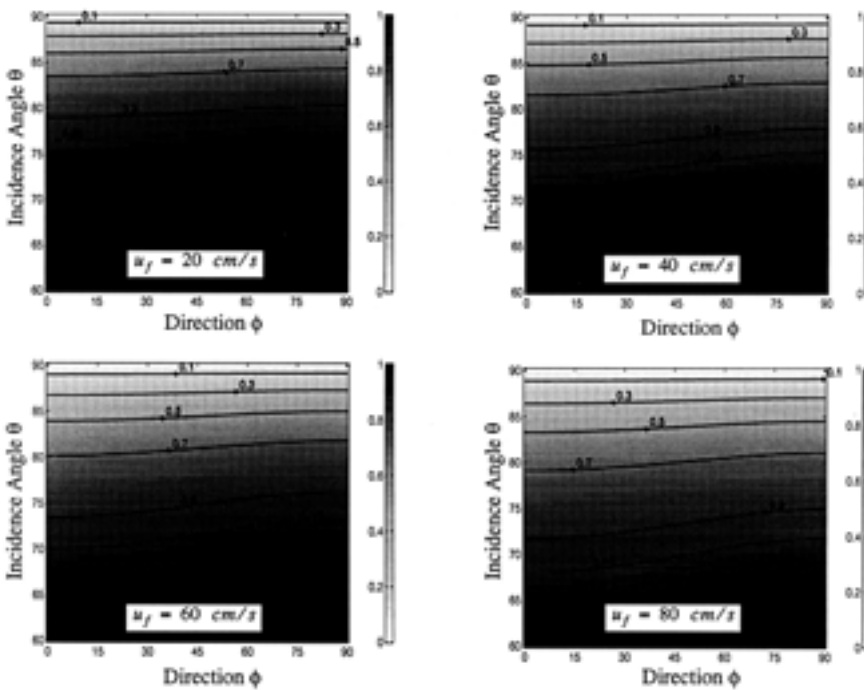


Figure 2.25 The Smith two-dimensional monostatic shadowing function as a function of observation directions, for different wind speeds.

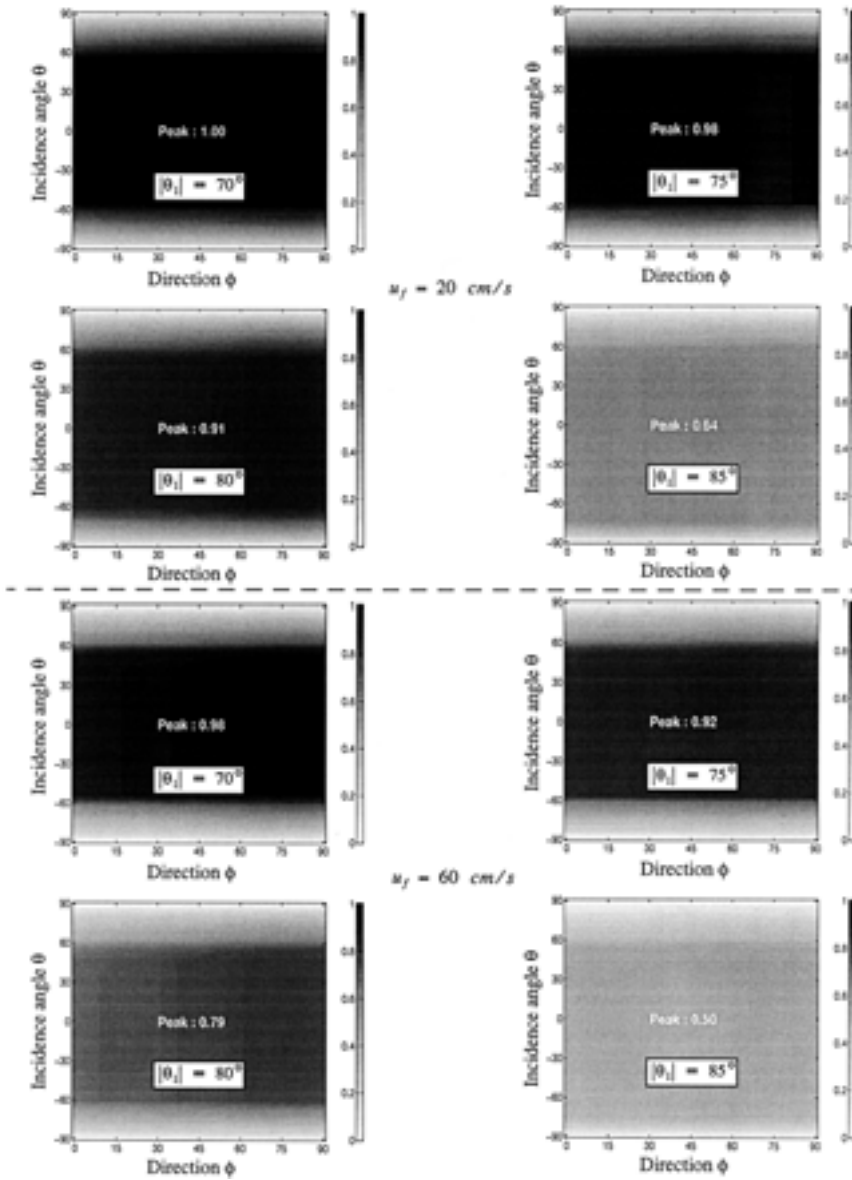


Figure 2.26 The Smith uncorrelated bistatic two-dimensional shadowing function as a function of $\{\theta_2, \phi = \phi_1 = \phi_2\}$, and for an incidence angle $|\theta_1|$ and a friction speed u_f given.

different incident angles $|\theta_1| = \{70, 75, 80, 85\}^\circ$ and friction speeds $u_f = \{20, 60\}$ cm/s. We observe that when the incident angle θ_1 is near 90° the shadow becomes more greater.

2.5.2 Generalization of the Monostatic and Bistatic Cases with Correlation

When the correlation is included in the one-dimensional case, the calculus of the conditional probability is based on the determination of the probability density $p(\xi = \xi_0 + \mu\tau, \gamma|\xi_0, \gamma_0; \tau)$. This quantity has to be extended in the two-dimensional case.

2.5.2.1 The Height and Slope Joint Probability in Cartesian Coordinates

The probability density $p(\xi, \gamma|\xi_0, \gamma_0; \tau)$ in the directions $\{(0x), (0y)\}$ becomes:

$$p(\xi, \gamma_x, \gamma_y|\xi_0, \gamma_{0x}, \gamma_{0y}; x, y) \quad (2.42)$$

Using the Bayes theorem, we have:

$$p(\xi, \gamma_x, \gamma_y|\xi_0, \gamma_{0x}, \gamma_{0y}; x, y) = p(\xi_0, \xi, \gamma_{0x}, \gamma_x, \gamma_{0y}, \gamma_y; x, y)/p(\xi_0, \gamma_{0x}, \gamma_{0y}) \quad (2.42a)$$

For a six dimension gaussian process $p(\xi_0, \xi, \gamma_{0x}, \gamma_x, \gamma_{0y}, \gamma_y; x, y)$ is:

$$p(\xi_0, \xi, \gamma_{0x}, \gamma_x, \gamma_{0y}, \gamma_y; x, y) = \frac{1}{(2\pi)^3 \sqrt{|[C^{xy}]|}} \exp\left(-\frac{1}{2} \overrightarrow{V^{xy}}^T [C^{xy}]^{-1} \overrightarrow{V^{xy}}\right) \quad (2.43)$$

with

$$\overrightarrow{V^{xy}} = [\xi_0, \xi, \gamma_{0x}, \gamma_x, \gamma_{0y}, \gamma_y] \quad (2.43a)$$

where $|[C^{xy}]|$ is the determinant of the covariance matrix $[C^{xy}]$. The exponent xy denotes the choice of the base. Using the same way as exposed in appendix 3, we show:

$$[C^{xy}] = \begin{bmatrix} R_0(\vec{0}) & R_0 & -R_{1x}(\vec{0}) & R_{1x} & -R_{1y}(\vec{0}) & R_{1y} \\ R_0 & R_0(\vec{0}) & -R_{1x} & -R_{1x}(\vec{0}) & -R_{1y} & -R_{1y}(\vec{0}) \\ -R_{1x}(\vec{0}) & -R_{1x} & -R_{2x}(\vec{0}) & -R_{2x} & -R_{2xy}(\vec{0}) & -R_{2xy} \\ R_{1x} & -R_{1x}(\vec{0}) & -R_{2x} & -R_{2x}(\vec{0}) & -R_{2xy} & -R_{2xy}(\vec{0}) \\ -R_{1y}(\vec{0}) & -R_{1y} & -R_{2xy}(\vec{0}) & -R_{2xy} & -R_{2y}(\vec{0}) & -R_{2y} \\ R_{1y} & -R_{1y}(\vec{0}) & -R_{2xy} & -R_{2xy}(\vec{0}) & -R_{2y} & -R_{2y}(\vec{0}) \end{bmatrix} \quad (2.44)$$

with

$$\begin{cases} R_{1x} = \frac{\partial R_0}{\partial x} & R_{1y} = \frac{\partial R_0}{\partial y} \\ R_{2x} = \frac{\partial^2 R_0}{\partial x^2} & R_{2y} = \frac{\partial^2 R_0}{\partial y^2} & R_{2xy} = \frac{\partial^2 R_0}{\partial x \partial y} \end{cases}$$

where $R_0(x, y)$ is the autocorrelation function in Cartesian coordinates. The spectrum being even according to $\{x, y\}$ involves an even autocorrelation function, R_0 depends then on $X = x^2$, $Y = y^2$. Thus, we show:

$$\begin{aligned} R_{1x}(\vec{0}) &= \left[2x \frac{\partial R_0}{\partial X} \right]_{\substack{x=0 \\ y=0}} = 0 & R_{1y}(\vec{0}) &= \left[2y \frac{\partial R_0}{\partial Y} \right]_{\substack{x=0 \\ y=0}} = 0 \\ R_{2xy}(\vec{0}) &= 4 \left[xy \frac{\partial^2 R_0}{\partial X \partial Y} \right]_{\substack{x=0 \\ y=0}} = 0 \end{aligned} \quad (2.44a)$$

Substituting equations (2.44a) into (2.44), the covariance matrix of the probability density $p(\xi_0, \xi, \gamma_{0x}, \gamma_x, \gamma_{0y}, \gamma_y; x, y)$ is:

$$[C^{xy}] = \begin{bmatrix} \omega^2 & R_0 & 0 & R_{1x} & 0 & R_{1y} \\ R_0 & \omega^2 & -R_{1x} & 0 & -R_{1y} & 0 \\ 0 & -R_{1x} & \sigma_x^2 & -R_{2x} & 0 & -R_{2xy} \\ R_{1x} & 0 & -R_{2x} & \sigma_x^2 & -R_{2xy} & 0 \\ 0 & -R_{1y} & 0 & -R_{2xy} & \sigma_y^2 & -R_{2y} \\ R_{1y} & 0 & -R_{2xy} & 0 & -R_{2y} & \sigma_y^2 \end{bmatrix} \quad (2.44b)$$

where $R_0(\vec{0}) = \omega^2$ is the height variance, and $\{-R_{2x}(\vec{0}) = \sigma_x^2, -R_{2y}(\vec{0}) = \sigma_y^2\}$ the slope variances in the upwind and crosswind directions. We notice that the matrix $[C^{xy}]$ is symmetrical. In order to follow the same approach as for the one-dimensional case, $p(\xi_0, \xi, \gamma_{0x}, \gamma_x, \gamma_{0y}, \gamma_y; x, y)$ must be expressed in the polar coordinates.

2.5.2.2 The Height and Slope Joint Probability in Polar Coordinates

The vector $\overset{\longrightarrow}{V}^{xy} = [\xi_0 \ \xi \ \gamma_{0x} \ \gamma_x \ \gamma_{0y} \ \gamma_y]$ in the (x, y) base is obtained from vector $\overset{\longrightarrow}{V}^{XY} = [\xi_0 \ \xi \ \gamma_{0X} \ \gamma_X \ \gamma_{0Y} \ \gamma_Y]$ in the new (X, Y) base by

(generalization of equation (2.39a)):

$$\begin{aligned} \overrightarrow{V^{xy}} &= \begin{bmatrix} \xi_0 \\ \xi \\ \gamma_{0x} \\ \gamma_x \\ \gamma_{0y} \\ \gamma_y \end{bmatrix} = \begin{bmatrix} 1 & 0 & 0 & 0 & 0 & 0 \\ 0 & 1 & 0 & 0 & 0 & 0 \\ 0 & 0 & \cos \phi & 0 & -\sin \phi & 0 \\ 0 & 0 & 0 & \cos \phi & 0 & -\sin \phi \\ 0 & 0 & \sin \phi & 0 & \cos \phi & 0 \\ 0 & 0 & 0 & \sin \phi & 0 & \cos \phi \end{bmatrix} \begin{bmatrix} \xi_0 \\ \xi \\ \gamma_{0X} \\ \gamma_X \\ \gamma_{0Y} \\ \gamma_Y \end{bmatrix} \\ &= [O_6] \overrightarrow{V^{XY}} \end{aligned} \quad (2.45)$$

thus:

$$\begin{aligned} \overrightarrow{V^{xy}} [C^{xy}]^{-1} \overrightarrow{V^{xy}} &= \overrightarrow{V^{XY}} [O_6]^T [C^{xy}]^{-1} [O_6] \overrightarrow{V^{XY}} \\ &= \overrightarrow{V^{XY}} ([O_6]^{-1} [C^{xy}] [O_6])^{-1} \overrightarrow{V^{XY}} \end{aligned} \quad (2.45a)$$

We notice that $[O_6]^T = [O_6]^{-1}$. Moreover we show:

$$\begin{aligned} [C^{XY}] &= [O_6]^{-1} [C^{xy}] [O_6] \\ &= \begin{bmatrix} \omega^2 & R_0 & 0 & C_{14}^{XY} & 0 & C_{16}^{XY} \\ R_0 & \omega^2 & -C_{14}^{XY} & 0 & -C_{16}^{XY} & 0 \\ 0 & -C_{14}^{XY} & C_{33}^{XY} & C_{34}^{XY} & C_{35}^{XY} & -C_{36}^{XY} \\ C_{14}^{XY} & 0 & C_{34}^{XY} & C_{33}^{XY} & -C_{36}^{XY} & C_{35}^{XY} \\ 0 & -C_{16}^{XY} & C_{35}^{XY} & -C_{36}^{XY} & C_{55}^{XY} & -C_{56}^{XY} \\ C_{16}^{XY} & 0 & -C_{36}^{XY} & C_{35}^{XY} & -C_{56}^{XY} & C_{55}^{XY} \end{bmatrix} \end{aligned} \quad (2.45b)$$

with

$$\begin{cases} C_{14}^{XY} = R_{1x} \cos \phi + R_{1y} \sin \phi \\ C_{16}^{XY} = -R_{1x} \sin \phi + R_{1y} \cos \phi \\ C_{34}^{XY} = -R_{2x} \cos(\phi)^2 - R_{2y} \sin(\phi)^2 - R_{2xy} \sin(2\phi) \\ C_{36}^{XY} = -\frac{(R_{2x} - R_{2y})}{2} \sin(2\phi) + R_{2xy} \cos(2\phi) \\ C_{56}^{XY} = R_{2x} \sin(\phi)^2 + R_{2y} \cos(\phi)^2 - R_{2xy} \sin(2\phi) \\ C_{33}^{XY} = \sigma_x^2 \cos(\phi)^2 + \sigma_y^2 \sin(\phi)^2 \\ C_{35}^{XY} = -\frac{(\sigma_x^2 - \sigma_y^2)}{2} \sin(2\phi) \\ C_{55}^{XY} = \sigma_x^2 \sin(\phi)^2 + \sigma_y^2 \cos(\phi)^2 \end{cases} \quad (2.45c)$$

Writing:

$$\left\{ \begin{array}{l} R_{1x} = \frac{\partial R_0}{\partial x} = \frac{\partial R_0}{\partial R} \frac{\partial R}{\partial x} + \frac{\partial R_0}{\partial \phi} \frac{\partial \phi}{\partial x} \\ R_{1y} = \frac{\partial R_0}{\partial y} = \frac{\partial R_0}{\partial R} \frac{\partial R}{\partial y} + \frac{\partial R_0}{\partial \phi} \frac{\partial \phi}{\partial y} \\ R_{2x} = \frac{\partial R_{1x}}{\partial x} = \frac{\partial R_{1x}}{\partial R} \frac{\partial R}{\partial x} + \frac{\partial R_{1x}}{\partial \phi} \frac{\partial \phi}{\partial x} \\ R_{2y} = \frac{\partial R_{1y}}{\partial y} = \frac{\partial R_{1y}}{\partial R} \frac{\partial R}{\partial y} + \frac{\partial R_{1y}}{\partial \phi} \frac{\partial \phi}{\partial y} \\ R_{2xy} = \frac{\partial R_{1x}}{\partial y} = \frac{\partial R_{1x}}{\partial R} \frac{\partial R}{\partial y} + \frac{\partial R_{1x}}{\partial \phi} \frac{\partial \phi}{\partial y} \end{array} \right. \quad (2.45d)$$

we show that the functions C_{ij}^{XY} in polar coordinates are given by:

$$\left\{ \begin{array}{l} C_{14}^{XY} = \frac{\partial R_0}{\partial R} = R_{1R} \quad C_{16}^{XY} = \frac{1}{R} \frac{\partial R_0}{\partial \phi} = \frac{R_{1\phi}}{R} \\ C_{34}^{XY} = -\frac{\partial^2 R_0}{\partial R^2} = -R_{2R} \\ C_{36}^{XY} = -\frac{1}{R^2} \left(\frac{\partial R_0}{\partial \phi} - R \frac{\partial^2 R_0}{\partial R \partial \phi} \right) = -\frac{1}{R^2} (R_{1\phi} - RR_{2R\phi}) \\ C_{56}^{XY} = \frac{1}{R^2} \left(R \frac{\partial R_0}{\partial R} + \frac{\partial^2 R_0}{\partial \phi^2} \right) = \frac{1}{R^2} (RR_{1R} + R_{2\phi}) \end{array} \right. \quad (2.45e)$$

where $R_0(R, \phi)$ is the autocorrelation function in polar coordinates. In the first chapter we have shown that R_0 is given by (equation (1.41)):

$$R_0(R, \phi) = I_0(R) - \cos(2\phi)I_2(R) \quad (2.46)$$

where I_0 denotes the isotropic part, whereas I_2 is the anisotropic part. Substituting equations (2.46) and (2.45e) into (2.45c), the probability density $p\left(\overrightarrow{V}^{XY}; R, \phi\right)$ in the base (X, Y) and in polar coordinates is (jacobian $J = |[O_6]| = 1$):

$$p(\xi_0, \xi, \gamma_{0X}, \gamma_X, \gamma_{0Y}, \gamma_Y; R, \phi) = \frac{1}{(2\pi)^3 \sqrt{|[C^{XY}]|}} \cdot \exp\left(-\frac{1}{2} \overrightarrow{V}^{XYT} [C^{XY}]^{-1} \overrightarrow{V}^{XY}\right) \quad (2.47)$$

with

$$[C^{XY}] = \begin{bmatrix} \omega^2 & R_0 & 0 & R_{1R} & 0 & C_{16}^{XY} \\ R_0 & \omega^2 & -R_{1R} & 0 & -C_{16}^{XY} & 0 \\ 0 & -R_{1R} & \sigma_X^2 & -R_{2R} & \sigma_{XY}^2 & -C_{36}^{XY} \\ R_{1R} & 0 & -R_{2R} & \sigma_X^2 & -C_{36}^{XY} & \sigma_{XY}^2 \\ 0 & -C_{16}^{XY} & \sigma_{XY}^2 & -C_{36}^{XY} & \sigma_Y^2 & -C_{56}^{XY} \\ C_{16}^{XY} & 0 & -C_{36}^{XY} & C_{36}^{XY} & -C_{56}^{XY} & \sigma_Y^2 \end{bmatrix}$$

$$\begin{cases} R_0 = I_0 - \cos(2\phi)I_2 \\ R_{1R} = \frac{\partial R_0}{\partial R} = \frac{dI_0}{dR} - \cos(2\phi) \frac{dI_2}{dR} \\ R_{2R} = \frac{\partial^2 R_0}{\partial R^2} = \frac{d^2 I_0}{dR^2} - \cos(2\phi) \frac{d^2 I_2}{dR^2} \\ C_{16}^{XY} = \frac{1}{R} \frac{\partial R_0}{\partial \phi} = \frac{2I_2 \sin(2\phi)}{R} \\ C_{36}^{XY} = \frac{2 \sin(2\phi)}{R^2} \left(R \frac{dI_2}{dR} - I_2 \right) \\ C_{56}^{XY} = \frac{1}{R} \frac{dI_0}{dR} - \frac{\cos(2\phi)}{R^2} \left(R \frac{dI_2}{dR} - 4I_2 \right) \\ \omega^2 = R_0(0) \quad \sigma_{XY}^2 = -\beta \sin 2\phi \\ \sigma_X^2 = \alpha + \beta \cos(2\phi) \\ \sigma_Y^2 = \alpha - \beta \cos(2\phi) \end{cases} \quad (2.47a)$$

and

$$\alpha = \frac{\sigma_x^2 + \sigma_y^2}{2} \quad \beta = \frac{\sigma_x^2 - \sigma_y^2}{2} \quad (2.47b)$$

where $\{\sigma_x^2, \sigma_y^2\}$ are the slope variances in the upwind and crosswind directions. The covariance matrix corresponding to $p(\xi_0, \gamma_{0X}, \gamma_{0Y})$ is given by:

$$p(\xi_0, \gamma_{0X}, \gamma_{0Y}) = \frac{1}{\sqrt{2\pi}^3} \left| \begin{bmatrix} C_{11}^{XY} & C_{13}^{XY} & C_{15}^{XY} \\ C_{31}^{XY} & C_{33}^{XY} & C_{35}^{XY} \\ C_{51}^{XY} & C_{53}^{XY} & C_{55}^{XY} \end{bmatrix} \right|^{-\frac{1}{2}} \cdot \exp \left(-\frac{1}{2} [\xi_0 \ \gamma_{0X} \ \gamma_{0Y}] \begin{bmatrix} C_{11}^{XY} & C_{13}^{XY} & C_{15}^{XY} \\ C_{31}^{XY} & C_{33}^{XY} & C_{35}^{XY} \\ C_{51}^{XY} & C_{53}^{XY} & C_{55}^{XY} \end{bmatrix}^{-1} \begin{bmatrix} \xi_0 \\ \gamma_{0X} \\ \gamma_{0Y} \end{bmatrix} \right) \quad (2.48)$$

with

$$\begin{bmatrix} C_{11}^{XY} & C_{13}^{XY} & C_{15}^{XY} \\ C_{31}^{XY} & C_{33}^{XY} & C_{35}^{XY} \\ C_{51}^{XY} & C_{53}^{XY} & C_{55}^{XY} \end{bmatrix} = \begin{bmatrix} \omega^2 & 0 & 0 \\ 0 & \sigma_X^2 & \sigma_{XY}^2 \\ 0 & \sigma_{XY}^2 & \sigma_Y^2 \end{bmatrix} \quad (2.48a)$$

Substituting equations (2.48) and (2.47) into (2.42a), we obtain:

$$\begin{aligned}
 p(\xi, \gamma_X, \gamma_Y | \xi_0, \gamma_{0X}, \gamma_{0Y}; R, \phi) &= \frac{\omega \sigma_Y \sigma_X \sqrt{1 - \rho^2}}{\sqrt{2\pi^3} \sqrt{|C^{XY}|}} \exp \left[-\frac{1}{2} \overrightarrow{V^{XY}}^T [C^{XY}]^{-1} \overrightarrow{V^{XY}} \right. \\
 &\quad \left. + \frac{\xi_0^2}{2\omega^2} + \frac{1}{2(1 - \rho^2)} \left(\frac{\gamma_{0X}^2}{\sigma_X^2} + \frac{\gamma_{0Y}^2}{\sigma_Y^2} - \frac{2\rho\gamma_{0X}\gamma_{0Y}}{\sigma_X\sigma_Y} \right) \right] \\
 \text{with } \rho &= \frac{\sigma_{XY}^2}{\sigma_X\sigma_Y} \tag{2.49}
 \end{aligned}$$

where the covariance matrix is given by equation (2.47a).

2.5.2.3 The Height and Slope Joint Marginal Probability

The marginal probability density $p(\xi, \gamma_X | \xi_0, \gamma_{0X}; R, \phi)$ is obtained by integrating equation (2.49) over the interval $\gamma_Y \in]-\infty; \infty[$. So it is based on the calculus of the inverse matrix $[C^{XY}]^{-1}$, which is very difficult to find analytically.

We use an analytic-numeric approach, that is to say the inverse matrix is estimated numerically, whereas the marginal probability is determined by using the analytic properties of the inverse matrix. Then we show:

$$[C^{XY}]^{-\Lambda} = \frac{1}{|[C^{XY}]|} \begin{bmatrix} C_{i11}^{XY} & C_{i12}^{XY} & C_{i13}^{XY} & C_{i14}^{XY} & C_{i15}^{XY} & C_{i16}^{XY} \\ C_{i12}^{XY} & C_{i11}^{XY} & -C_{i14}^{XY} & -C_{i13}^{XY} & -C_{i16}^{XY} & -C_{i15}^{XY} \\ C_{i13}^{XY} & -C_{i14}^{XY} & C_{i33}^{XY} & C_{i34}^{XY} & C_{i35}^{XY} & C_{i36}^{XY} \\ C_{i14}^{XY} & -C_{i13}^{XY} & C_{i34}^{XY} & C_{i33}^{XY} & C_{i36}^{XY} & C_{i35}^{XY} \\ C_{i15}^{XY} & -C_{i16}^{XY} & C_{i35}^{XY} & C_{i36}^{XY} & C_{i55}^{XY} & C_{i56}^{XY} \\ C_{i16}^{XY} & -C_{i15}^{XY} & C_{i36}^{XY} & C_{i35}^{XY} & C_{i56}^{XY} & C_{i55}^{XY} \end{bmatrix} \tag{2.50}$$

where C_{ij}^{XY} are the elements of the inverse covariance matrix $[C^{XY}]$ multiplied by the determinant $|[C^{XY}]|$. They are obtained numerically. Moreover:

$$\begin{aligned}
 \begin{cases} \begin{bmatrix} \gamma_x \\ \gamma_y \end{bmatrix} &= \begin{bmatrix} \cos \phi & -\sin \phi \\ \sin \phi & \cos \phi \end{bmatrix} \begin{bmatrix} \gamma_X \\ \gamma_Y \end{bmatrix} \\ \begin{bmatrix} \gamma_{0x} \\ \gamma_{0y} \end{bmatrix} &= \begin{bmatrix} \cos \phi & -\sin \phi \\ \sin \phi & \cos \phi \end{bmatrix} \begin{bmatrix} \gamma_{0X} \\ \gamma_{0Y} \end{bmatrix} \end{cases} \\
 \Rightarrow \begin{bmatrix} \gamma_x - \gamma_{0x} \\ \gamma_y - \gamma_{0y} \end{bmatrix} &= \begin{bmatrix} \cos \phi & -\sin \phi \\ \sin \phi & \cos \phi \end{bmatrix} \begin{bmatrix} \gamma_X - \gamma_{0X} \\ \gamma_Y - \gamma_{0Y} \end{bmatrix} \tag{2.50a}
 \end{aligned}$$

and

$$\xi = \xi_0 + \mu R \quad \Rightarrow \quad \begin{cases} \gamma_x = \frac{\partial \xi}{\partial x} = \frac{\partial \xi_0}{\partial x} + \mu \frac{\partial R}{\partial x} = \gamma_{0x} + \mu \cos \phi \\ \gamma_y = \frac{\partial \xi}{\partial y} = \frac{\partial \xi_0}{\partial y} + \mu \frac{\partial R}{\partial y} = \gamma_{0y} + \mu \sin \phi \end{cases} \quad (2.50b)$$

Substituting equation (2.50b) into (2.50a), we have:

$$\begin{aligned} \begin{bmatrix} \gamma_X - \gamma_{0X} \\ \gamma_Y - \gamma_{0Y} \end{bmatrix} &= \begin{bmatrix} \cos \phi & -\sin \phi \\ \sin \phi & \cos \phi \end{bmatrix}^{-1} \begin{bmatrix} \mu \cos \phi \\ \mu \sin \phi \end{bmatrix} = \begin{bmatrix} \mu \\ 0 \end{bmatrix} \\ &\Rightarrow \begin{cases} \gamma_X = \gamma_{0X} + \mu \\ \gamma_Y = \gamma_{0Y} \end{cases} \end{aligned} \quad (2.50c)$$

Using equations (2.50c), (2.50) and (2.49), we show that the probability density $p(\xi, \gamma_X, \gamma_Y | \xi_0, \gamma_{0X}, \gamma_Y; R, \phi)$ is:

$$\begin{aligned} p(\xi, \gamma_X, \gamma_Y | \xi_0, \gamma_{0X}, \gamma_Y; R, \phi) &= \frac{\omega \sigma_Y \sigma_X \sqrt{1 - \rho^2}}{\sqrt{2\pi}^3 \sqrt{|[C^{XY}]|}} \\ &\quad \cdot \exp(-A_2 \gamma_Y^2 - 2B_2 \gamma_Y - C_2) \end{aligned} \quad (2.51)$$

with

$$\begin{cases} A_2 = \frac{C_{i55}^{XY} + C_{i56}^{XY}}{|[C^{XY}]|} - \frac{1}{2\sigma_Y^2(1 - \rho^2)} \\ B_2 = \frac{(\xi_0 - \xi)(C_{i15}^{XY} + C_{i16}^{XY}) + (\gamma_{0X} + \gamma_X)(C_{i35}^{XY} + C_{i36}^{XY})}{2|[C^{XY}]|} \\ \quad + \frac{\rho \gamma_{0X}}{2\sigma_X \sigma_Y(1 - \rho^2)} \\ C_2 = -\frac{\gamma_{0X}^2}{2\sigma_X^2(1 - \rho^2)} - \frac{\xi_0^2}{2\omega^2} \end{cases} \quad (2.51a)$$

Using equation (2.40c), the marginal probability density $p(\xi, \gamma_X | \xi_0, \gamma_{0X}; R, \phi)$ is then equal to:

$$\begin{aligned} &p(\xi, \gamma_X | \xi_0, \gamma_{0X}; R, \phi) \\ &= \int_{-\infty}^{\infty} p(\xi, \gamma_X, \gamma_Y | \xi_0, \gamma_{0X}, \gamma_Y; R, \phi) d\gamma_Y \end{aligned}$$

$$\begin{aligned}
 &= \frac{\omega\sigma_Y\sigma_X\sqrt{1-\rho^2}}{\sqrt{2\pi^3}\sqrt{|[C^{XY}]|}}\sqrt{\frac{\pi}{A_2}}\times\exp\left(\frac{B_2^2}{A_2}-C_2\right) \\
 &= \frac{\omega\sigma_X\sqrt{1-\rho^2}}{2\pi\sqrt{E/\sigma_Y^2}}\exp\left(\frac{\xi_0^2}{2\omega^2}+\frac{\gamma_{0X}^2}{2\sigma_X^2}-\frac{a_1\xi_0^2+a_2\xi^2+a_9\gamma_X^2+a_{10}\gamma_{0X}^2}{2|[C^{XY}]|}\right. \\
 &\quad \left.-\frac{a_3\xi_0\xi+a_4\gamma_{0X}\gamma_X+a_5\xi_0\gamma_{0X}-a_6\xi\gamma_X+a_7\xi_0\gamma_X-a_8\xi\gamma_{0X}}{|[C^{XY}]|}\right)
 \end{aligned} \tag{2.52}$$

with:

$$\left\{ \begin{aligned}
 a_1 &= a_2 = C_{i11}^{XY} - \frac{(C_{i15}^{XY} + C_{i16}^{XY})^2}{E} \\
 E &= 2A_2|[C^{XY}]| = 2(C_{i55}^{XY} + C_{i56}^{XY}) - \frac{|[C^{XY}]|}{\sigma_Y^2(1-\rho^2)} \\
 a_3 &= C_{i12}^{XY} + \frac{(C_{i15}^{XY} + C_{i16}^{XY})^2}{E} \\
 a_4 &= C_{i34}^{XY} - \frac{(C_{i35}^{XY} + C_{i36}^{XY})^2}{E} - \frac{\rho(C_{i35}^{XY} + C_{i36}^{XY})}{2A_2\sigma_X\sigma_Y(1-\rho^2)} \\
 a_5 &= C_{i13}^{XY} - \frac{(C_{i15}^{XY} + C_{i16}^{XY})(C_{i35}^{XY} + C_{i36}^{XY})}{E} - \frac{\rho(C_{i15}^{XY} + C_{i16}^{XY})}{2A_2\sigma_X\sigma_Y(1-\rho^2)} \\
 a_6 &= C_{i13}^{XY} - \frac{(C_{i15}^{XY} + C_{i16}^{XY})(C_{i35}^{XY} + C_{i36}^{XY})}{E} \\
 a_7 &= C_{i14}^{XY} - \frac{(C_{i15}^{XY} + C_{i16}^{XY})(C_{i35}^{XY} + C_{i36}^{XY})}{E} \\
 a_8 &= C_{i14}^{XY} - \frac{(C_{i15}^{XY} + C_{i16}^{XY})(C_{i35}^{XY} + C_{i36}^{XY})}{E} - \frac{\rho(C_{i15}^{XY} + C_{i16}^{XY})}{2A_2\sigma_X\sigma_Y(1-\rho^2)} \\
 a_9 &= C_{i133}^{XY} - \frac{(C_{i35}^{XY} + C_{i36}^{XY})^2}{E} \\
 a_{10} &= C_{i133}^{XY} - \frac{(C_{i35}^{XY} + C_{i36}^{XY})^2}{E} \\
 &\quad - \left[\frac{\rho^2|[C^{XY}]|}{2A_2\sigma_X^2\sigma_Y^2(1-\rho^2)^2} + \frac{\rho(C_{i35}^{XY} + C_{i36}^{XY})}{A_2\sigma_X\sigma_Y(1-\rho^2)} + \frac{\rho^2|[C^{XY}]|}{\sigma_X^2(1-\rho^2)} \right]
 \end{aligned} \right. \tag{2.52a}$$

In the one-dimensional case the probability is given by (equation (2.13)):

$$\begin{aligned}
 & p(\xi, \gamma | \xi_0, \gamma_0; \tau) \\
 &= \frac{\sigma \omega}{2\pi \sqrt{|[C]|}} \times \exp \left[-\frac{C_{i11} (\xi_0^2 + \xi^2) + C_{i33} (\gamma_0^2 + \gamma^2)}{2|[C]|} + \frac{\xi_0^2}{2\omega^2} + \frac{\gamma_0^2}{2\sigma^2} \right. \\
 & \quad \left. - \frac{C_{i12}\xi_0\xi + 2C_{i34}\gamma_0\gamma + 2C_{i13}(\xi_0\gamma_0 - \xi\gamma) + 2C_{i14}(\xi_0\gamma - \xi\gamma_0)}{|[C]|} \right]
 \end{aligned} \tag{2.52b}$$

So by comparing equations (2.52) and (2.52b), the one-dimensional probability is obtained from the two-dimensional probability by substituting:

$$\frac{\omega \sigma_X \sqrt{1 - \rho^2}}{2\pi \sqrt{E/\sigma_Y^2}} \quad \text{to} \quad \frac{\omega \sigma}{2\pi \sqrt{|[C]|}} \quad \begin{cases} \sigma_X & \text{to} & \sigma \\ \gamma_X & \text{to} & \gamma \\ \gamma_{0X} & \text{to} & \gamma_0 \end{cases} \tag{2.52c}$$

and

$$\begin{cases} a_1, a_2 & \text{to} & C_{i11} \\ a_9, a_{10} & \text{to} & C_{i33} \\ a_3 & \text{to} & C_{i12} \end{cases} \quad \begin{cases} a_4 & \text{to} & C_{i34} \\ a_5, a_6 & \text{to} & C_{i13} \\ a_7, a_8 & \text{to} & C_{i14} \end{cases} \tag{2.52d}$$

The calculus of the two-dimensional probability requires 9 coefficients $a_{i \in [2;10]}$, whereas in the one-dimensional case we have 6 coefficients.

Uncorrelated surface

The correlation is negligible when:

$$I_0 = 0 \quad I_2 = 0 \tag{2.53}$$

Then, the covariance matrix in polar coordinates is (equation (2.47a)):

$$[C^{XY}] = \begin{bmatrix} \omega^2 & 0 & 0 & 0 & 0 & 0 \\ 0 & \omega^2 & 0 & 0 & 0 & 0 \\ 0 & 0 & \sigma_X^2 & 0 & \rho\sigma_X\sigma_Y & 0 \\ 0 & 0 & 0 & \sigma_X^2 & 0 & \rho\sigma_X\sigma_Y \\ 0 & 0 & \rho\sigma_X\sigma_Y & 0 & \sigma_Y^2 & 0 \\ 0 & 0 & 0 & \rho\sigma_X\sigma_Y & 0 & \sigma_Y^2 \end{bmatrix}$$

$$\text{with} \quad \rho = \frac{\sigma_{XY}^2}{\sigma_X\sigma_Y} \tag{2.53a}$$

This equation corresponds to the classical probability density of gaussian process without correlation

Probability expression in the isotropic case

If the surface is isotropic, then $I_2(R) = 0$ and

$$C_{16}^{XY} = 0 \quad C_{36}^{XY} = 0 \quad \sigma_{XY}^2 = 0 \Rightarrow \rho = 0 \quad (2.55)$$

The covariance matrix $[C^{XY}]$ is given by:

$$[C^{XY}] = \begin{bmatrix} [C] & [0] \\ [0] & [Q] \end{bmatrix} \quad (2.55a)$$

$[C^{XY}]$ is then composed of two matrices $\{[C], [Q]\}$, where $[C]$ corresponds to the one-dimensional covariance matrix obtained from appendix 3 (equation (3.3c)) with $R_1 = R_{1R}$, $R_2 = R_{2R}$. The inverse matrix is:

$$[C^{XY}]^{-1} = \frac{1}{|[C]||[Q]|} \begin{bmatrix} [C]^{-1} & [0] \\ [0] & [Q]^{-1} \end{bmatrix} \quad (2.55b)$$

Moreover we show from equations (2.52a) that:

$$\begin{cases} a_1 = a_2 = C_{i11}^{XY} = C_{i11} & a_5 = a_6 = C_{i13}^{XY} = C_{i13} \\ a_3 = C_{i12}^{XY} = C_{i12} & a_7 = a_8 = C_{i14}^{XY} = C_{i14} \\ a_4 = C_{i34}^{XY} = C_{i34} & a_9 = a_{10} = C_{i33}^{XY} = C_{i33} \\ E = \frac{|[C^{XY}]| \sigma_Y^2}{|[Q]|} \left(1 - \frac{C_{56}^{XY}}{\sigma_Y^2}\right)^2 = |[C]| \sigma_Y^2 \left(1 - \frac{C_{56}^{XY}}{\sigma_Y^2}\right)^2 \end{cases} \quad (2.55c)$$

Substituting equation (2.55c) into (2.52), $p(\xi, \gamma_X | \xi_0, \gamma_{0X}; R)$ becomes:

$$\begin{aligned} & p(\xi, \gamma_X | \xi_0, \gamma_{0X}; R) \\ &= \frac{\omega \sigma_X}{2\pi \left|1 - \frac{C_{56}^{XY}}{\sigma_Y^2}\right| \sqrt{|[C]|}} \\ & \times \exp \left[\frac{\xi_0^2}{2\omega^2} + \frac{\gamma_{0X}^2}{2\sigma_X^2} - \frac{C_{i11}(\xi_0^2 + \xi^2) + C_{i33}(\gamma_{0X}^2 + \gamma_X^2)}{2|[C^{XY}]}\right. \\ & \left. - \frac{2C_{i12}\xi_0\xi + 2C_{i34}\gamma_{0X}\gamma_X + 2C_{i13}(\xi_0\gamma_{0X} - \xi\gamma_X) + 2C_{i14}(\xi_0\gamma_X - \xi\gamma_{0X})}{2|[C^{XY}]}\right] \end{aligned} \quad (2.55d)$$

We obtain the same solution that in the one-dimensional case (equation (2.52b)) with:

$$\gamma_X = \gamma \quad \gamma_{0X} = \gamma_0 \quad \sigma_X = \sigma \quad \sqrt{|[C]|} \rightarrow \sqrt{|[C]|} \left| 1 - \frac{C_{56}^{XY}}{\sigma_Y^2} \right| \quad (2.55e)$$

2.5.2.4 The Smith Conditional Probability

In appendix 6 we show that the Smith two-dimensional conditional probability $g_S(R, \phi | \{\xi_0, \gamma_{0X}\}, \theta)$ is given by:

$$g_S = \frac{1}{\pi} \sqrt{\frac{A_{1X}}{A_X}} \times \frac{\left(\exp[-C_X - \mu(\mu A_X + 2B_X)] \times \left[1 - e^{-\frac{(B_X + \mu A)^2}{A}} \sqrt{\pi} \frac{B_X + \mu A_X}{\sqrt{A_X}} \operatorname{erfc} \left(\frac{B_X + \mu A_X}{\sqrt{A_X}} \right) \right] \right)}{\exp \left(\frac{B_{1X}^2}{A_{1X}} - C_{1X} \right) \left\{ \operatorname{erf} \left[\frac{A_{1X} \xi + B_{1X}}{\sqrt{A_{1X}}} \right] + 1 \right\}} \quad (2.56)$$

with

$$\begin{cases} A_X = \frac{a_9}{2|[C^{XY}]|} & B_X = \frac{a_7 \xi_0 - a_9 \xi + a_4 \gamma_{0X}}{2|[C^{XY}]|} \\ C_X = \frac{a_1 \xi_0^2 + a_2 \xi^2 + 2a_3 \xi_0 \xi + 2a_5 \xi_0 \gamma_{0X} - 2a_8 \xi \gamma_{0X} + 2a_{10} \gamma_{0X}^2}{2|[C^{XY}]|} \end{cases} \quad (2.56a)$$

and:

$$\begin{cases} A_{1X} = (a_2 a_9 - a_6^2) E_{1X} & E_{1X} = \frac{1}{2a_9 |[C^{XY}]|} \\ B_{1X} = [\xi_0 (a_3 a_9 + a_6 a_7) + \gamma_0 (a_6 a_4 - a_8 a_9)] E_{1X} \\ C_{1X} = [\xi_0^2 (a_1 a_9 - a_7^2) + \gamma_0^2 (a_{10} a_9 - a_4^2) + 2\xi_0 \gamma_0 (a_5 a_9 - a_4 a_7)] E_{1X} \end{cases} \quad (2.56b)$$

Applying equations (2.52d), equations $\{(2.56), (2.56a), (2.56b)\}$ are similar to $\{(2.15), (2.15a), (2.14a)\}$, respectively.

2.5.2.5 The Smith Shadowing Function

We have seen in paragraph 2.5.2.3 that the correlated two-dimensional shadowing function is obtained from the correlated one-dimen-

sional shadowing function by using equations (2.52c) and (2.52d). In order to use table 2.2, we must determine the f_{ij} functions in the two-dimensional case. Define the following relations:

$$\begin{cases} R_0 = \omega^2 f_0 & R_{1R} = -\omega \sigma_X f_{1R}, & R_{2R} = -\sigma_X^2 f_{2R} \\ C_{36}^{XY} = -\sigma_Y \sigma_X f_{36}^{XY} & C_{16}^{XY} = -\omega \sigma_Y f_{16}^{XY} & C_{56}^{XY} = -\sigma_Y^2 f_{56}^{XY} \end{cases} \quad (2.57)$$

We show that the inverse matrix $[f^{XY}]^{-1}$ keeps the similar structure that $[C^{XY}]^{-1}$:

$$[f^{XY}]^{-1} = \frac{1}{|[f^{XY}]|} \begin{bmatrix} f_{i11}^{XY} & f_{i12}^{XY} & f_{i13}^{XY} & f_{i14}^{XY} & f_{i15}^{XY} & f_{i16}^{XY} \\ f_{i12}^{XY} & f_{i11}^{XY} & -f_{i14}^{XY} & -f_{i13}^{XY} & -f_{i16}^{XY} & -f_{i15}^{XY} \\ f_{i13}^{XY} & -f_{i14}^{XY} & f_{i33}^{XY} & f_{i34}^{XY} & f_{i35}^{XY} & f_{i36}^{XY} \\ f_{i14}^{XY} & -f_{i13}^{XY} & f_{i34}^{XY} & f_{i33}^{XY} & f_{i36}^{XY} & f_{i35}^{XY} \\ f_{i15}^{XY} & -f_{i16}^{XY} & f_{i35}^{XY} & f_{i36}^{XY} & f_{i55}^{XY} & f_{i56}^{XY} \\ f_{i16}^{XY} & -f_{i15}^{XY} & f_{i36}^{XY} & f_{i35}^{XY} & f_{i56}^{XY} & f_{i55}^{XY} \end{bmatrix} \quad (2.58)$$

but

$$[f^{XY}] = \begin{bmatrix} 1 & f_0 & 0 & -f_{1R} & 0 & -f_{16}^{XY} \\ f_0 & 1 & f_{1R} & 0 & f_{16}^{XY} & 0 \\ 0 & f_{1R} & 1 & f_{2R} & \rho & f_{36}^{XY} \\ -f_{1R} & 0 & f_{2R} & 1 & f_{36}^{XY} & \rho \\ 0 & f_{16}^{XY} & \rho & f_{36}^{XY} & 1 & f_{56}^{XY} \\ -f_{16}^{XY} & 0 & f_{36}^{XY} & \rho & f_{56}^{XY} & 1 \end{bmatrix} \quad \rho = \frac{\sigma_{XY}^2}{\sigma_X \sigma_Y} \quad (2.58a)$$

The set of functions C_{ijk}^{XY} introduces in equations (2.52a) becomes f_{ijk}^{2d} , and $\{a_i, A_2\}$ are determined by taking $\{\sigma_X, \sigma_Y\} = 1$ because the variable transformations (2.57) it is equivalent to normalize by $\{\sigma_X, \sigma_Y\}$. Applying the same reasoning as paragraph 2.3.2, table 2.2 becomes in the Smith two-dimensional case, the following equation:

$$S(v, \phi) = \frac{1}{\pi} \int_{-\infty}^{\infty} \exp(-h_0^2) \left[\frac{1 - \operatorname{erfc}(h_0 + y_t v \eta)/2}{1 - \operatorname{erfc}(h_0 + y_0 v \eta)/2} \right]^{\Lambda(v)} \cdot \left[\int_0^{\infty} J(h_0, p_{0X}, \phi) dp_{0X} \right] dh_0$$

with

$$J(h_0, p_{0X}, \phi) = \exp \left[-(v - p_{0X})^2 - L \int_0^{y_t} g_S(y, h_0, p_{0X}, \phi, v) dy \right]$$

with

$$g_S = \frac{\eta}{\pi} \frac{\sqrt{a_2 a_9 - a_6^2} \exp[-C_X - v(vA_X + 2B_X)] \left[1 - e^{S_X^2} \sqrt{\pi} S_X \operatorname{erfc}(S_X) \right]}{a_9 \exp\left(\frac{B_{1X}^2}{A_{1X}} - C_{1X}\right) \left\{ \operatorname{erf}\left[\frac{A_{1X}h + B_{1X}}{\sqrt{A_{1X}}}\right] + 1 \right\}}$$

with

(2.59)

$$\left\{ \begin{array}{l} C_X = \frac{\left(a_1 h_0^2 + a_2 h^2 + 2a_3 h_0 h + 2a_5 h_0 (v - p_{0X}) - 2a_8 h (v - p_{0X}) + a_{10} (v - p_{0X})^2 \right)}{|[f^{XY}]|} \\ S_X = \frac{h_0 a_7 - h a_6 + (v - p_{0X}) a_4 + v a_9}{\sqrt{a_9 |[f^{XY}]|}} \\ v(vA_X + 2B_X) = \frac{v^2 a_9 + 2v(h_0 a_7 - h a_6) + 2v a_4 (v - p_{0X})}{|[f^{XY}]|} \\ C_{1X} = h_0^2 \cdot \frac{a_1 a_9 - a_7^2}{a_9 |[f^{XY}]|} + (v - p_{0X})^2 \\ \quad \cdot \frac{a_{10} a_9 - a_4^2}{a_9 |[f^{XY}]|} + 2h_0 (v - p_{0X}) \cdot \frac{a_5 a_9 - a_4 a_7}{a_9 |[f^{XY}]|} \\ \frac{B_{1X}}{\sqrt{A_{1X}}} = \frac{h_0 (a_3 a_9 + a_6 a_7) + (v - p_{0X}) (a_6 a_4 - a_8 a_9)}{\sqrt{a_9 |[f^{XY}]|} (a_2 a_9 - a_6^2)} \\ \sqrt{A_{1X}} = \sqrt{\frac{a_2 a_9 - a_6^2}{a_9 |[f^{XY}]|}} \end{array} \right.$$

2.5.2.6 Simulations

In the first chapter we have shown that the autocorrelation function in polar coordinates is modeled by:

$$R_0(R, \phi; u_{10}) = \omega^2 \left\{ \cos\left(\frac{R}{L_0}\right) / \left[1 + \left(\frac{R}{L_0}\right)^2 \right] - A \cos(2\phi) \cdot J_2\left(\frac{R}{L_2}\right) / \left[1 + \left(\frac{R}{L_2}\right)^2 \right] \right\} \quad (2.60)$$

In table 2.5 are given the elements of the covariance matrix (2.58a). They are obtained from equation (2.60). In figure 2.27 a_i , the deter-

Table 2.5 Parameters of the covariance matrix in polar coordinates.

R_0	$\omega^2 \left\{ \cos\left(\frac{R}{L'_0}\right) / \left[1 + \left(\frac{R}{L_0}\right)^2\right] - A \cos(2\phi) J_2\left(\frac{R}{L'_0}\right) / \left[1 + \left(\frac{R}{L_2}\right)^2\right] \right\}$
$f_0 =$ $f_{00} - f_{02} \cos(2\phi)$	$\begin{cases} f_{00} = \cos(yr_0)/(1+y^2) \\ f_{02} = AJ_2(yr_2)/[1+(yr_1)^2] \end{cases}$ with $\begin{cases} y = R/L_0 & r_0 = L_0/L'_0 \\ r_1 = L_0/L_2 & r_2 = L_0/L'_2 \end{cases}$
$f_{1R} =$ $-\frac{f_{1R0} - f_{1R2} \cos(2\phi)}{\sigma_X}$	$\begin{cases} f_{1R0} = -\frac{2y \cos(yr_0)}{(1+y^2)^2} - \frac{r_0 \sin(yr_0)}{1+y^2} \\ f_{1R2} = A \left(\frac{r_2 \left[J_1(yr_2) - \frac{2J_2(yr_2)}{yr_2} \right]}{1+(yr_1)^2} - \frac{2yr_1^2 J_2(yr_2)}{[1+(yr_1)^2]^2} \right) \end{cases}$
$f_{2R} =$ $-\frac{f_{2R0} - f_{2R2} \cos(2\phi)}{\sigma_X^2}$	$\begin{cases} f_{2R0} = \cos(yr_0) \left[\frac{8y^2}{(1+y^2)^2} - r_0^2 - \frac{2}{1+y^2} \right] \frac{1}{1+y^2} + \frac{4r_0 y \sin(yr_0)}{(1+y^2)^2} \\ f_{2R2} = A \left(\left[r_2 J_0(yr_2) - \frac{3J_1(yr_2)}{y} + \frac{6J_2(yr_2)}{r_2 y^2} \right] \frac{r_2}{1+(yr_1)^2} \right. \\ \left. - [2yr_2 J_1(yr_2) - 3J_2(yr_2)] \frac{2r_1^2}{[1+(yr_1)^2]^2} + \frac{8y^2 r_1^4 J_2(yr_2)}{[1+(yr_1)^2]^3} \right) \end{cases}$
$\{f_{16}^{XY}, f_{36}^{XY}, f_{56}^{XY}\}$	$\begin{cases} f_{16}^{XY} = \frac{2f_{02} \sin(2\phi)}{y\sigma_Y} & f_{36}^{XY} = -\frac{2 \sin(2\phi)}{y^2 \sigma_X \sigma_Y} (yf_{1R2} - f_{02}) \\ f_{56}^{XY} = -\frac{1}{\sigma_Y^2} \left[\frac{f_{1R0}}{y} + \frac{\cos(2\phi)}{y^2} (4f_{02} - yf_{1R2}) \right] \end{cases}$
$\{\sigma_X^2, \sigma_Y^2, \sigma_{XY}^2, \rho, \eta\}$	$\begin{cases} \sigma_X^2 = \alpha + \beta \cos(2\phi) \\ \sigma_Y^2 = \alpha - \beta \cos(2\phi) \\ \sigma_{XY}^2 = -\beta \sin(2\phi) \end{cases}$ with $\begin{cases} \alpha = 2 + r_0^2 & \beta = Ar_2^2/4 \\ \rho = \sigma_{XY}^2/(\sigma_X \sigma_Y) & \eta = \sigma_X \end{cases}$

minant $[[f^{XY}]]$ of the covariance matrix, are plotted as a function of $y = R/L_0$, for wind directions $\phi = \{0, 45, 90\}^\circ$.

We observe that $\{a_1, a_9, a_{10}, [[f^{XY}]]\}$ tend to one when $y \geq y_t = 6$, whereas $\{a_{i \in [3;8]}\}$ tend respectively to zero. So, when $y \geq y_t = 6$, the correlation is negligible and we obtain equation (2.53c).

Figure 2.28 summarizes the steps of the determination of the correlated shadowing function.

On the left of figure 2.29, for an infinite surface, the Smith two-dimensional correlated monostatic shadowing function for $u_f = \{40, 60\}$ cm/s is plotted as a function of the direction ϕ according to the wind direction and the parameter v . We observe that the shadowing function varies slightly with the direction ϕ , the anisotropic effect is then not very important. On the right of figure 2.29, the difference between the correlated and uncorrelated results for $u_f = \{40, 60\}$ cm/s are represented as a function of the direction ϕ and v . We note that the correlation is negligible when v becomes superior to 1.4, corresponding to an incidence angle equal to $\theta_C =$

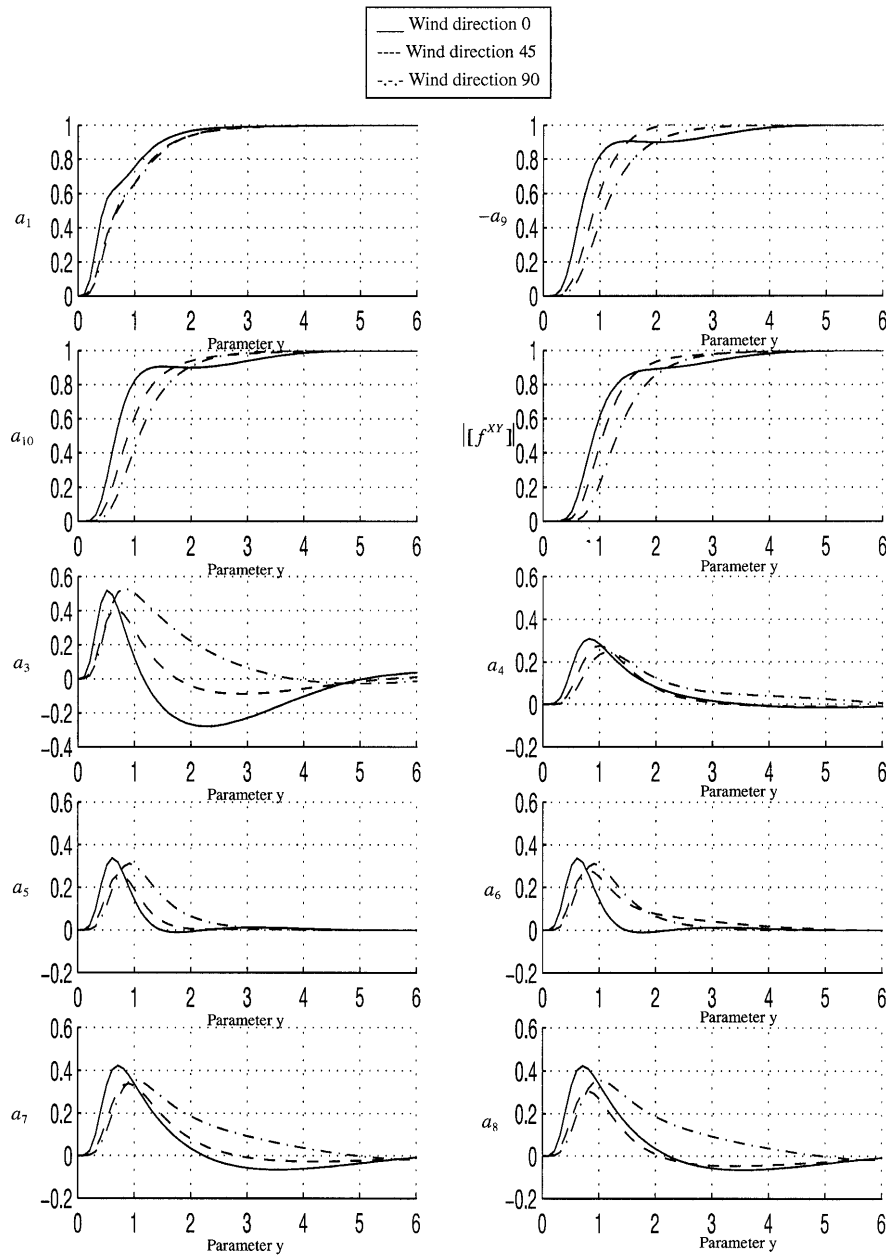


Figure 2.27 Terms $\{a_i, |[f^{XY}]|\}$ as a function of the distance y and for directions $\phi = \{0, 45, 90\}^\circ$.

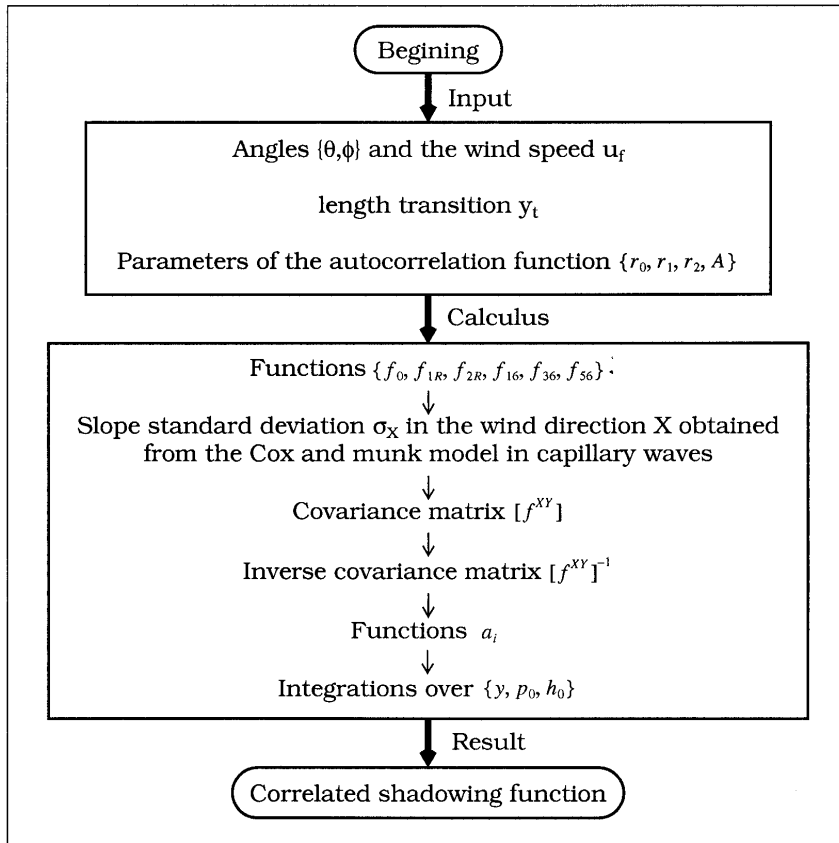


Figure 2.28 Steps for the calculus of the correlated shadowing function.

$\text{atan}[0, 5\sqrt{\alpha + \beta \cos(2\phi)}]$. As the difference becomes more greater than zero, the correlated results are superior to the uncorrelated ones, involving that the correlated shadowing function overestimates the shadow. Indeed in the one-dimensional case, we have seen that the uncorrelated shadowing function overestimated the shadow. So, the correlation must be include when the difference becomes inferior to zero. This limit is given by the curve named zero of the figure 2.29 (right). The method applied to the bistatic case is similar to the one used in paragraph 2.4.2.3.

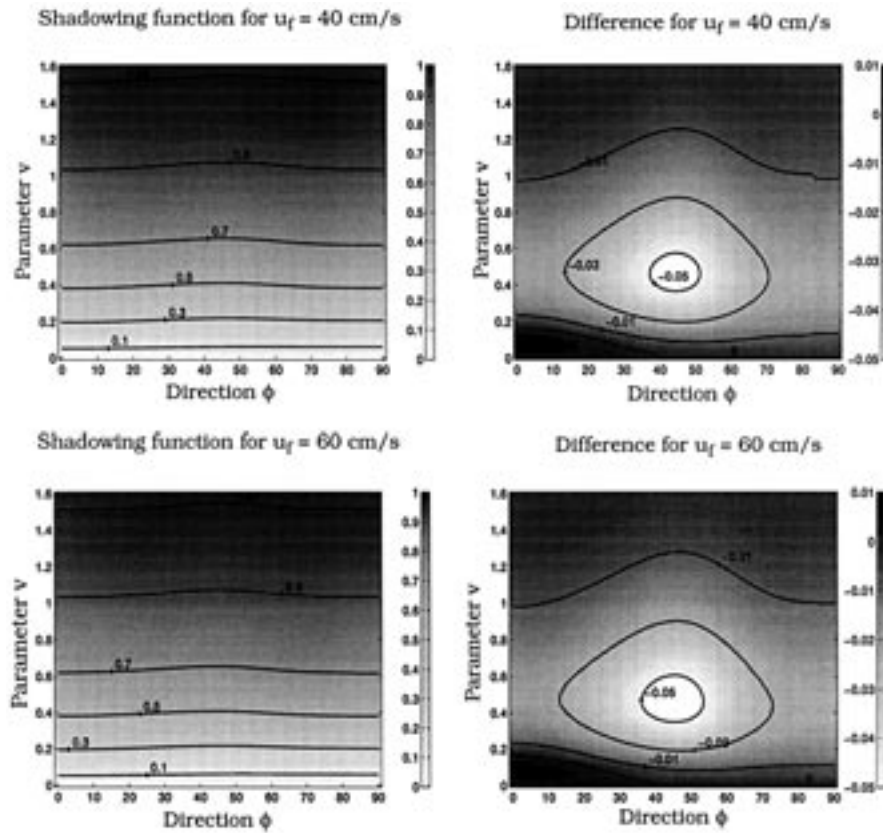


Figure 2.29 On the left, the Smith two-dimensional correlated monostatic shadowing function for $u_f = \{20, 40\}$ cm/s, as a function of the wind direction ϕ and v . On the right, the difference between the correlated and uncorrelated results for $u_f = \{20, 40\}$ cm/s, as a function of the wind direction ϕ and v .

2.5.3 Conclusion

In this part, The one-dimensional shadowing functions have been extended to the two-dimensional case. At first, we calculated the Smith uncorrelated shadowing function in polar coordinates as a function of incidence angles $\{\theta_1, \theta_2\}$, the wind directions $\{\phi_1, \phi_2\}$ and the slope standard deviation. Using the same reasoning, we determined rigorously the correlated covariance matrix in polar coordinates, and we shown the two-dimensional shadowing function is obtained from re-

sults of the one-dimensional shadowing function by replacing the new functions f_{ij}^{2d} . Moreover we have proved that the monostatic uncorrelated condition is given by $\theta < \text{atan}[0, 5\sqrt{\alpha + \beta \cos(2\phi)}] = \theta_C$. In the bistatic case its expression is $|\theta_{1,2}| < \text{atan}\{0, 505\sqrt{\alpha + \beta \cos(2\phi_{1,2})}\} = \theta_{1C,2C}$. The parameters $\{\alpha, \beta\}$ are obtained from the Cox and Munk model in capillary waves. Table 2.6 gives the maxima limit angle (with $\phi_1 = \phi_2 = 0^\circ$) θ_C when the correlation becomes negligible, and it is contained between $[60; 86]^\circ$.

Table 2.6 Limit angle of correction.

Beaufort scale	1	2	3	4	5	6	7	8	9
Friction u_f in cm/s	2	7	13	19	28	44	63	84	109
Speed u_{10} in m/s	0,4	1,7	3,6	5,6	7,8	10,8	14,0	17,3	20,9
Limit angle θ_C in $^\circ$	85	81	77	75	72	69	67	64	62

2.6 CONCLUSION

At first, the Wagner and Smith one-dimensional monostatic shadowing functions is calculated for an infinite surface with an uncorrelated gaussian process (equations (2.7)). Ricciardi and Sato give the rigorous expression of the shadowing function by Rice's infinite series of integrals (equation (2.5)). We determine analytically these series for an infinite surface with an uncorrelated gaussian process (equation (2.9)), and unfortunately the obtained result do not have a physical meaning. The Wagner formulation (equation (2.11)) obtained from the first term of the series is correct, but overestimate the shadowing function, whereas the Smith one is close to the reference solution.

In order to quantify the correlation effect, the Wagner and Smith one-dimensional monostatic shadowing functions is determined for a correlated gaussian process (table 2.2). For an infinite surface, the simulations show that for gaussian and lorentzian autocorrelation functions, the correlated results are inferior to the uncorrelated ones, but are superior to ones obtained from the reference solution. Nevertheless the Smith correlated model is very close to the reference solution. Moreover we show that the effect of the correlation is negligible when the incidence angle is inferior to $\theta_C = \text{atan}(0, 505/\sigma)$, corresponding to a shadow equal to 0.97. σ denotes the slope standard deviation. Physically, neglecting the correlation means that the shadowing func-

tion is independent of the autocorrelation function. Simulations are also presented for damped autocorrelation functions.

The Smith one-dimensional shadowing function is extended to bistatic case without and with correlation. It depends on two monostatic shadowing functions defined by the location of the emitter θ_1 , and receiver θ_2 . The simulations in the correlated case prove that the correlation is negligible when the incidence angles $\theta_{1,2}$ are inferior to $\theta_{iC} = \text{atan}(0,505/\sigma)$.

The set of one-dimensional results are generalized to the two-dimensional configurations. We show that the uncorrelated shadowing function depends on incidence angles $\{\theta_1, \theta_2\}$, slope variances $\sigma_{1,2}^2 = \alpha + \beta \cos(2\phi_{1,2})$ where $\{\phi_1, \phi_2\}$ are the observation directions according to the wind direction. The parameters $\{\alpha, \beta\}$ are given by the Cox and Munk model in capillary waves. In order to use the one-dimensional result, the covariance matrix is expressed in polar coordinates which is the main difficulty of the shadowing function calculus.

The simulations show that the correlation becomes negligible when the incidence angle is inferior to $\theta_C = \text{atan}\left(0,505\sqrt{\alpha + \beta \cos(2\phi)}\right)$. In this chapter we have considered an infinite surface for simulations, but the method may be applied on any observation length.

3. EMISSIVITY OF THE SEA SURFACE

3.1 INTRODUCTION

The intrinsic thermal radiation of a body is characterized by two quantities: its emissivity and the spectral radiance of a blackbody. A blackbody is a body which totally absorbs any incident radiation. For any material, Kirchhoff [30, 31] shows that its radiance is equal to the radiance of a blackbody which would radiate at the same temperature multiplied by a coefficient named emissivity. The mathematical expression of the blackbody radiance as a function of the temperature and wavelength is given by Planck's distribution, involving that the body at surrounding temperature radiates in the near infrared (Wien's law). On the contrary the emissivity is difficult to model, it depends on the surface parameters (temperature, roughness) and on the incident beam characteristics (wavelength, incidence angle and polarization).

The goal of this chapter is to determine the two-dimensional infrared emissivity of the sea surface. Articles [32] and [33] use a similar approach for computing emissivity. They assume that the sea surface is isotropic and the shadowing effect is not included. In [34] suppose that the surface is isotropic and the shadowing effect is quantified by an heuristic approach. Our study is based on recent works presented in [35] and [36]. These authors use a similar approach than [32] and [33] with more rigorous analysis by introducing the shadowing function. In order to use the one-dimensional shadowing function, these authors assume that the slope in the crosswind direction γ_y can be neglected with respect to the one defined in the wind direction γ_x . This means that they neglect γ_y^2 in comparison with $1 + \gamma_x^2$. This hypothesis allows them to consider a one-dimensional problem, involving that the knowledge of the two-dimensional shadowing function is not required. Moreover, they use the JONSWAP gravity spectrum (equation (1.29)) for the calculus of the slope variance, whereas we use the Cox and munk capillary model. Since our model assumes no hypothesis on the slopes, the emissivity is obtained from the two-dimensional shadowing function developed in chapter 2. Moreover the correlating effect of the shadowing function introduced in chapter 2 is also quantified.

The first paragraph of this chapter shows that the diffraction is negligible, involving that the scattered power from the sea surface is defined in the specular component, given by the geometric optic theory. The concepts of the radiometry are also presented. The determination

of the emissivity requires the knowledge of three following parameters: the probability density of the slopes assumed to be gaussian, the two-dimensional monostatic shadowing function studied in chapter 2, and the Fresnel coefficient giving the polarization information. In the second paragraph, are determined the one-dimensional and two-dimensional emissivities. In the last part, simulations are realized for different sea states and results are compared to the ones obtained in [35] and [36].

3.2 PRELIMINARIES

We show in this first part that the emitted power in the specular direction is more important than the one diffracted in the all half-space. In the second part, the quantities required for the calculus of the emissivity are introduced.

3.2.1 Diffraction by a Facet

The radiation at a point has been approximated by a plane to the facet at the point [34]. This approximation is valid only if:

$$2\pi d \cos^3(\theta_1) \gg \lambda \quad (3.1)$$

with d the radius of facet curvature at the point, λ the wavelength, and θ_1 the angle between the normal to the facet and the observation direction. Equation (3.1) involves that the ocean wave is sufficiently smooth relative to the infrared spectrum, λ is on about the order ten μm , which means that the tangent plane assumption is valid even for capillary waves. Define a facet of length a , inclined of an angle χ along the horizontal plane (figure 3.1).

The diffracted normalized intensity by the surface around the normal is defined as follows:

$$I = \frac{\sin^2(\pi u \Delta\theta)}{(\pi u \Delta\theta)^2} \quad \text{with} \quad \begin{cases} u = a/\lambda & a = \omega \sqrt{1 + \frac{1}{\sigma^2}} \\ \Delta\theta = \sin(\theta_1) - \sin(\theta_2) \end{cases} \quad (3.2)$$

where ω denotes the surface height with a slope $\sigma = \tan \chi$. The first zero of the intensity is given by $\Delta\theta_0 = 1/u$. In the infrared domain, the wavelength λ is approximatively ten μm whereas a is about one cm at minimum, thus $u \approx 10^3$. As the viewing direction is different

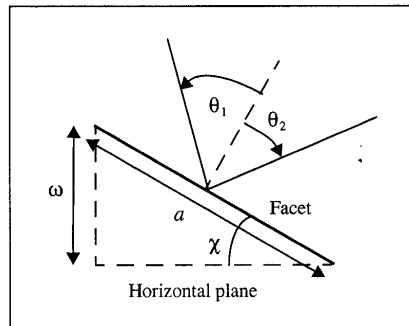


Figure 3.1 Diffracted intensity by a facet.

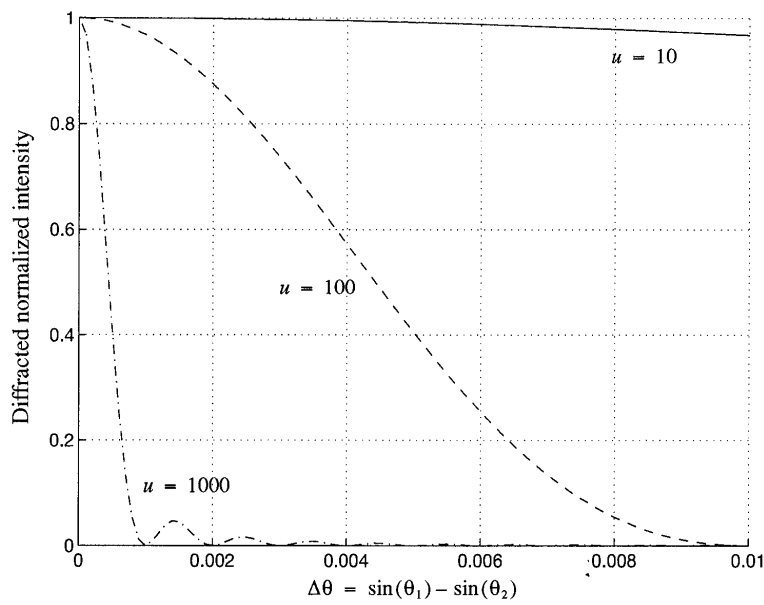


Figure 3.2 Diffracted normalized intensity by a facet.

of the specular direction (figure 3.2) involving $\Delta\theta \neq 0$, the diffracted intensity becomes null due to $\Delta\theta_0 \approx 0,06^\circ$, so the power radiated is defined in the specular direction $\theta_1 = \theta_2$ given by the geometric optic theory.

3.2.2 Definitions

The set of the magnitudes introduced in [30] and [31] are monochromatic. For a polychromatic beam we have to sum over the spectral bandwidth.

3.2.2.1 The Blackbody

A blackbody is a body which totally absorbs any received radiation. Max Planck showed that its brightness $L(\lambda, T)$ is given by:

$$L(\lambda, T) = \frac{C_1 \lambda^{-5}}{e^{\frac{C_2}{\lambda T}} - 1} \quad \text{with} \quad \begin{cases} C_1 = 1,192 \cdot 10^{-16} W \cdot m^2 \\ C_2 = 1,439 \cdot 10^{-2} m \cdot K \end{cases} \quad (3.3)$$

where T is the absolute temperature in Kelvin, and λ the wavelength in meter. In figure 3.3 the variations of the isotherm brightness are plotted. The unity is $W \cdot sr^{-1} \cdot m^{-2}$.

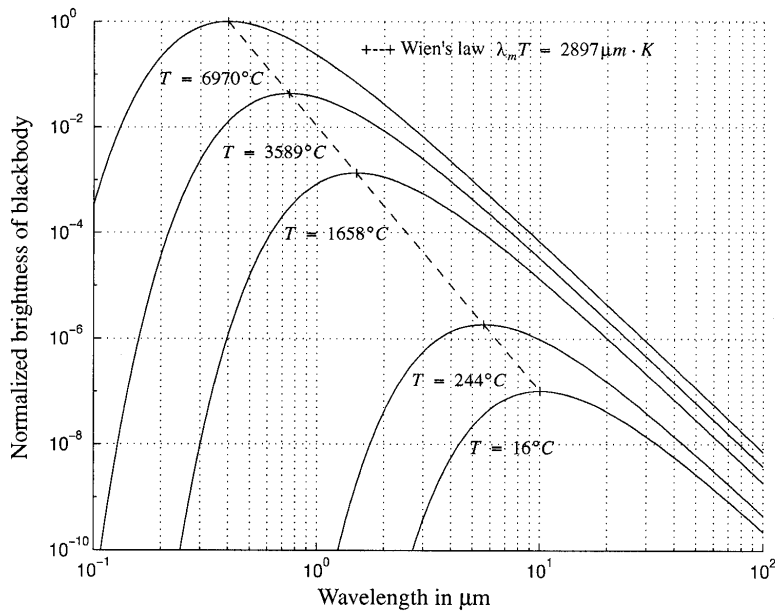


Figure 3.3 Normalized brightness of blackbody as a function of the wavelength for different temperatures.

3.2.2.2 The Wien Law

The isotherms of Planck's distribution represented in figure 3.3 reach a maximum λ_m verifying the following relation:

$$\lambda_m T = cste = 2897 \mu\text{m} \cdot \text{K} \quad (3.4)$$

Equation (3.4) named Wien's law shows that the hotter body the more its maximum shifts to a small wavelength. The electromagnetic spectrum defined between the infrared and the visible extends from 700 nm to one mm. Equation (3.4) involves that to a given wavelength corresponds a temperature (figure 3.4). We observe that between $5.6 \mu\text{m}$ and $14 \mu\text{m}$ the temperatures are defined between -66 and 244 Celsius degrees, this region is named the thermal infrared. The limit values may change according to authors.

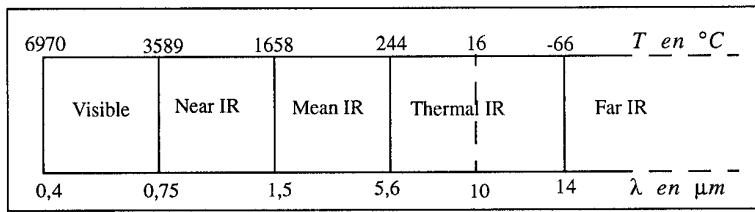


Figure 3.4 Correspondence between the wavelength and the temperature.

3.2.2.3 The Real Bodies-Emissivity

Physically a blackbody does not exist, but its theoretical model can be applied on any body. Indeed, Kirchhoff shown that for a real body, its brightness $l(\lambda, T, \theta)$ is obtained from the blackbody one $L(\lambda, T)$ radiating at the same temperature multiplied by a coefficient $\varepsilon(\lambda, T, \theta)$:

$$l(\lambda, T, \theta) = \varepsilon(\lambda, T, \theta)L(\lambda, T) \quad (3.5)$$

where $\varepsilon(\lambda, T, \theta)$ denotes the emissivity. It depends on the wavelength, on the sea state (temperature T , roughness), and on the viewing direction θ . Since it is contained between zero and one, the radiation of the real body is always inferior to a blackbody at the same temperature.

3.2.2.4 Coefficients of Reflection, Absorption and Transmission

Let ϕ_i be an incident flux arriving on the surface of a dioptré characterized by the refraction indexes $\{n_1, n_2\}$. The incident flux is decomposed in three parts (figure 3.5):

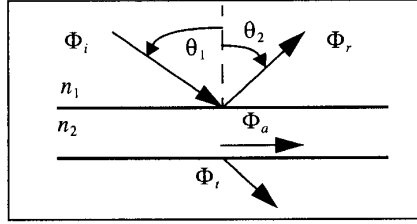


Figure 3.5 Coefficients of reflection, absorption and transmission.

where $\{\Phi_r, \Phi_a, \Phi_t\}$ respectively denote the reflected, absorbed and transmitted flux by the material of index n_2 . The conservation of the energy implies:

$$\Phi_i = \Phi_r + \Phi_a + \Phi_t \quad (3.6)$$

The reflection κ , absorption α and transmission τ power coefficients are given by:

$$\kappa = \frac{\Phi_r}{\Phi_i} \quad \alpha = \frac{\Phi_a}{\Phi_i} \quad \tau = \frac{\Phi_t}{\Phi_i} \quad (3.6a)$$

Substituting equations (3.6a) into (3.6), we obtain:

$$\kappa + \alpha + \tau = 1 \quad (3.6b)$$

The blackbody is defined by $\alpha = 1$. The thermal equilibrium conditions of a body located inside a closed enclosure involves that the emissivity of body is equal to its absorption coefficient:

$$\varepsilon = \alpha \quad (3.6c)$$

Using equations (3.6c) and (3.6b), the emissivity of an opaque ($\tau = 0$) body becomes:

$$\varepsilon = 1 - \kappa \quad (3.7)$$

This relation is used to determine the emissivity of the sea surface.

3.2.2.5 The Fresnel Reflection Coefficients

For an incidence angle θ_1 , the Fresnel reflection coefficients in vertical polarization r_v (parallel to the incidence plane) and in horizontal polarization r_H (orthogonal to the incidence plane) are given by (figure 3.5):

$$\begin{cases} r_V(\theta_1) = \frac{\tan(\theta_1 - \theta_2)}{\tan(\theta_1 + \theta_2)} = \frac{n_2 \cos \theta_1 - n_1 \cos \theta_2}{n_2 \cos \theta_1 + n_1 \cos \theta_2} \\ r_H(\theta_1) = \frac{\sin(\theta_2 - \theta_1)}{\sin(\theta_1 + \theta_2)} = \frac{n_1 \cos \theta_1 - n_2 \cos \theta_2}{n_1 \cos \theta_1 + n_2 \cos \theta_2} \end{cases} \quad (3.8)$$

The emissivity is obtained from both quantities. Since the emissivity is proportional to the power density, we must use the Fresnel reflection coefficients $\{\kappa_V, \kappa_H\}$ in power defined by:

$$\kappa_V(\theta_1) = |r_V(\theta_1)|^2 \quad \kappa_H(\theta_1) = |r_H(\theta_1)|^2 \quad (3.8a)$$

3.2.2.6 The Sea Refractive Index

The emissivity depends on the Fresnel coefficients defined from indexes n_2 sea and n_1 air. The air index is assumed equal to the unity. The goal of this part is to quantify the index n_2 as a function of the wavelength λ . Wien's law involves that the body of surrounding temperature radiate in infrared. Thermal signals may result from self-emission or incident reflections of the background. The wavelength are in the infrared range of about 0.7 to 100 μm . The attenuation of infrared radiation is frequency and temperature dependent. A number of so-called windows exist in the practical range of infrared radiation frequencies. In these windows the transmittance of the infrared radiation is high. The windows of practical interest for the infrared optronic systems are the 8 to 13 μm window, the 3 to 5 μm window and the near-infrared window (0.7 to 2 μm). Between these windows, we find absorption bands, mainly due to the presence of water vapor and carbon dioxide in the absorption. In this paper, we do not study the near infrared band. The sea refraction index is then studied in the interval from 3 to 13 μm . In figure 3.6, the real and complex parts of the index [37] are plotted as a function of the wavelength for a temperature equal to 25°C. We observe that the real part is proportional to the inverse of the wavelength, whereas for the imaginary part is the contrary. Moreover with the interval between 4 and 12 μm , the real part

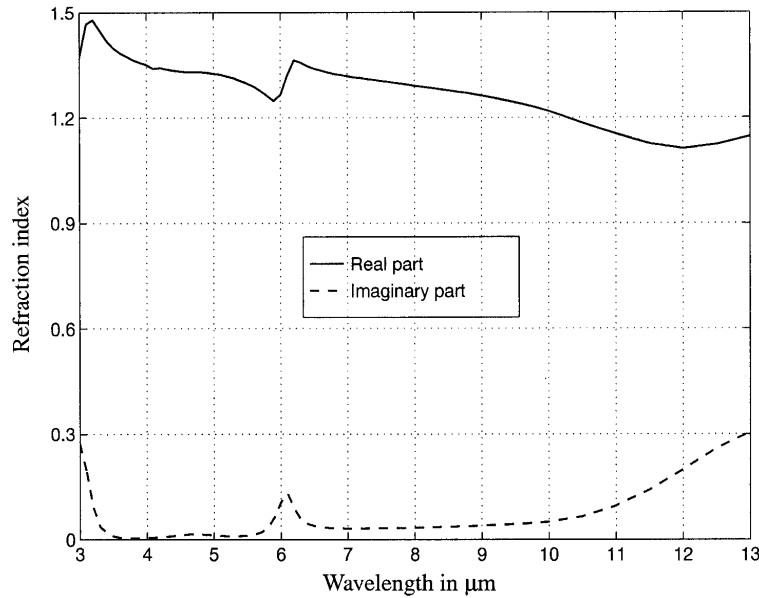


Figure 3.6 Water reflection index as a function of the wavelength for a temperature $T = 25^{\circ}\text{C}$.

is greater than the imaginary part, with respective mean values equal to 1.262 and 0.053.

3.2.3 Conclusion

The wavelength in the infrared is very inferior to the curvate radius of the sea surface, involving that the whole diffracted energy is defined in the specular direction, given by the geometric optic theory. Since for a dielectric, the emissivity is obtained from Fresnel's power coefficients, the emissivity is a function of the three following parameters: the medium index, thus of the temperature, and if the medium is dispersive of the wavelength, the incidence and reflection angles modulated by the surface roughness, the polarimetric information is contained in the Fresnel coefficients.

3.3 THE TWO-DIMENSIONAL EMISSIVITY

The goal of this paragraph is to model the two-dimensional emissivity from the parameters defined in the previous paragraph. It is calculated

in the one-dimensional and two-dimensional cases.

3.3.1 The One-Dimensional Emissivity

We have seen in paragraph 3.2.2.4 that the emissivity of the body depends on the Fresnel coefficients, which are function of the incidence angle and refraction indexes. For a given incidence, the reflection angle is modulated by the surface roughness characterized by the slope distribution. The shadowing function is also included. The goal of this section is to introduce these parameters in the calculus of the emissivity [35, 36].

3.3.1.1 Geometry of the Problem

In the cartesian coordinates (z, x) (figure 3.7), M is a surface point of height $z(x, t)$ and abscissa x at the time t . The surface is assumed to be one-dimensional involving that the component y is nil. Let \vec{n} be the unitary vector in the direction z , \vec{n}' the unitary vector normal to the surface element dS at the point M , and \vec{s} the unitary vector between the viewing direction and z . Define $\varphi = (\vec{n}', \vec{s})$.

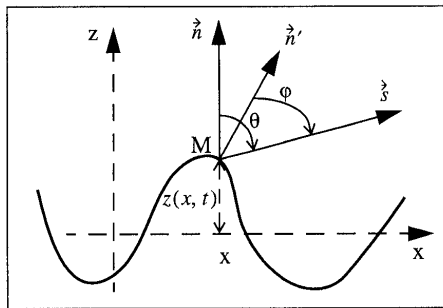


Figure 3.7 Geometry of the problem.

According to (3.7), the local emissivity ε of the facet in the direction φ is [35]:

$$\varepsilon = [1 - |r(|\varphi|)|^2] \cdot f \quad (3.9)$$

The dependences in frequency and temperature are omitted. The function f characterizes the surface statistical behavior of the local slope γ .

3.3.1.2 The Average Emissivity

The function $f = p(\gamma)S(\theta, \gamma)$ is composed of two terms. The shadowing function $S(\theta, \gamma)$, and the slope probability density $p(\gamma)$ assumed to be gaussian:

$$p(\gamma) = \frac{1}{\sqrt{2\pi}\sigma} \cdot \exp\left(-\frac{\gamma^2}{2\sigma^2}\right) \quad (3.10)$$

where σ is the slope standard deviation. f being a probability density, it has to be normalized. This function f_N is determined in the next paragraph. Moreover (figure 3.8) we have:

$$\tan \chi = \frac{\partial z}{\partial x} = \gamma \quad \text{and} \quad \varphi = \theta + \chi \quad \Rightarrow \quad \varphi = \theta + \text{atan} \gamma \quad (3.10a)$$

These equations imply that the emissivity $\varepsilon(\theta, \gamma)$ in the viewing direction θ is:

$$\varepsilon(\theta, \gamma) = [1 - |r(|\theta + \text{atan} \gamma|)|^2] f_N(\theta, \gamma) \quad (3.10b)$$

The average emissivity $\varepsilon(\theta, \gamma)$ is then given by:

$$\varepsilon(\theta) = \int_{-\infty}^{\infty} \varepsilon(\theta, \gamma) d\gamma \quad (3.11)$$

3.3.1.3 The Normalized Average Emissivity

By definition, we have:

$$f_N = f \cdot g \quad \text{and} \quad \int_{-\infty}^{\infty} f_N d\gamma = \int_{-\infty}^{\infty} f \cdot g \cdot d\gamma = 1 \quad (3.12)$$

The sum of observed surfaces S_{obs} in the Σ plane normal to the viewing direction θ is equal to the projected surface S_0 in the same plane (figure 3.8), so:

$$\int_{S_0} dS_{obs} \cos \varphi = S_0 \cos \theta \quad (3.12a)$$

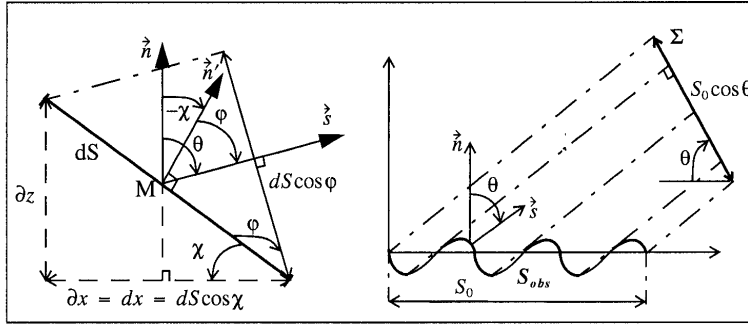


Figure 3.8 Determination of the normalized function.

moreover

$$dS_{obs} = \int_{-\infty}^{\infty} f \cdot dS \cdot d\gamma \quad (3.12b)$$

Substituting equation (3.12b) into (3.12a) we obtain:

$$\int_{S_0} dS \int_{-\infty}^{\infty} f \cdot \cos \varphi d\gamma = S_0 \cos \theta \quad (3.12c)$$

Since $dS = dx / \cos \chi$ (figure 3.7), we have:

$$\int_{S_0} dx \int_{-\infty}^{\infty} f \cdot \frac{\cos \varphi}{\cos \chi} \cdot d\gamma = S_0 \cos \theta \Rightarrow \int_{-\infty}^{\infty} f \cdot \frac{\cos \varphi}{\cos \theta \cos \chi} \cdot d\gamma = 1 \quad (3.12d)$$

Comparing equations (3.12d) with (3.12), the normalized function g is given by:

$$g(\theta, \gamma) = \frac{\cos \varphi}{\cos \theta \cos \chi} = \frac{\vec{n}' \cdot \vec{s}}{(\vec{n} \cdot \vec{n}')(\vec{n} \cdot \vec{s})} = 1 - \gamma \tan \theta \quad (3.13)$$

3.3.1.4 Conclusion

The one-dimensional emissivity for a gaussian process with a variance σ^2 is:

$$\varepsilon(\theta, \sigma) = \int_{-\infty}^{\infty} \frac{(1 - \gamma \tan \theta)[1 - |r(|\theta + \text{atan}\gamma|)|^2]}{\sqrt{2\pi\sigma}} \exp\left(-\frac{\gamma^2}{2\sigma^2}\right) S(\theta, \gamma) d\gamma \tag{3.14}$$

where r is the Fresnel reflection coefficient and S the shadowing function.

3.3.2 The Two-dimensional Emissivity

In this paragraph we determine the two-dimensional emissivity. In order to use the one-dimensional shadowing function, the authors of article [36] use an hypothesis on the slope probability density. Since our method includes the two-dimensional shadowing function established in chapter 2, we make no hypothesis on the slope distribution, it is the originality of our work.

3.3.2.1 The Problem Geometry

Let M be a point of the surface defining the origin of cartesian coordinates (x, y, z) (figure 3.9), \vec{n} the unitary vector in the direction z , \vec{n}' the unitary vector normal to the facet at M , and \vec{s} the unitary vector of the viewing direction characterized by the $\{\theta, \phi\}$ angles. These vectors are defined by:

$$\vec{n} = \begin{bmatrix} 0 \\ 0 \\ 1 \end{bmatrix} \quad \vec{n}' = \frac{1}{\sqrt{1 + \gamma_x^2 + \gamma_y^2}} \begin{bmatrix} -\gamma_x \\ -\gamma_y \\ 1 \end{bmatrix} \quad \vec{s} = \begin{bmatrix} \sin \theta \cos \phi \\ \sin \theta \sin \phi \\ \cos \theta \end{bmatrix} \tag{3.15}$$

where $\{\gamma_x, \gamma_y\}$ are the slopes of the surface in the wind and cross-wind directions. Define $\varphi = (\vec{n}', \vec{s})$.

3.3.2.2 Determination of the Emissivity

The way is similar to the one exposed in the one-dimensional case. According to equation (3.7), the local emissivity of the facet in the direction φ is given by:

$$\varepsilon = [1 - |r(|\varphi|)|^2] \cdot f_N \tag{3.16}$$

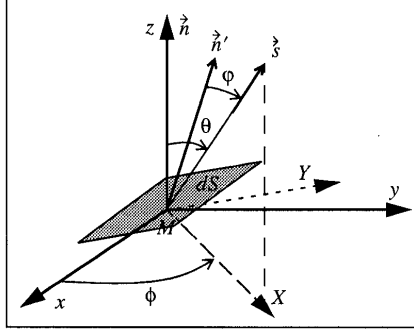


Figure 3.9 Two-dimensional configuration.

The function $f_N = p \cdot S \cdot g$ is composed of three terms. The slope probability density $p(\gamma_x, \gamma_y)$ assumed to be gaussian (equation (1.46c)):

$$p(\gamma_x, \gamma_y) = \frac{1}{2\pi\sigma_x\sigma_y} \exp\left(-\frac{\gamma_x^2}{2\sigma_x^2} - \frac{\gamma_y^2}{2\sigma_y^2}\right) \quad (3.16a)$$

The angle φ is defined by:

$$\cos \varphi = \vec{n}' \cdot \vec{s} = \frac{\cos \theta - (\gamma_x \cos \phi + \gamma_y \sin \phi) \sin \theta}{\sqrt{1 + \gamma_x^2 + \gamma_y^2}} \quad (3.16b)$$

The two-dimensional normalization function becomes:

$$g = \frac{\vec{n}' \cdot \vec{s}}{(\vec{n} \cdot \vec{n}')(\vec{n} \cdot \vec{s})} = \frac{\sqrt{1 + \gamma_x^2 + \gamma_y^2} \cos \varphi}{s_z} = \frac{\sqrt{1 + \gamma_x^2 + \gamma_y^2} \cos \varphi}{\cos \theta} \quad (3.17)$$

Substituting equation (3.16b) into (3.17) g is given by:

$$g = \frac{\cos \theta - (\gamma_x \cos \phi + \gamma_y \sin \phi) \sin \theta}{\cos \theta} = 1 - (\gamma_x \cos \phi + \gamma_y \sin \phi) \tan \theta \quad (3.17a)$$

the average emissivity $\varepsilon(\theta, \phi)$ in the directions $\{\theta, \phi\}$ is then:

$$\varepsilon(\theta, \phi) = \frac{1}{2\pi\sigma_x\sigma_y} \int_{-\infty}^{\infty} \int_{-\infty}^{\infty} [1 - r(|\varphi|)^2] \cdot \exp\left(-\frac{\gamma_x^2}{2\sigma_x^2} - \frac{\gamma_y^2}{2\sigma_y^2}\right) \cdot g \cdot S \cdot d\gamma_x d\gamma_y \quad (3.18)$$

The angle $\varphi = \varphi(\theta, \phi, \gamma_x, \gamma_y)$ and the function $g = g(\theta, \phi, \gamma_x, \gamma_y)$ are given by equations (3.16b) and (3.17a). $S = S(\theta, \phi, \gamma_x, \gamma_y)$ denotes the two-dimensional monostatic shadowing function integrated over the heights.

3.4 SIMULATIONS

In this paragraph, the two-dimensional emissivity is simulated in vertical and horizontal polarizations. Since Smith results are better than Wagner ones, we use the Smith two-dimensional shadowing function. In [36] the slope variance is determined from the JONSWAP gravity spectrum, whereas we use the Cox and Munk model (equation (1.51)), which gives the slope variance in capillary wave. The correlation of the shadowing function is also introduced, and the emissivity obtained from [36] is compared with our model.

3.4.1 Emissivity Determined with the Smith Uncorrelated Shadowing Function

3.4.1.1 Calculus

In order to calculate the shadowing function $S = S(\theta, \phi, \gamma_x, \gamma_y)$ the emissivity must be determined in the wind direction ϕ i.e., in the new base (X, Y) (figure 3.9). From the previous coordinates (γ_x, γ_y) the new coordinates (γ_X, γ_Y) are:

$$\begin{cases} \gamma_x = \gamma_X \cos \phi - \gamma_Y \sin \phi \\ \gamma_y = \gamma_X \sin \phi + \gamma_Y \cos \phi \end{cases} \quad (3.18a)$$

Substituting equations (3.18a) into (3.18) we have:

$$\begin{aligned} \varepsilon(\theta, \phi) &= \frac{1}{2\pi\sqrt{\alpha^2 - \beta^2}} \int_{-\infty}^{\infty} \int_{-\infty}^{\infty} [1 - |r(|\varphi|)|^2] \\ &\quad \cdot \exp(-a\gamma_Y^2 - 2b\gamma_Y\gamma_X - c\gamma_X^2) \cdot g \cdot S \cdot d\gamma_X d\gamma_Y \\ \text{with } \begin{cases} \cos \varphi = \frac{\cos \theta - \gamma_X \sin \theta}{\sqrt{1 + \gamma_X^2 + \gamma_Y^2}} & g = 1 - \gamma_X \tan \theta \\ a = \frac{\alpha + \beta \cos(2\phi)}{2(\alpha^2 - \beta^2)} & b = \frac{\beta \sin(2\phi)}{2(\alpha^2 - \beta^2)} & c = \frac{\alpha - \beta \cos(2\phi)}{2(\alpha^2 - \beta^2)} \end{cases} \end{aligned} \quad (3.19)$$

where $\{\alpha, \beta\}$ are defined by:

$$\alpha = (\sigma_x^2 + \sigma_y^2)/2 \quad \beta = (\sigma_x^2 - \sigma_y^2)/2 \quad (3.19a)$$

with $\{\sigma_x^2, \sigma_y^2\}$ the slope variances in the wind and crosswind directions. For an infinite sea surface, we have shown that the Smith averaged uncorrelated two-dimensional monostatic shadowing function over the height is the following (equation (2.41a)):

$$S_S(\theta, \phi, \gamma_X) = \frac{\Upsilon(\mu - \gamma_X)}{\Lambda + 1} \quad \text{with} \quad \begin{cases} v = \frac{\mu}{\sqrt{2}\sigma} = \frac{\cot \theta}{\sqrt{2[\alpha + \beta \cos(2\phi)]}} \\ \Lambda = [e^{-v^2} - v\sqrt{\pi}\text{erfc}(v)] / (2v\sqrt{\pi}) \end{cases} \quad (3.20)$$

Since the shadowing function is not integrated over the slopes, the term $1 - \text{erfc}(v)/2$ is not taken into account. Substituting equation (3.20) into (3.19), the emissivity is equal to:

$$\varepsilon(\theta, \phi) = \frac{1}{2\pi(\Lambda + 1)\sqrt{\alpha^2 - \beta^2}} \int_{-\infty}^{\mu} e^{-c\gamma_X^2} \cdot (1 - \gamma_X \tan \theta) \cdot \left\{ \int_{-\infty}^{\infty} [1 - |r(|\varphi|)|^2] \cdot e^{-a\gamma_Y^2 - 2b\gamma_Y\gamma_X} \cdot d\gamma_Y \right\} d\gamma_X \quad (3.21)$$

in order to make the double integrations we set:

$$v_X = \sqrt{c}\gamma_X \quad v_Y = \sqrt{a}\gamma_Y \quad (3.21a)$$

thus:

$$\varepsilon(\theta, \phi) = \varepsilon_0 \int_{-\infty}^{\mu\sqrt{c}} e^{-v_X^2} \cdot \left(1 - \frac{v_X}{\sqrt{c}} \tan \theta\right) \cdot \left\{ \int_{-\infty}^{\infty} [1 - |r(|\varphi|)|^2] \cdot e^{-v_Y^2 - \frac{2\beta \sin(2\phi)}{\sqrt{\alpha^2 - \beta^2 \cos^2(2\phi)}} v_X v_Y} \cdot dv_Y \right\} dv_X$$

with $\varepsilon_0 = \frac{1}{\pi(\Lambda + 1)} \sqrt{\frac{\alpha^2 - \beta^2}{\alpha^2 - \beta^2 \cos^2(2\phi)}}$ $\varphi = \text{acos} \left(\frac{\cos \theta - \frac{v_X}{\sqrt{c}} \sin \theta}{\sqrt{1 + \frac{v_X^2}{c} + \frac{v_Y^2}{a}}} \right)$ (3.22)

3.4.1.2 Particular Cases

When the incidence angle θ is equal to zero i.e., $\{v, \mu\} \rightarrow \infty$, equation (3.22) becomes:

$$\begin{aligned} \varepsilon(0, \phi) = & \frac{1}{\pi} \sqrt{\frac{\alpha^2 - \beta^2}{\alpha^2 - \beta^2 \cos^2(2\phi)}} \int_{-\infty}^{\infty} e^{-v_X^2} \\ & \cdot \left\{ \int_{-\infty}^{\infty} [1 - |r(|\varphi|)|^2] \cdot e^{-v_Y^2 - \frac{2\beta \sin(2\phi)}{\sqrt{\alpha^2 - \beta^2 \cos^2(2\phi)}} v_X v_Y} \cdot dv_Y \right\} dv_X \end{aligned} \quad (3.22a)$$

Assuming that $\cos \varphi \approx 1$ (equation (3.19) with $\theta = 0$ and $\gamma_X^2 + \gamma_Y^2 \ll 1$), we have:

$$\begin{aligned} \varepsilon(0, \phi) = & \frac{1 - |r(0)|^2}{\pi} \sqrt{\frac{\alpha^2 - \beta^2}{\alpha^2 - \beta^2 \cos^2(2\phi)}} \int_{-\infty}^{\infty} e^{-v_X^2} \\ & \cdot \left\{ \int_{-\infty}^{\infty} e^{-v_Y^2 - \frac{2\beta \sin(2\phi)}{\sqrt{\alpha^2 - \beta^2 \cos^2(2\phi)}} v_X v_Y} \cdot dv_Y \right\} dv_X \\ = & 1 - |r(0)|^2 \end{aligned} \quad (3.22b)$$

We obtain the emissivity of the plane surface. When the incidence angle θ is equal to 90° i.e., $\{v, \mu\} \rightarrow 0$, equation (3.22) becomes:

$$\begin{aligned} \varepsilon(90, \phi) = & \frac{2(\alpha^2 - \beta^2)}{\sqrt{\pi}[\alpha^2 - \beta^2 \cos^2(2\phi)]} \int_0^{\infty} v_X e^{-v_X^2} \\ & \cdot \left\{ \int_{-\infty}^{\infty} [1 - |r(|\varphi|)|^2] \cdot e^{-v_Y^2 - \frac{2\beta \sin(2\phi)}{\sqrt{\alpha^2 - \beta^2 \cos^2(2\phi)}} v_X v_Y} \cdot dv_Y \right\} dv_X \end{aligned} \quad (3.22c)$$

3.4.1.3 Simulations of the Emissivity

In figure 3.10, the vertical $\overline{\varepsilon_V}$ and horizontal $\overline{\varepsilon_H}$ integrated emissivities over the wavelength are plotted as a function of the angles $\{\phi, \theta\}$, for different friction speeds $u_f = \{20, 40, 60\}$ cm/s. $\{\overline{\varepsilon_V}, \overline{\varepsilon_H}\}$ are obtained from equation (3.22) with $|r(|\varphi|)|^2 = \{|r_V(|\varphi|)|^2, |r_H(|\varphi|)|^2\}$ where $\{r_V, r_H\}$ denote the Fresnel coefficients.

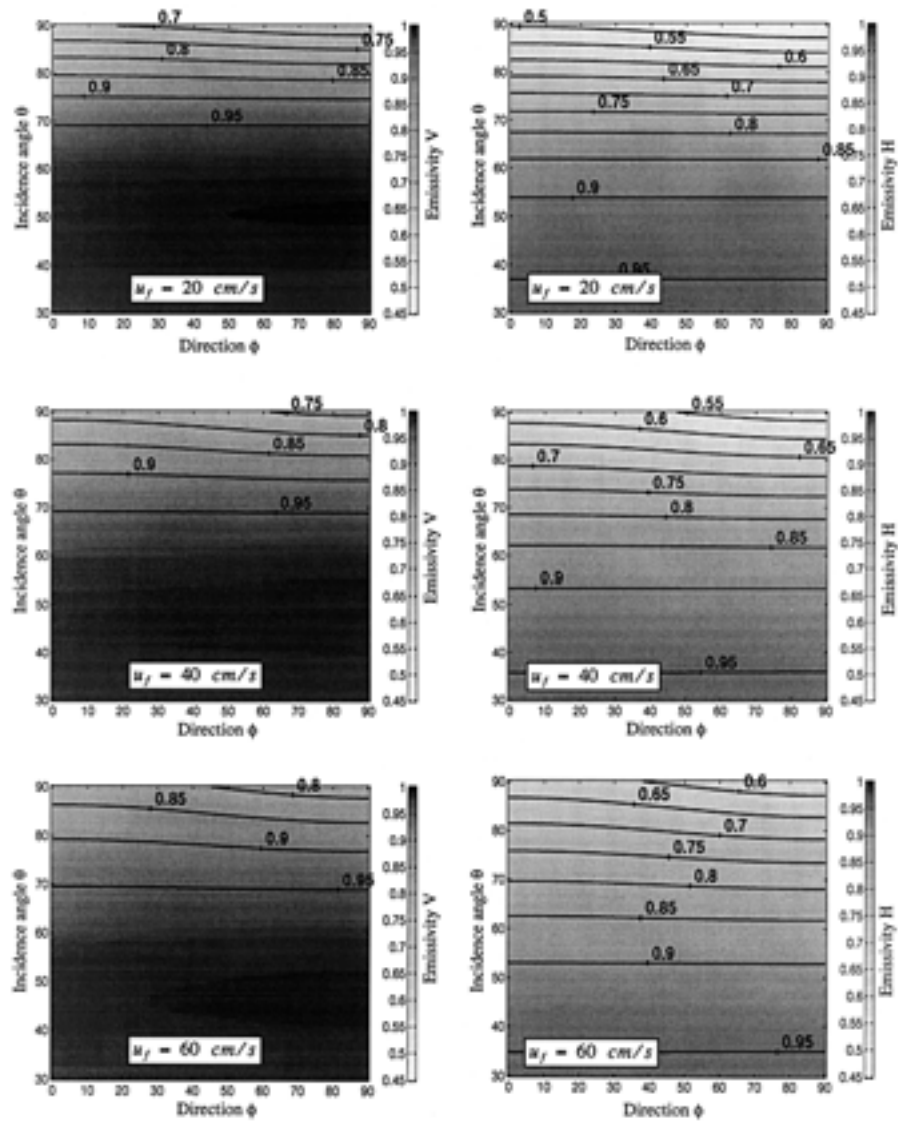


Figure 3.10 On the left and right the vertical V and horizontal H uncorrelated integrated emissivities over $\lambda \in [3; 5] \mu\text{m}$ as a function of the angles $\{\phi, \theta\}$ for different friction speeds $u_f = \{20, 40, 60\} \text{ cm/s}$ with $T = 25^\circ\text{C}$.

The emissivities are integrated over the interval $[3;5] \mu\text{m}$ with an integration step equal to $0.2 \mu\text{m}$, and the water index n_2 is defined from paragraph 3.2.2.6 at the temperature $T = 25^\circ\text{C}$.

We observe that the emissivities decrease when the angles $\{\phi, \theta\}$ tend to 90° , and their variations is very slight with the wind direction ϕ , involving that the emissivity is weakly sensitive to the anisotropic of the sea surface.

For a normal incidence $\theta = 0$, the emissivities are sensitively equal (table 3.1) to the ones obtained from the plane surface:

$$\begin{aligned} \overline{\varepsilon_V}(0,0) &\approx \overline{\varepsilon_H}(0,0) \approx 1 - \overline{|r_V(0)|^2} \approx 1 - \overline{|r_H(0)|^2} \\ &= \frac{4n_1n_2}{(n_2 + n_1)^2} = \frac{4n_2}{(n_2 + 1)^2} = 0.975 \end{aligned} \tag{3.22d}$$

where the operator $\overline{}$ denotes the mean value over the wavelength. As the friction speed increases the emissivities increases, and we note that in vertical V polarization the gap $\Delta\overline{\varepsilon_V}$ is smaller than the one $\Delta\overline{\varepsilon_H}$ obtained from a horizontal polarization H (table 3.1), and the amplitudes of $\{\Delta\overline{\varepsilon_V}, \Delta\overline{\varepsilon_H}\}$ are inversely proportional to the wind speed. Moreover, at neighborhood of the mean Brewster angle defined by $\overline{\theta_B} = \text{atan}(|\overline{n_2}|/n_1) \approx 54^\circ$, the emissivity V increases weakly.

Table 3.1 Particular values of the emissivity.

	$\lambda \in [3; 5] \mu\text{m}$			$\lambda \in [8; 12] \mu\text{m}$		
	$\overline{\varepsilon}_i(0,0)$	$\overline{\varepsilon}_i(90,90)$	$\Delta\overline{\varepsilon}_i$	$\overline{\varepsilon}_i(0,0)$	$\overline{\varepsilon}_i(90,90)$	$\Delta\overline{\varepsilon}_i$
$u_f = 20 \text{ cm/s}$	$V : 0.996$ $H : 0.973$	$V : 0.666$ $H : 0.456$	$V : 0.330$ $H : 0.517$	$V : 0.998$ $H : 0.988$	$V : 0.672$ $H : 0.533$	$V : 0.326$ $H : 0.455$
$u_f = 40 \text{ cm/s}$	$V : 0.994$ $H : 0.972$	$V : 0.739$ $H : 0.527$	$V : 0.255$ $H : 0.445$	$V : 0.997$ $H : 0.987$	$V : 0.744$ $H : 0.606$	$V : 0.253$ $H : 0.381$
$u_f = 60 \text{ cm/s}$	$V : 0.993$ $H : 0.971$	$V : 0.776$ $H : 0.567$	$V : 0.216$ $H : 0.404$	$V : 0.996$ $H : 0.987$	$V : 0.780$ $H : 0.646$	$V : 0.216$ $H : 0.341$

In figure 3.11, are plotted curves similar to the ones of figure 3.10, but the emissivities are integrated over the interval $[8;12] \mu\text{m}$. Since the mean index $\overline{n_2}|_{\lambda \in [8;12]}$ equal to 1.21 is smaller than $\overline{n_2}|_{\lambda \in [3;5]}$ equal to 1.37, the emissivities of figure 3.11 are greater than the ones obtained for the case where the integration interval is $[3;5] \mu\text{m}$ (table 3.1).

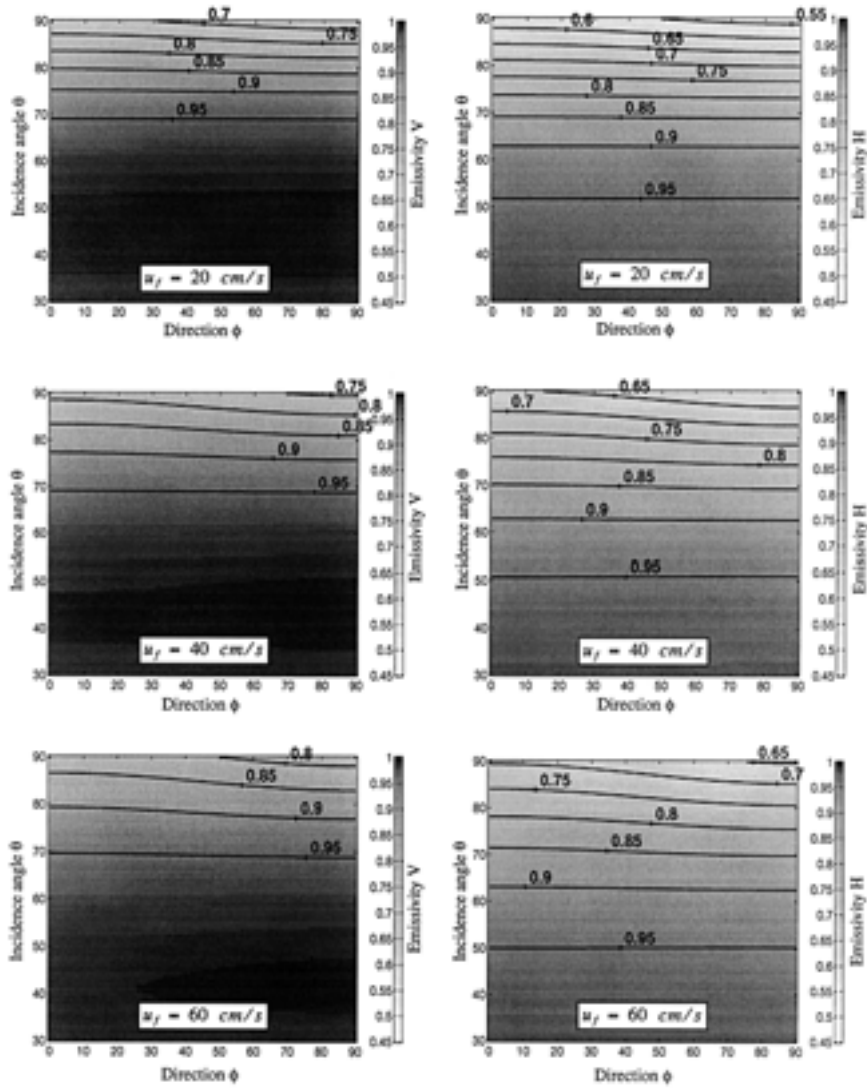


Figure 3.11 On the left and right the vertical V and horizontal H uncorrelated integrated emissivities over $\lambda \in [8; 12] \mu\text{m}$ as a function of the angles $\{\phi, \theta\}$ for different friction speeds $u_f = \{20, 40, 60\} \text{ cm/s}$ with $T = 25^\circ\text{C}$.

3.4.1.4 Simulations of the Infrared Temperature

From Kirchhoff's equation (3.5), the temperature T_a is defined by:

$$L(T_a) = \varepsilon \cdot L(T) \quad \text{with} \quad L(T) = \frac{C_1 \lambda^{-5}}{e^{\frac{C_2}{\lambda T}} - 1} \quad (3.23)$$

where L denotes the blackbody brightness (equation (3.3)), T the medium temperature in Kelvin, and λ the wavelength. So:

$$T_a = \frac{C_2}{\lambda} \frac{1}{\ln \left[\left(e^{\frac{C_2}{\lambda T}} - 1 + \varepsilon \right) / \varepsilon \right]} \quad (3.23a)$$

In figure 3.12, are plotted the uncorrelated temperatures integrated $\{\overline{T_{aV}}, \overline{T_{aH}}\}$ over $\lambda \in [3; 5] \mu\text{m}$ and $\lambda \in [8; 12] \mu\text{m}$ (measured by the infrared camera) defined in the vertical V and horizontal H planes, as a function of the angles $\{\phi, \theta\}$, and for $u_f = \{40, 60\} \text{ cm/s}$ with $T = 25^\circ\text{C}$. As the incidence angle θ and the wind speed decrease, the temperature rises. The variations $\Delta \overline{T_{aH}}$ of the temperature T_{aH} are more important than the ones $\Delta \overline{T_{aV}}$ of T_{aV} (table 3.2), involving that the horizontal component H is more sensitive to a variation of the emissivity.

Table 3.2 Particular values of the temperature.

	$\lambda \in [3; 5] \mu\text{m}$			$\lambda \in [8; 12] \mu\text{m}$		
	$\overline{T_{api}}(0, 0)$	$\overline{T_{api}}(90, 90)$	$\Delta \overline{T_{api}}$	$\overline{T_{api}}(0, 0)$	$\overline{T_{api}}(90, 90)$	$\Delta \overline{T_{api}}$
$u_f = 40 \text{ cm/s}$	V : 24.9 H : 24.0	V : 17.7 H : 10.1	V : 7.2 H : 13.9	V : 24.8 H : 23.8	V : 16.9 H : -2.7	V : 7.9 H : 26.5
$u_f = 60 \text{ cm/s}$	V : 24.8 H : 23.9	V : 18.9 H : 11.8	V : 5.9 H : 12.1	V : 24.7 H : 23.8	V : 14.3 H : 0.6	V : 10.4 H : 23.2

According to table 3.1 and table 3.2, a small variation of the emissivity $\Delta \overline{\varepsilon}_i$ can involve an important variation of the temperature $\Delta \overline{T_{ai}}$, as show in figure 3.13, where is plotted the average $\Delta \overline{T_a} / \Delta \varepsilon$ as a function of the emissivity for $\lambda \in [3; 5] \mu\text{m}$ and $\lambda \in [8; 12] \mu\text{m}$. $\Delta \overline{T_a} / \Delta \varepsilon$ is given by:

$$\frac{\Delta \overline{T_a}}{\Delta \varepsilon} \approx \frac{dT_a}{d\varepsilon} = \frac{C_2 \left(e^{\frac{C_2}{\lambda T}} - 1 \right)}{\varepsilon \lambda \ln \left(\frac{e^{\frac{C_2}{\lambda T}} - 1 + \varepsilon}{\varepsilon} \right)^2 \left(e^{\frac{C_2}{\lambda T}} - 1 + \varepsilon \right)} \quad (3.23b)$$

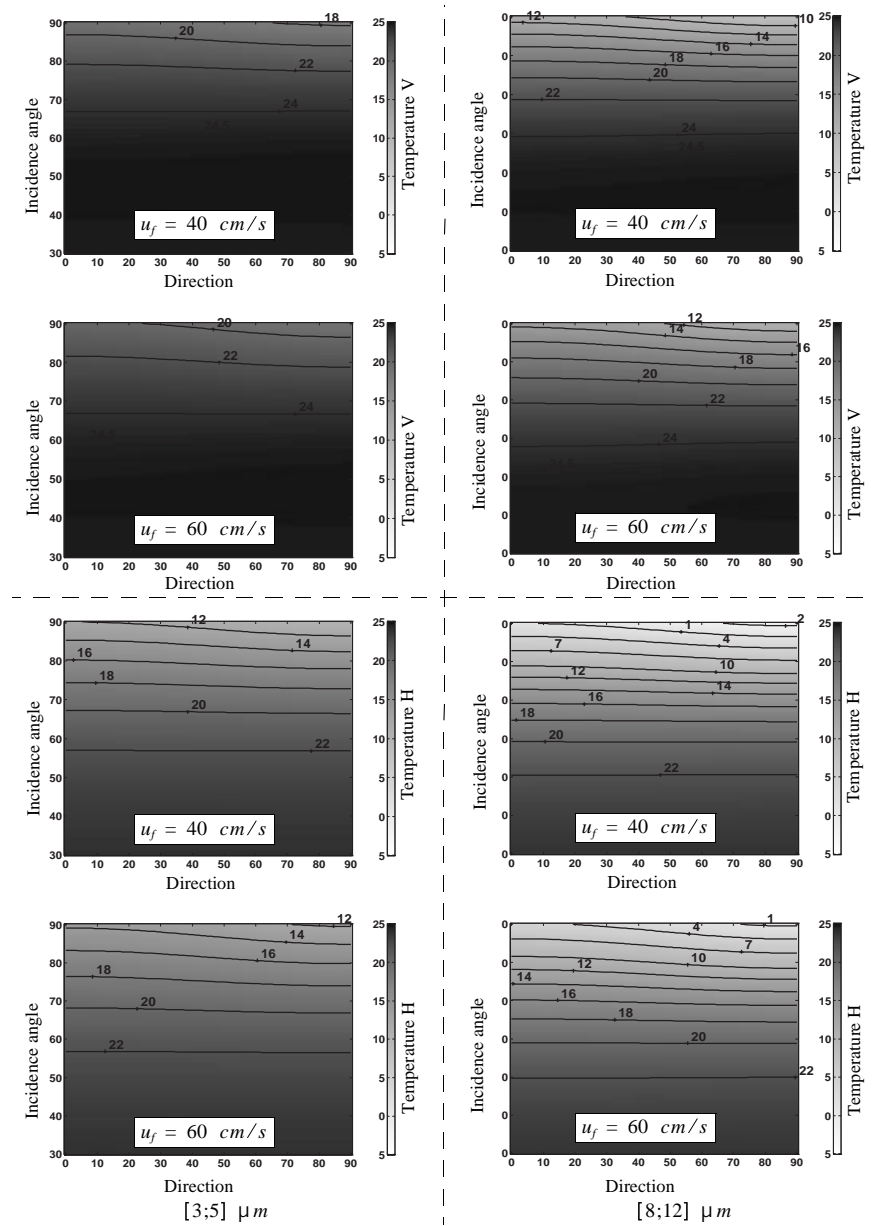


Figure 3.12 The vertical V and horizontal H uncorrelated integrated temperatures over $\lambda \in [3; 5] \mu m$ and $\lambda \in [8; 12] \mu m$ as a function of the angles $\{\phi, \theta\}$ for different friction speeds $u_f = \{40, 60\} \text{ cm/s}$ with $T = 25^\circ C$.

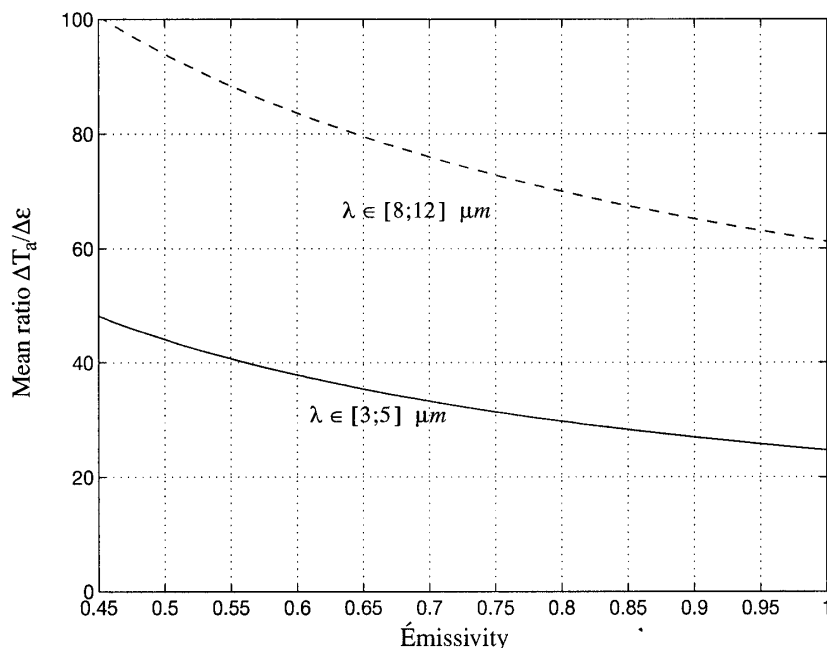


Figure 3.13 Mean ratio $\overline{\Delta T_a/\Delta \varepsilon}$ as a function of the emissivity for $\lambda \in [3; 5] \mu m$ and $\lambda \in [8; 12] \mu m$.

Since the ratio $\Delta T_a/\Delta \varepsilon$ is inversely proportional to the wavelength, the variation of the temperature $\overline{\Delta T_a}$ is more important for $\lambda \in [8; 12] \mu m$, it is equal to 76, whereas for $\lambda \in [3; 5] \mu m$ is approximately equal to 34.

In figure 3.14, the mean emissivities $[\varepsilon_V(\theta, \phi) + \varepsilon_H(\theta, \phi)]/2$ determined for $\phi = \{0, 90\}^\circ$ and $\theta = \{60, 85\}$ are compared with those obtained in [36], as a function of the wind speed u_{10} defined at ten meters above the sea. The refractive index of the water is equal to 1.19. There are two differences between their model and ours. Firstly we make no hypothesis over the slopes variance, whereas they neglect γ_y^2 in comparison with $1 + \gamma_x^2$. This hypothesis allows them to consider a one-dimensional problem, and involves that the knowledge of the two-dimensional shadowing function is not required. The second difference remains in the fact that they use the slope variances obtained from the JONSWAP gravity spectrum, whereas we use the Cox and munk capillary model.

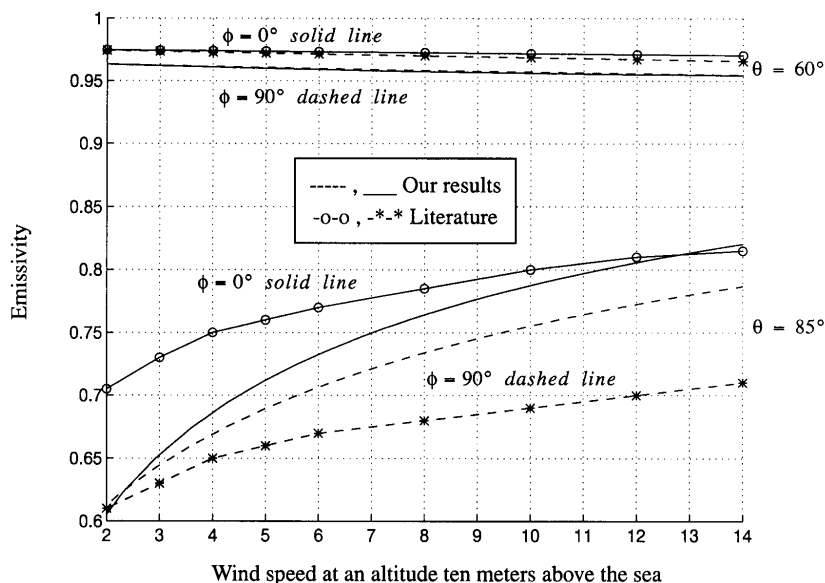


Figure 3.14 Comparison of our results with those obtained in literature.

3.4.2 Emissivity Determined with the Smith Correlated Shadowing Function

In Chapter 2, we have determined the Smith correlated two-dimensional monostatic shadowing functions. The goal of this part is to introduce this quantity in the emissivity formulation and to compare it with results obtained without correlation.

3.4.2.1 Calculus

In this case, for an infinite surface, we have shown that the Smith uncorrelated two-dimensional monostatic shadowing functions is given by:

$$S_S(\theta, \phi, \gamma_X) = \frac{\Upsilon(\mu - \gamma_X)}{\sqrt{\pi}} \int_{-\infty}^{\infty} \left[1 - \frac{\operatorname{erfc}(h_0 + y_t \sqrt{2v})}{2} \right]^\Lambda \cdot \exp \left[-h_0^2 - L \int_0^{y_t} g_S(y, h_0, p_0, v) dy \right] dh_0 \quad (3.24)$$

where $Lg_s dy$ is the two-dimensional conditional probability containing the information on the autocorrelation function defined in (2.59) of chapter 2. The limit y_t , is obtained when the correlation is negligible. In this case it is equal to 6.

h_0 corresponds to the integration over the height. The variable p_0 (equation (2.18a)) is defined by:

$$p_0 = v - \frac{\gamma_0}{\sqrt{2}\sigma} = v - \frac{\gamma_x}{\sqrt{2}\sigma} = v - \gamma_X \sqrt{c} = v - v_X \quad (3.24a)$$

Substituting equation (3.24) into (3.19) and making the variable transformations of (3.21a), we show:

$$\begin{aligned} \varepsilon(\theta, \phi) &= \frac{1}{\pi\sqrt{\pi}} \sqrt{\frac{\alpha^2 - \beta^2}{\alpha^2 - \beta^2 \cos^2(2\phi)}} \\ &\times \int_{-\infty}^{\mu\sqrt{c}} \left\{ \int_{-\infty}^{\infty} [1 - |r(|\varphi|)^2] e^{-v_X^2 - v_Y^2 - \frac{2\beta \sin(2\phi)}{\sqrt{\alpha^2 - \beta^2 \cos^2(2\phi)}} v_X v_Y} \right. \\ &\cdot \left. \left(1 - \frac{v_X}{\sqrt{c}} \tan \theta\right) \left[\int_{-\infty}^{\infty} I(h_0) J(h_0, v_X) dh_0 \right] dv_Y \right\} dv_X \quad (3.25) \end{aligned}$$

with

$$\begin{aligned} I(h_0) &= e^{-h_0^2} \left[1 - \frac{\operatorname{erfc}(h_0 + y_t \sqrt{2}v)}{2} \right]^\Lambda \\ J(h_0, v_X) &= \exp \left[-L \int_0^{y_t} g_S(y, h_0, v_X, v) dy \right] \end{aligned} \quad (3.25a)$$

The determination of the two-dimensional correlated emissivity requires four integrations over $\{y, v_X, h_0, v_Y\}$.

3.4.2.2 Notice

The correlation is negligible when $\{y_t = 0\}$ involving that:

$$I(h_0) = e^{-h_0^2} [1 - \operatorname{erfc}(h_0)/2]^\Lambda \quad J(h_0, v_X) = 1 \quad (3.26)$$

The function $J(h_0, v_X)$ becomes independent of $\{h_0, v_X\}$, the integration of $I(h_0)$ gives then:

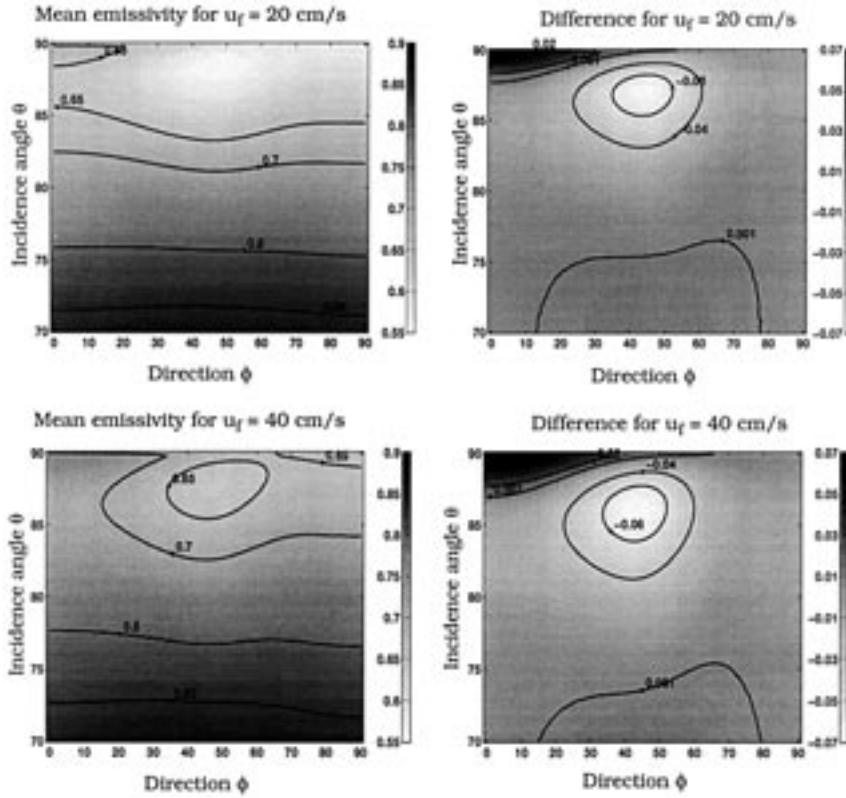


Figure 3.15 On the left, the mean emissivity $(\varepsilon_V + \varepsilon_H)/2$ as a function of the wind direction ϕ and the incidence angle θ for $u_f = \{20, 40\}$ cm/s and $\lambda = 4 \mu\text{m}$. On the right the difference between the correlated and uncorrelated emissivities as a function of the wind direction ϕ and the incidence angle θ for $u_f = \{20, 40\}$ cm/s and $\lambda = 4 \mu\text{m}$.

$$\int_{-\infty}^{\infty} I(h_0) dh_0 = \frac{\sqrt{\pi}}{\Lambda + 1} \quad (3.26a)$$

Substituting equation (3.26a) into (3.25), the expression (3.25) becomes equal to (3.22).

3.4.2.3 Simulations

In figure 3.15 the mean emissivity $(\varepsilon_V + \varepsilon_H)/2$ and the difference between the correlated and uncorrelated mean emissivities are plotted

as a function of the wind direction ϕ and the incidence angle θ for $u_f = \{20, 40\}$ cm/s and $\lambda = 4 \mu\text{m}$. We observe an enhancement of the emissivity for the grazing angles due to the fact that the shadow is overestimated involving an increasing of the emissivity. The correlation becomes negligible according the Table 2.6 when the incidence angle $\theta < 75^\circ$ for $u_f = 20$ cm/s and $\theta < 70^\circ$ for $u_f = 40$ cm/s. So, the correlation involves an emissivity's discontinuity, which physically is not observed. This phenomenon depends on the choice of the autocorrelation function.

3.5 CONCLUSION

In this chapter the two-dimensional emissivity is rigorously determined for a gaussian process, and depends on the following parameters. The incidence angle θ , and the angle ϕ between the viewing and the wind directions. The slope variances $\{\sigma_x^2, \sigma_y^2\}$ defined in the wind and crosswind directions. The Fresnel coefficients $\{r_V, r_H\}$ depending on the polarization and the medium index n_2 function of the temperature T and the wavelength. Due to the atmospheric absorption, the infrared wavelength are studied over the intervals $[3; 5] \mu\text{m}$ and $[8; 12] \mu\text{m}$, where the refraction index of the water varies between from 1.1 to 1.5, and its imaginary part is very small.

For an infinite surface, the simulations show that the uncorrelated emissivity increases with the wind speed and the wavelength, whereas it decreases with the incidence angle. Moreover it varies slightly with the wind direction and is more important in the H plane orthogonal to the incidence plane. Article [36] assumes that the slope variance in the wind direction is very superior to the one defined in the crosswind direction, which implies that the problem becomes one-dimensional. Moreover These authors use the slope variances are obtained from the JONSWAP gravity spectrum, whereas we take the Cox and Munk capillary model.

Figure 3.14 compares our emissivity model and the [36] one. We also compare the correlated and uncorrelated emissivities obtained from the Smith monostatic two-dimensional shadowing function, and we observe that the correlation has not physical meaning for grazing angles due to an overestimation of the correlated shadowing function. For simulations we have chosen an infinite surface, but our method may be applied on a finite observation area.

Epilogue

The two-dimensional spatial autocorrelation function of the heights has been modeled in polar coordinates as a function of the wind direction ϕ and the distance R between two points located on the surface. According to the wind direction ϕ , the fact that sea spectrum is even in the upwind and crosswind directions involves that the autocorrelation depends on $\cos(2\phi)$. In the Elfouhaily spectrum formulation which is the most recent in literature, the isotropic part of the autocorrelation function is modeled by a damped lorentzian, whereas the anisotropic part is represented from a Bessel function (second order and first kind) multiplied by a lorentzian. Both functions depend on parameters linked to the wind speed u_{10} defined ten meters above the sea. The correlation length is approximately proportional to the square of u_{10} and the height variance is proportional to the fourth power of u_{10} . With the Pierson and Apel spectra we obtain the same results, but the parameters vary slightly. Slopes computed from the Elfouhaily spectrum are similar to the ones obtained from the Cox and Munk model. Unlike the Pierson and Apel spectra, slopes are overestimated due to an inaccuracy of their spectrum in the capillary zone.

In order to quantify the hypothesis introduced by Wagner's and Smith's one-dimensional shadowing functions, we compute the shadowing function with correlation. It then depends on the autocorrelation function, moreover we have considered a finite observation length. We compare the correlated and the uncorrelated results for a damped lorentzian and damped gaussian autocorrelation functions, with the exact solution obtained from generating an infinite surface. The results show that the correlation is negligible when the incidence angle is inferior to $\theta_c = \text{atan}(0.5/\sigma)$, where σ is the slope standard deviation, and the correlation improves the shadow. The Smith one-dimensional function is extended to bistatic case with and without correlation. The set of one-dimensional results are generalized to the two-dimensional surface. We show that in the monostatic case, the shadowing function depends on the incidence angle θ and the slope variance $\sigma^2(\phi) = \alpha + \alpha \cos(2\phi)$ in the direction ϕ , where $\{\alpha, \beta\}$ depend on the wind speed. For the bistatic case, the shadowing function depends on θ_i and $\sigma^2(\phi_i) = \alpha + \beta \cos(2\phi_i)$. $i = 1$ corresponds to the emitter location and $i = 2$ characterizes the receiver location. Results obtained from the two-dimensional autocorrelation function modeled

in the first chapter, show that the correlation is negligible when the incidence angle is inferior to $\theta_c = \text{atan}[0.5/\sigma(\phi)]$, and for grazing angles, correlation then overestimates shadow.

For the emissivity, we compare our model with [36] which assumes that the slope variance in the upwind direction is greater than the one defined in the crosswind direction, and allows to the use of the one-dimensional shadowing function. Results are plotted in figure 3.14. We also compare the correlated and uncorrelated emissivities obtained from the Smith two-dimensional shadowing functions. We observe that the correlation overestimates the emissivity at grazing angles because the correlated shadowing function is overestimated. The set of the uncorrelated simulations assumes that the observed surface is infinite, but our method may be applied on a finite observed surface.

APPENDIX 1. THE WAGNER AND SMITH SHADOWING FUNCTIONS OF THE UNCORRELATED PROCESS FOR AN INFINITE SURFACE

In this appendix, the Wagner and Smith shadowing functions are determined for an uncorrelated process, and for an infinite observation length (equation (2.6)):

$$S(\theta) = \int_{-\infty}^{\infty} \int_{-\infty}^{\mu} p(\xi_0, \gamma_0) \exp\left(-\int_0^{\infty} g(\tau|F, \theta) d\tau\right) d\xi_0 d\gamma_0 \quad (\text{A1.1})$$

A1.1 Wagner

The Wagner conditional probability is given by (equation (2.3)):

$$g_W(\tau|F, \theta) = \int_{\mu}^{\infty} (\gamma - \mu) p(\xi = \xi_0 + \mu\tau, \gamma|\xi_0, \gamma_0; \tau) d\gamma \quad (\text{A1.2})$$

Using the Bayes theorem, the probability $p(\xi, \gamma|\xi_0, \gamma_0; \tau)$ becomes:

$$p(\xi, \gamma|\xi_0, \gamma_0; \tau) = \frac{p(\xi, \gamma, \xi_0, \gamma_0; \tau)}{p(\xi_0, \gamma_0; \tau)} \quad (\text{A1.2a})$$

The process being uncorrelated involves:

$$p(\xi, \gamma|\xi_0, \gamma_0; \tau) = \frac{p(\xi, \xi_0) \cdot p(\gamma, \gamma_0)}{p(\xi_0, \gamma_0)} = \frac{p(\xi)p(\xi_0)p(\gamma)p(\gamma_0)}{p(\xi_0)p(\gamma_0)} = p(\xi)p(\gamma) \quad (\text{A1.2b})$$

Substituting equation (A1.2b) into (A1.2), the Wagner function $g_W(\tau|F, \theta)$ is:

$$g_W(\tau|F, \theta) = \mu \Lambda p(\xi) \quad \text{with} \quad \Lambda = \frac{1}{\mu} \int_{\mu}^{\infty} (\gamma - \mu) p(\gamma) d\gamma \quad (\text{A1.3})$$

Moreover $\xi = \xi_0 + \mu\tau$, thus:

$$\int_0^{\infty} g_W(\tau|F, \theta) d\tau = \mu \Lambda \int_0^{\infty} p(\xi_0 + \mu\tau) d\tau = \Lambda \int_{\xi_0}^{\infty} p(\xi) d\xi \quad (\text{A1.4})$$

Substituting equation (A1.4) into (A1.1), the shadowing function is given by:

$$S_W(\theta) = \left\{ \int_{-\infty}^{\infty} p(\xi_0) \cdot \exp \left[-\Lambda \int_{\xi_0}^{\infty} p(\xi) d\xi \right] d\xi_0 \right\} \int_{-\infty}^{\mu} p(\gamma_0) d\gamma_0 \quad (\text{A1.5})$$

Set P be a primitive of $p(h)$:

$$P = \int p(h) dh \quad (\text{A1.6})$$

thus

$$S_W(\theta) = \left[e^{-\Lambda P(\infty)} \int_{-\infty}^{\infty} dP(\xi_0) \cdot e^{\Lambda P(\xi_0)} \right] \int_{-\infty}^{\mu} p(\gamma_0) d\gamma_0 \quad (\text{A1.6a})$$

The integration over ξ_0 gives:

$$S_W(\theta) = \left[\frac{1 - e^{-\Lambda\{P(\infty) - P(-\infty)\}}}{\Lambda} \right] \int_{-\infty}^{\mu} p(\gamma_0) d\gamma_0 \quad (\text{A1.6b})$$

Moreover

$$P(\infty) - P(-\infty) = \int_{-\infty}^{\infty} p(h) dh = 1 \quad (\text{A1.6c})$$

The Wagner shadowing function is then:

$$S_W(\theta) = \Lambda' \times \frac{1 - e^{-\Lambda}}{\Lambda} \quad \Lambda = \frac{1}{\mu} \int_{\mu}^{\infty} (\gamma - \mu) p(\gamma) d\gamma \quad \Lambda' = \int_{-\infty}^{\mu} p(\gamma) d\gamma \quad (\text{A1.7})$$

A1.2 Smith

The Smith conditional probability is given by (equation (2.4)):

$$g_S(\tau|F, \theta) = g_W(\tau|F, \theta) / \left[\int_{-\infty}^{\infty} d\gamma \int_{-\infty}^{\xi_0 + \mu\tau} p(\xi, \gamma|\xi_0, \gamma_0; \tau) d\xi \right] \quad (\text{A1.8})$$

Substituting equations (A1.2b) and (A1.3) into (A1.8) we have:

$$g_S(\tau|F, \theta) = \mu\Lambda p(\xi) / \int_{-\infty}^{\xi} p(\xi_1) d\xi_1 \quad (\text{A1.9})$$

Making the variable transformation we obtain:

$$\begin{aligned} \int_0^{\infty} g_S(\tau|F, \theta) d\tau &= \mu\Lambda \int_0^{\infty} \left\{ p(\xi) / \left[\int_{-\infty}^{\xi} p(\xi_1) d\xi_1 \right] \right\} d\tau \\ &= \Lambda \int_{\xi_0}^{\infty} \left\{ p(\xi) / \left[\int_{-\infty}^{\xi} p(\xi_1) d\xi_1 \right] \right\} d\xi \end{aligned} \quad (\text{A1.10})$$

Using equation (A1.6), the integration over τ gives:

$$\begin{aligned} \int_0^{\infty} g_S(\tau|F, \theta) d\tau &= \Lambda \int_{\xi_0}^{\infty} dP(\xi) / [P(\xi) - P(-\infty)] \\ &= -\ln |P(\xi_0) - P(-\infty)|^{\Lambda} \end{aligned} \quad (\text{A1.11})$$

Substituting equation (A1.11) into (A1.1), the Smith shadowing function is given by:

$$S_S(\theta) = \left\{ \int_{-\infty}^{\infty} p(\xi_0) \cdot |P(\xi_0) - P(-\infty)|^{\Lambda} d\xi_0 \right\} \int_{-\infty}^{\mu} p(\gamma_0) d\gamma_0 \quad (\text{A1.12})$$

The integration over ξ_0 gives:

$$S_S(\theta) = \left\{ \frac{1}{\Lambda + 1} [P(\xi_0) - P(-\infty)]_{-\infty}^{\infty} \right\} \int_{-\infty}^{\mu} p(\gamma_0) d\gamma_0 \quad (\text{A1.12a})$$

Using equation (A1.6c), we show that:

$$S_S(\theta) = \Lambda' / (\Lambda + 1) \quad (\text{A1.13})$$

APPENDIX 2. THE RICCIARDI-SATO SHADOWING FUNCTION OF THE UNCORRELATED PROCESS FOR AN INFINITE SURFACE

In this appendix, the Ricciardi-Sato shadowing function is determined for an uncorrelated process, and for an infinite observation length (equation (2.6)):

$$S(\theta) = \int_{-\infty}^{\infty} \int_{-\infty}^{\mu} p(\xi_0, \gamma) \exp \left(- \int_0^{\infty} g(l|F, \theta) dl \right) d\xi_0 d\gamma_0 \quad (\text{A2.1})$$

A2.1 Introduction

The Ricciardi-Sato function $g_R(l|F, \theta)$ is defined by (2.5):

$$g_R(l|F, \theta) = \sum_{n=1}^{\infty} (-1)^{n-1} I_n(l|F, \theta) \quad (\text{A2.2})$$

$$\left\{ \begin{array}{l} I_1(l|F, \theta) = W_1(l|F, \theta) \\ I_n(l|F, \theta) = \int_0^l dl_1 \int_{l_1}^l dl_2 \cdots \int_{l_{n-2}}^l W_n(l, l_1, \dots, l_{n-1}|F, \theta) dl_{n-1} \\ W_n(l, l_1, \dots, l_{n-1}|F, \theta) = \int_{\mu}^{\infty} d\gamma_1 \int_{\mu}^{\infty} d\gamma_2 \cdots \int_{\mu}^{\infty} d\gamma_n \\ \prod_{i=1}^n (\gamma_i - \mu) \cdot p_{2n+2}(\vec{S}, \vec{G}|\xi_0, \gamma_0; l) \end{array} \right. \quad (\text{A2.2a})$$

Using the Bayes theorem, the probability density $p_{2n+2}(\vec{S}, \vec{G}|\xi_0, \gamma_0; l)$ is:

$$p_{2n+2}(\vec{S}, \vec{G}|\xi_0, \gamma_0; l) = p_{2n+2}(\vec{S}, \vec{G}, \xi_0, \gamma_0; l) / p(\xi_0, \gamma_0; l) \quad (\text{A2.3})$$

For an uncorrelated gaussian process $p_{2n+2}(\vec{S}, \vec{G}|\xi_0, \gamma_0; l)$ is given by:

$$\begin{aligned} p_{2n+2}(\vec{S}, \vec{G}|\xi_0, \gamma_0; l) &= p_{2n}(\vec{S}, \vec{G}; l) \\ &= \frac{1}{(2\pi)^n (-a_2 a_0)^{n/2}} \sum_{i=1}^n \exp\left(-\frac{\xi_0 + \mu l_i}{2a_0} + \frac{\gamma_i^2}{2a_2}\right) \end{aligned} \quad (\text{A2.3a})$$

Physically a_0 represents the height variance and $-a_2 = \sigma^2$ the slope variance. Substituting equation (A2.3a) into W_n , we have:

$$\begin{aligned} W_n &= \exp\left[-\frac{1}{2a_0} \sum_{i=1}^n (\xi_0 + \mu l_i)^2\right] \\ &\cdot \left\{ \frac{1}{2\pi \sqrt{|a_2| a_0}} \int_{\mu}^{\infty} (\gamma - \mu) \cdot \exp\left[-\frac{\gamma^2}{2|a_2|}\right] d\gamma \right\}^n \end{aligned} \quad (\text{A2.4})$$

If $a_2 < 0$ is verified then the integral is convergent. The integration over γ of W_n gives:

$$\begin{aligned} W_n &= \exp\left[-\frac{1}{2a_0} \sum_{i=1}^n (\xi_0 + \mu l_i)^2\right] \left[\frac{\mu \Lambda}{\sqrt{2\pi a_0}}\right]^n \\ \text{with} & \quad (\text{A2.5}) \\ & \begin{cases} \Lambda = \left[\frac{e^{-v^2} - v\sqrt{\pi}\text{erfc}(v)}{2v\sqrt{\pi}}\right] \\ v = \mu/(\sigma\sqrt{2}) \end{cases} \end{aligned}$$

A2.2 Calculus of the Integral I_n

Case $n = 1$

The case $n = 1$, I_1 is:

$$I_1 = W_1 = \exp\left[-\frac{\xi_1^2}{2a_0}\right] \left[\frac{\mu\Lambda}{\sqrt{2\pi a_0}}\right] \quad \text{with} \quad \xi_1 = \xi_0 + \mu l_0 = \xi_0 + \mu l \quad (\text{A2.6})$$

Case $n = 2$

$$\begin{aligned} I_2 &= \int_0^l W_2 dl_1 \\ &= \left[\frac{\mu\Lambda}{\sqrt{2\pi a_0}}\right]^2 \int_0^l \exp\left[-\frac{(\xi_0 + \mu l)^2}{2a_0} - \frac{(\xi_0 + \mu l_1)^2}{2a_0}\right] dl_1 \\ &\quad \left[\frac{\mu\Lambda}{\sqrt{2\pi a_0}}\right]^2 \exp\left[-\frac{(\xi_0 + \mu l)^2}{2a_0}\right] \int_0^l \exp\left[-\frac{(\xi_0 + \mu l_1)^2}{2a_0}\right] dl_1 \quad (\text{A2.7}) \end{aligned}$$

Setting $u = (\xi_0 + \mu l_1)/\sqrt{2a_0}$, the integration of I_2 gives:

$$I_2 = \left[\frac{\mu\Lambda}{\sqrt{2\pi a_0}}\right] \exp\left[-\frac{(\xi_0 + \mu l)^2}{2a_0}\right] \left\{ \frac{\Lambda}{2} \left[\operatorname{erf}\left(\frac{\xi_0 + \mu l}{\sqrt{2a_0}}\right) - \operatorname{erf}\left(\frac{\xi_0}{\sqrt{2a_0}}\right) \right] \right\} \quad (\text{A2.7a})$$

Case $n = 3$

$$I_3 = \int_0^l dl_1 \left[\int_{l_1}^l W_3 dl_2 \right] \quad (\text{A2.8})$$

* Integration over l_2 :

$$\int_{l_1}^l W_3 dl_2 = \left[\frac{\mu\Lambda}{\sqrt{2\pi a_0}}\right]^3 \exp\left[-\frac{\xi_1^2 + \xi_2^2}{2a_0}\right] \int_{l_1}^l \exp\left[-\frac{(\xi_0 + \mu l_2)^2}{2a_0}\right] dl_2 \quad (\text{A2.8a})$$

or

$$\left[\frac{\mu\Lambda}{\sqrt{2\pi a_0}}\right] \int_{l_1}^l \exp\left[-\frac{(\xi_0 + \mu l_2)^2}{2a_0}\right] dl_2 = \frac{\Lambda}{2} \left[\operatorname{erf}\left(\frac{\xi_0 + \mu l}{\sqrt{2a_0}}\right) - \operatorname{erf}\left(\frac{\xi_0 + \mu l_1}{\sqrt{2a_0}}\right) \right] \quad (\text{A2.8b})$$

so

$$\int_{l_1}^l W_3 dl_2 = \left[\frac{\mu \Lambda}{\sqrt{2\pi a_0}} \right]^2 \exp \left[-\frac{\xi_1^2 + \xi_2^2}{2a_0} \right] \frac{\Lambda}{2} \left[\operatorname{erf} \left(\frac{\xi_0 + \mu l}{\sqrt{2a_0}} \right) - \operatorname{erf} \left(\frac{\xi_0 + \mu l_1}{\sqrt{2a_0}} \right) \right] \quad (\text{A2.8c})$$

* Integration over l_1 :

Substituting equation (A2.8c) into (A2.8) we have:

$$I_3 = \left[\frac{\mu \Lambda}{\sqrt{2\pi a_0}} \right]^2 \frac{\Lambda}{2} \exp \left[-\frac{\xi_1^2}{2a_0} \right] \int_0^l \exp \left[-\frac{(\xi_0 + \mu l_1)^2}{2a_0} \right] \left[\operatorname{erf} \left(\frac{\xi_0 + \mu l}{\sqrt{2a_0}} \right) - \operatorname{erf} \left(\frac{\xi_0 + \mu l_1}{\sqrt{2a_0}} \right) \right] dl_1 \quad (\text{A2.8d})$$

Setting $u = (\xi_0 + \mu l_1)/\sqrt{2a_0}$ we have:

$$\begin{aligned} & \int_0^l e^{-\frac{(\xi_0 + \mu l_1)^2}{2a_0}} \left[\operatorname{erf} \left(\frac{\xi_0 + \mu l}{\sqrt{2a_0}} \right) - \operatorname{erf} \left(\frac{\xi_0 + \mu l_1}{\sqrt{2a_0}} \right) \right] dl_1 \\ &= \frac{\sqrt{2a_0}}{\mu} \int_{\frac{\xi_0}{\sqrt{2a_0}}}^{\frac{\xi_0 + \mu l}{\sqrt{2a_0}}} e^{-u^2} \left[\operatorname{erf}(u) + \operatorname{erf} \left(\frac{\xi_0 + \mu l}{\sqrt{2a_0}} \right) \right] du \quad (\text{A2.8e}) \end{aligned}$$

Moreover

$$\int_{u_1}^{u_2} \exp[-u^2] \operatorname{erf}(u) du = \frac{\sqrt{\pi}}{4} [\operatorname{erf}^2(u_2) - \operatorname{erf}^2(u_1)] \quad (\text{A2.8f})$$

Substituting equation (A2.8f) into (A2.8e), integral (A2.8e) becomes:

$$\begin{aligned} & \frac{\sqrt{2a_0}}{\mu} \left\{ \frac{\pi}{4} \left[\operatorname{erf}^2 \left(\frac{\xi_0}{\sqrt{2a_0}} \right) - \operatorname{erf}^2 \left(\frac{\xi_0 + \mu l}{\sqrt{2a_0}} \right) \right] \right. \\ & \left. + \operatorname{erf} \left(\frac{\xi_0 + \mu l}{\sqrt{2a_0}} \right) \frac{\pi}{2} \left[\operatorname{erf} \left(\frac{\xi_0 + \mu l}{\sqrt{2a_0}} \right) - \operatorname{erf} \left(\frac{\xi_0}{\sqrt{2a_0}} \right) \right] \right\} \\ &= \frac{\sqrt{\pi a_0}}{2\sqrt{2}\mu} \left[\operatorname{erf} \left(\frac{\xi_0}{\sqrt{2a_0}} \right) - \operatorname{erf} \left(\frac{\xi_0 + \mu l}{\sqrt{2a_0}} \right) \right]^2 \quad (\text{A2.8g}) \end{aligned}$$

Using equation (A2.8g) and (A2.8d) we obtain:

$$\begin{aligned} I_3 &= \left[\frac{\mu\Lambda}{\sqrt{2\pi a_0}} \right]^2 \frac{\Lambda}{2} \exp \left[-\frac{\xi_1^2}{2a_0} \right] \frac{\sqrt{\pi a_0}}{2\sqrt{2}\mu} \left[\operatorname{erf} \left(\frac{\xi_0}{\sqrt{2a_0}} \right) - \operatorname{erf} \left(\frac{\xi_0 + \mu l}{\sqrt{2a_0}} \right) \right]^2 \\ &= \left[\frac{\mu\Lambda}{\sqrt{2\pi a_0}} \right] \exp \left[-\frac{\xi_1^2}{2a_0} \right] \frac{1}{2} \left\{ \frac{\Lambda}{2} \left[\operatorname{erf} \left(\frac{\xi_0}{\sqrt{2a_0}} \right) - \operatorname{erf} \left(\frac{\xi_0 + \mu l}{\sqrt{2a_0}} \right) \right] \right\}^2 \end{aligned} \quad (\text{A2.8h})$$

Case $n = 4$

$$I_4 = \int_0^l dl_1 \left\{ \int_{l_1}^l W_3 \left[\int_{l_2}^l W_4 dl_3 \right] dl_2 \right\} \quad (\text{A2.9})$$

Applying the same reasoning as previously we show:

$$I_4 = \left[\frac{\mu\Lambda}{\sqrt{2\pi a_0}} \right] \exp \left[-\frac{\xi_1^2}{2a_0} \right] \frac{1}{6} \left\{ \frac{\Lambda}{2} \left[\operatorname{erf} \left(\frac{\xi_0 + \mu l}{\sqrt{2a_0}} \right) - \operatorname{erf} \left(\frac{\xi_0}{\sqrt{2a_0}} \right) \right] \right\}^3 \quad (\text{A2.9a})$$

$n \geq 1$ **integer**

Generalizing equations (A2.6), (A2.7a), (A2.8h), (A2.9a), we prove:

$$\begin{cases} I_1 = \left[\frac{\mu\Lambda}{\sqrt{2\pi a_0}} \right] \exp \left[-\frac{(\xi_0 + \mu l)^2}{2a_0} \right] & n = 1 \\ I_n = \left[\frac{\mu\Lambda}{\sqrt{2\pi a_0}} \right] \exp \left[-\frac{(\xi_0 + \mu l)^2}{2a_0} \right] \frac{X^{n-1}}{(n-1)!} & n > 1 \\ \text{with } X = \frac{\Lambda}{2} \left[\operatorname{erf} \left(\frac{\xi_0 + \mu l}{\sqrt{2a_0}} \right) - \operatorname{erf} \left(\frac{\xi_0}{\sqrt{2a_0}} \right) \right] \end{cases} \quad (\text{A2.10})$$

2.3 Calculus of the Shadowing Function

Using equation (A2.10) and (A2.2), the function g_R becomes:

$$\begin{aligned} g_R &= \left[\frac{\mu\Lambda}{\sqrt{2\pi a_0}} \right] \exp \left[-\frac{(\xi_0 + \mu l)^2}{2a_0} \right] \\ &\quad \cdot \left[1 - X + \frac{X^2}{2} - \frac{X^3}{6} + \dots + (-1)^p \frac{X^p}{p!} \right] \\ &= g_0 \cdot \exp(-X) \quad \text{with } g_0 = \left[\frac{\mu\Lambda}{\sqrt{2\pi a_0}} \right] \exp \left[-\frac{(\xi_0 + \mu l)^2}{2a_0} \right] \end{aligned} \quad (\text{A2.11})$$

Substituting equation (A2.11) into (A2.1), and making the integration over γ_0 , the Ricciardi-Sato shadowing function $S_R(\theta)$ for an uncorrelated process is given by:

$$S_R(\theta) = \frac{1}{\sqrt{2\pi a_0}} \left[1 - \frac{1}{2} \operatorname{erfc}(v) \right] \int_{-\infty}^{\infty} \exp\left(-\frac{\xi_0^2}{2a_0}\right) \exp\left[-\int_0^{\infty} g_0 \cdot \exp(-X) dl\right] d\xi_0 \quad (\text{A2.12})$$

with erfc the complementary error function. Setting $u = (\xi_0 + \mu l)/(\sqrt{2a_0})$, the integral over l is:

$$\int_0^{\infty} g_0 \cdot \exp(-X) dl = \frac{\Lambda}{\sqrt{\pi}} \exp\left[\frac{\Lambda}{2} \operatorname{erf}(v)\right] \int_{\frac{\xi_0}{\sqrt{2a_0}}}^{\infty} \exp\left[-\frac{\Lambda}{2} \operatorname{erf}(u) - u^2\right] du \quad (\text{A2.13})$$

or

$$\int \exp\left[-\frac{\Lambda}{2} \operatorname{erf}(u) - u^2\right] du = -\frac{\sqrt{\pi}}{\Lambda} \exp\left[-\frac{\Lambda}{2} \operatorname{erf}(u)\right] \quad (\text{A2.13a})$$

so

$$\int_0^{\infty} g_0 \cdot \exp(-X) dl = 1 - \exp\left[-\frac{\Lambda}{2} \operatorname{erfc}\left(\frac{\xi_0}{\sqrt{2a_0}}\right)\right] \quad (\text{A2.13b})$$

Setting $x = \xi_0/\sqrt{2a_0}$ and Substituting equation (A2.13b) into (A2.12), the shadowing function is given by:

$$S_R(\theta) = \frac{1}{\sqrt{\pi}} \left[1 - \frac{1}{2} \operatorname{erfc}(v) \right] \int_{-\infty}^{\infty} e^{-x^2} e^{-1+\exp[-\frac{\Lambda}{2} \operatorname{erfc}(x)]} dx \quad (\text{A2.14})$$

Making the variable transformation $z = -\Lambda \operatorname{erfc}(x)/2$, the integral (A2.14) becomes:

$$S_R(\theta) = \left[1 - \frac{1}{2} \operatorname{erfc}(v) \right] \frac{e^{-1}}{\Lambda} \int_{-\Lambda}^0 e^{\exp(z)} dz = \frac{e^{-1}}{\Lambda} \left[1 - \frac{1}{2} \operatorname{erfc}(v) \right] \int_{e^{-\Lambda}}^1 \frac{e^t}{t} dt \quad (\text{A2.14a})$$

with $t = \exp(z)$. The Ricciardi-Sato shadowing function is then:

$$\begin{cases} S_R(v) = \left[1 - \frac{\operatorname{erfc}(v)}{2} \right] \left[\frac{E_1(-e^{-\Lambda}) - E_1(-1)}{\Lambda e^1} \right] \\ E_1(x) = \int_1^\infty \frac{e^{-xt}}{y} dy = \int_{-x}^{-\infty} \frac{e^t}{t} dt \end{cases} \quad (\text{A2.15})$$

where E_1 is the exponential integral function.

APPENDIX 3. THE WAGNER CONDITIONAL PROBABILITY OF THE CORRELATED GAUSSIAN PROCESS

This appendix determines the Wagner conditional probability for a correlated gaussian process (equation (2.3)):

$$g_W(\tau|F, \theta) = \int_{\mu}^{\infty} (\gamma - \mu) p(\xi = \xi_0 + \mu\tau, \gamma|\xi_0, \gamma_0; \tau) d\gamma \quad (\text{A3.1})$$

A3.1 Calculus of the Probability Density

Using the Bayes theorem, we have:

$$p(\xi, \gamma|\xi_0, \gamma_0; \tau) = p(\xi, \gamma, \xi_0, \gamma_0; \tau) / p(\xi_0, \gamma_0) \quad (\text{A3.2})$$

For 4-dimensions gaussian process $p(\xi, \gamma, \xi_0, \gamma_0; \tau)$ is given by

$$p(\xi, \gamma|\xi_0, \gamma_0; \tau) = \frac{\sqrt{C_{11}C_{33} - C_{31}C_{13}}}{2\pi\sqrt{|[C]|}} e^{-\frac{1}{2}\vec{V}^T[C]^{-1}\vec{V} + \frac{1}{2}[\xi_0, \gamma_0] \begin{bmatrix} C_{11} & C_{13} \\ C_{31} & C_{33} \end{bmatrix}^{-1} \begin{bmatrix} \xi_0 \\ \gamma_0 \end{bmatrix}}$$

$$\text{with } \vec{V} = \begin{bmatrix} \xi_0 \\ \xi \\ \gamma_0 \\ \gamma \end{bmatrix} \quad (\text{A3.3})$$

and

$$[C] = \begin{bmatrix} [C_{HH}] & [C_{HP}] \\ [C_{PH}] & [C_{PP}] \end{bmatrix} \quad \text{with} \quad \begin{cases} C_{HH}^{ij} = \langle \xi_i(\tau_i) \xi_j(\tau_j) \rangle = R_0(\tau_i - \tau_j) \\ C_{PP}^{ij} = \langle \dot{\xi}_i(\tau_i) \dot{\xi}_j(\tau_j) \rangle = -R_2(\tau_i - \tau_j) \\ C_{HP}^{ij} = \langle \xi_i(\tau_i) \dot{\xi}_j(\tau_j) \rangle = -R_1(\tau_i - \tau_j) \\ C_{PH}^{ij} = \langle \dot{\xi}_i(\tau_i) \xi_j(\tau_j) \rangle = -R_1(\tau_j - \tau_i) \end{cases} \quad (\text{A3.3a})$$

R_0 is the autocorrelation function, R_1 its first derivative over τ , and R_2 its second derivative. $|[C]|$ is the determinant of the covariance matrix $[C]$. The autocorrelation function being even we have:

$$\begin{cases} R_0(-[l_i - l_j]) = R_0(l_i - l_j) & R_2(-[l_i - l_j]) = R_2(l_i - l_j) \\ R_1(-[l_i - l_j]) = -R_1(l_i - l_j) & R_1(0) = 0 \end{cases} \quad (\text{A3.3b})$$

The covariance matrix becomes with $\tau = l_2 - l_1$:

$$[C] = \begin{bmatrix} R_0(0) & R_0(-\tau) & -R_1(0) & -R_1(-\tau) \\ R_0(\tau) & R_0(0) & -R_1(\tau) & -R_1(0) \\ -R_1(0) & -R_1(\tau) & -R_2(0) & -R_2(-\tau) \\ -R_1(-\tau) & -R_1(0) & -R_2(\tau) & -R_2(0) \end{bmatrix} \\ = \begin{bmatrix} \omega^2 & R_0 & 0 & R_1 \\ R_0 & \omega^2 & -R_1 & 0 \\ 0 & -R_1 & \sigma^2 & -R_2 \\ R_1 & 0 & -R_2 & \sigma^2 \end{bmatrix} \quad (\text{A3.3c})$$

where ω^2 is the height variance equal to $R_0(0)$, and σ^2 the slope variance equal to $-R_2(0)$. Moreover we show that the inverse covariance matrix $[C]^{-1}$ is:

$$[C]^{-1} = \frac{1}{|[C]|} \begin{bmatrix} C_{i11} & C_{i12} & C_{i13} & C_{i14} \\ C_{i12} & C_{i11} & -C_{i14} & -C_{i13} \\ C_{i13} & -C_{i14} & C_{i33} & C_{i34} \\ C_{i14} & -C_{i13} & C_{i34} & C_{i33} \end{bmatrix} \quad (\text{A3.4})$$

with:

$$\begin{cases} C_{i11} = \omega^2 (\sigma^4 - R_2^2) - R_1^2 \sigma^2 \\ C_{i12} = R_0 (R_2^2 - \sigma^4) - R_1^2 R_2 \\ C_{i13} = -R_1 (R_0 \sigma^2 + \omega^2 R_2) \\ C_{i14} = R_1 (R_1^2 - R_0 R_2 - \omega^2 \sigma^2) \end{cases} \quad (\text{A3.5})$$

$$\begin{cases} C_{i33} = \sigma^2 (\omega^4 - R_0^2) - R_1^2 \omega^2 \\ C_{i34} = R_2 (\omega^4 - R_0^2) + R_1^2 R_0 \\ |[C]| = (C_{i33}^2 - C_{i34}^2) / (\omega^4 - R_0^2) \end{cases} \quad (\text{A3.6})$$

Substituting equations (A3.4) and (A3.3c) into (A3.3) we obtain:

$$\begin{aligned}
 p(\xi, \gamma | \xi_0, \gamma_0; \tau) &= \frac{\sigma\omega}{2\pi\sqrt{|[C]|}} \\
 &\times \exp \left[-\frac{C_{i11}(\xi_0^2 + \xi^2) + C_{i33}(\gamma_0^2 + \gamma^2)}{2|[C]|} + \frac{\xi_0^2}{2\omega^2} + \frac{\gamma_0^2}{2\sigma^2} \right. \\
 &\quad \left. - \frac{\left(2C_{i12}\xi_0\xi + 2C_{i34}\gamma_0\gamma \right. \right. \\
 &\quad \left. \left. + 2C_{i13}(\xi_0\gamma_0 - \xi\gamma) + 2C_{i14}(\xi_0\gamma - \xi\gamma_0) \right)}{2|[C]|} \right]
 \end{aligned} \tag{A3.7}$$

A3.2 Calculus of the Conditional Probability

Using equations (A3.7) and (A3.1), the Wagner conditional probability is given by:

$$g_W(\tau | F, \theta) = \frac{\sigma\omega}{2\pi\sqrt{|[C]|}} \int_{\mu}^{\infty} (\gamma - \mu) \exp(-A\gamma^2 - 2B\gamma - D) d\gamma \tag{A3.8}$$

with

$$\left\{ \begin{array}{l} A = \frac{C_{i33}}{2|[C]|} \quad B = \frac{\xi_0 C_{i14} - \xi C_{i13} + \gamma_0 C_{i34}}{2|[C]|} \\ D = \frac{(\xi_0^2 + \xi^2) C_{i11} + 2\xi_0 \xi C_{i12} + 2\gamma_0 (\xi_0 C_{i13} - \xi C_{i14}) + \gamma_0^2 C_{i33}}{2|[C]|} \\ \quad - \frac{\xi_0^2}{2\omega^2} - \frac{\gamma_0^2}{2\sigma^2} \end{array} \right. \tag{A3.8a}$$

or:

$$\begin{aligned}
 &\int_{\mu}^{\infty} (\gamma - \mu) e^{-A\gamma^2 - 2B\gamma - D} d\gamma \\
 &= \frac{e^{-D - \mu(\mu A + 2B)}}{2A} \cdot \left[1 - e^{\frac{(B + \mu A)^2}{A}} \sqrt{\pi} \frac{B + \mu A}{\sqrt{A}} \operatorname{erfc} \left(\frac{B + \mu A}{\sqrt{A}} \right) \right]
 \end{aligned} \tag{A3.9}$$

so:

$$g_W(\tau|F, \theta) = \frac{\sigma\omega \exp[-D - \mu(\mu A + 2B)]}{4\pi A \sqrt{||[C]||}} \cdot \left[1 - e^{\frac{(B+\mu A)^2}{A}} \sqrt{\pi} \frac{B + \mu A}{\sqrt{A}} \operatorname{erfc} \left(\frac{B + \mu A}{\sqrt{A}} \right) \right] \quad (\text{A3.10})$$

If the conditions $A > 0$ and $||[C]|| > 0$ are satisfied then $g_W(\tau|F, \theta)$ is real.

APPENDIX 4. THE SMITH CONDITIONAL PROBABILITY OF THE CORRELATED GAUSSIAN PROCESS

This appendix determines the Smith conditional probability for a correlated gaussian process (equation (2.4)):

$$g_S(\tau|F, \theta) = \frac{g_W(\tau|F, \theta)}{\int_{-\infty}^{\infty} d\gamma \int_{-\infty}^{\xi_0 + \mu\tau} p(\xi, \gamma | \xi_0, \gamma_0; \tau) d\xi} \quad (\text{A4.1})$$

Using equation (A3.10) we have:

$$g_W(\tau|F, \theta) = \frac{\sigma\omega \exp[-D - \mu(\mu A + 2B)]}{4\pi A \sqrt{||[C]||}} \cdot \left[1 - e^{\frac{(B+\mu A)^2}{A}} \sqrt{\pi} \frac{B + \mu A}{\sqrt{A}} \operatorname{erfc} \left(\frac{B + \mu A}{\sqrt{A}} \right) \right] \quad (\text{A4.2})$$

and the denominator is:

$$I = \frac{\sigma\omega}{2\pi \sqrt{||[C]||}} \int_{-\infty}^{\xi_0 + \mu\tau} \left(\int_{-\infty}^{\infty} \exp[-A\gamma^2 - 2B\gamma - D] d\gamma \right) d\xi \quad (\text{A4.3})$$

$$I = \frac{\sigma\omega}{2\pi \sqrt{||[C]||}} \sqrt{\frac{\pi}{A}} \int_{-\infty}^{\xi_0 + \mu\tau} \exp \left(\frac{B^2}{A} - D \right) d\xi \quad (\text{A4.3a})$$

Setting:

$$\frac{B^2}{A} - D = -A_1\xi^2 - 2B_1\xi - D_1 \quad (\text{A4.4})$$

and applying the following relation:

$$\begin{aligned} & \int_{-\infty}^{\xi'} \exp(-A_1\xi^2 - 2B_1\xi - D_1) d\xi \\ &= \frac{1}{2} \sqrt{\frac{\pi}{A_1}} \exp\left(\frac{B_1^2}{A_1} - D_1\right) \left[\operatorname{erf}\left(\frac{A_1\xi' + B_1}{\sqrt{A_1}}\right) + 1 \right] \end{aligned} \quad (\text{A4.4a})$$

We show that the integration over ξ is:

$$I = \frac{\sigma\omega}{4\sqrt{|[C]|A_1A}} \exp\left(\frac{B_1^2}{A_1} - D_1\right) \left\{ \operatorname{erf}\left[\frac{A_1(\xi_0 + \mu\tau) + B_1}{\sqrt{A_1}}\right] + 1 \right\} \quad (\text{A4.5})$$

with:

$$\begin{cases} A_1 = \frac{C_{i11}C_{i33} - C_{i13}^2}{2C_{i33}|[C]|} \\ B_1 = \xi_0 \frac{C_{i12}C_{i33} + C_{i14}C_{i13}}{2C_{i33}|[C]|} + \gamma_0 \frac{C_{i13}C_{i34} - C_{i14}C_{i33}}{2C_{i33}|[C]|} \\ D_1 = \xi_0^2 \frac{C_{i11}C_{i33} - C_{i14}^2}{2C_{i33}|[C]|} + \gamma_0^2 \frac{C_{i33}^2 - C_{i34}^2}{2C_{i33}|[C]|} \\ \quad + 2\xi_0\gamma_0 \frac{C_{i13}C_{i33} - C_{i14}C_{i34}}{2C_{i33}|[C]|} - \frac{\xi_0^2}{2\omega^2} - \frac{\gamma_0^2}{2\sigma^2} \end{cases} \quad (\text{A4.5a})$$

Substituting equation (A4.5) and (A4.2) into (A4.1), the function $g_S(\tau)$ is given by:

$$\begin{aligned} g_S(\tau|F, \theta) &= \frac{1}{\pi} \sqrt{\frac{A_1}{A}} \\ & \frac{\exp[-D - \mu(\mu A + 2B)] \left[1 - e^{\frac{(B+\mu A)^2}{A}} \sqrt{\pi} \frac{B + \mu A}{\sqrt{A}} \operatorname{erfc}\left(\frac{B + \mu A}{\sqrt{A}}\right) \right]}{\exp\left(\frac{B_1^2}{A_1} - D_1\right) \left\{ \operatorname{erf}\left[\frac{A_1(\xi_0 + \mu\tau) + B_1}{\sqrt{A_1}}\right] + 1 \right\}} \end{aligned} \quad (\text{A4.6})$$

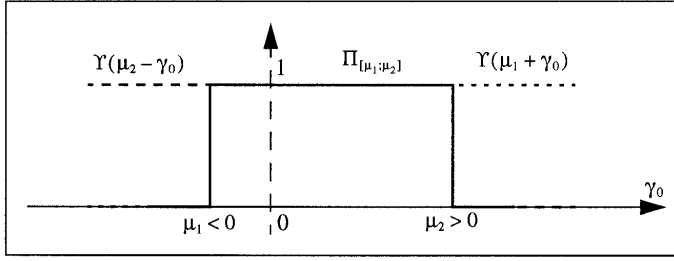


Figure 5A.1 Definition of the pulse function.

APPENDIX 5. THE SMITH UNCORRELATED BISTATIC SHADOWING FUNCTION FOR AN INFINITE SURFACE

The Smith uncorrelated monostatic shadowing function in the observation direction θ is given by (equations (2.16a) into (2.1) with $L_0 = \infty$):

$$S_S(\theta|F) = \Upsilon(\mu - \gamma_0) \cdot \left[1 - \frac{1}{2} \operatorname{erfc}(h_0) \right]^{\Lambda(v)} \quad (\text{A5.1})$$

Cases (a): $\theta_2 \in [0; \pi/2]$

Substituting equation (A5.1) into (2.31), we have:

$$\begin{aligned} S_S(\theta_1, \theta_2|F) &= S_S(\theta_1|F) S_S(\theta_2|F) \\ &= \Upsilon(\mu_1 + \gamma_0) \left[1 - \frac{\operatorname{erfc}(h)}{2} \right]^{\Lambda(|v_1|)} \Upsilon(\mu_2 - \gamma_0) \left[1 - \frac{\operatorname{erfc}(h)}{2} \right]^{\Lambda(v_2)} \end{aligned} \quad (\text{A5.2})$$

We note that in the Heaviside function $\Upsilon(\mu_1 + \gamma_0)$, the sign in front of γ_0 is positive because the emitter is defined by $y < 0$. Or figure A5.1:

$$\Upsilon(\mu_1 + \gamma_0) \cdot \Upsilon(\mu_2 - \gamma_0) = \Pi_{[\mu_1; \mu_2]} \quad (\text{A5.3})$$

with $\Pi_{[\mu_1; \mu_2]}$ is the pulse function of bandwidth $[\mu_1; \mu_2]$ ($\mu_1 < 0$ and $\mu_2 > 0$). Using equations (A5.3) and (A5.2), the shadowing function becomes:

$$S_S(\theta_1, \theta_2|F) = \Pi_{[\mu_1; \mu_2]} \cdot \left[1 - \frac{1}{2} \operatorname{erfc}(h) \right]^{\Lambda(|v_1|) + \Lambda(v_2)} \quad (\text{A5.4})$$

Substituting equation (A5.4) into (2.32), the average shadowing function is given by :

$$S_S(\theta_1, \theta_2) = \frac{1}{2\pi\sigma\omega} \int_{-\infty}^{\infty} \int_{-|\mu_1|}^{\mu_2} \left[1 - \frac{1}{2} \operatorname{erfc}(h) \right]^{\Lambda(|v_1|) + \Lambda(v_2)} \cdot \exp\left(-\frac{\xi_0^2}{2\omega^2} - \frac{\gamma_0^2}{2\sigma^2}\right) d\xi_0 d\gamma_0 \quad (\text{A5.5})$$

The integration gives:

$$S_S(\theta_1, \theta_2) = \frac{1 - \frac{1}{2} [\operatorname{erfc}(|v_1|) + \operatorname{erfc}(v_2)]}{\Lambda(|v_1|) + \Lambda(v_2) + 1} \quad (\text{A5.6})$$

Conclusion

The cases (b) and (c) are known monostatic cases (equation (2.22a)) involving the bistatic uncorrelated shadowing function is the following:

$$S_S(v_1, v_2) = \begin{cases} \frac{1 - \frac{1}{2} [\operatorname{erfc}(v_1) + \operatorname{erfc}(v_2)]}{\Lambda_1 + \Lambda_2 + 1} & \text{for } 0 \leq v_2 < \infty \\ \frac{1 - \frac{1}{2} [\operatorname{erfc}(v_2)]}{\Lambda_2 + 1} & \text{for } -v_1 \leq -v_2 < 0 \\ \frac{1 - \frac{1}{2} [\operatorname{erfc}(v_1)]}{\Lambda_1 + 1} & \text{for } -\infty \leq -v_2 < -v_1 \end{cases} \quad (\text{A5.7})$$

$$\text{with } \begin{cases} v_i = \frac{\cot(|\theta_i|)}{\sqrt{2}\sigma} \\ \Lambda_i = \left[e^{-v_i^2} - v_i \sqrt{\pi} \operatorname{erfc}(v_i) \right] / (2v_i \sqrt{\pi}) \end{cases} \quad i = \{1, 2\} \quad (\text{A5.7a})$$

APPENDIX 6. THE SMITH TWO-DIMENSIONAL CONDITIONAL PROBABILITY OF THE CORRELATED GAUSSIAN PROCESS

This appendix determines The Smith two-dimensional conditional probability $g_S(R, \phi | \{\xi_0, \gamma_{0X}\}, \theta)$ of the correlated gaussian process

(equation (2.4)). It is equal to:

$$g_S = \frac{\int_{-\infty}^{\infty} (\gamma_X - \mu) p(\xi, \gamma_X | \xi_0, \gamma_{0X}; R, \phi) d\gamma_X}{\int_{-\infty}^{\infty} d\gamma_X \left[\int_{-\infty}^{\xi_0 + \mu\tau} p(\xi, \gamma_X | \xi_0, \gamma_{0X}; R, \phi) d\xi \right]} = \frac{I_1}{I_2} \quad (\text{A6.1})$$

with:

$$\begin{aligned} p(\xi, \gamma_X | \xi_0, \gamma_{0X}; R, \phi) &= \frac{\omega\sigma_X \sqrt{1-\rho^2}}{2\pi\sqrt{E/\sigma_Y^2}} \exp\left(\frac{\xi_0^2}{2\omega^2} + \frac{\gamma_{0X}^2}{2\sigma_X^2} - \frac{a_1\xi_0^2 + a_2\xi^2 + a_9\gamma_X^2 + a_{10}\gamma_{0X}^2}{2|[C^{XY}]|} \right. \\ &\quad \left. - \frac{a_3\xi_0\xi + a_4\gamma_{0X}\gamma_X + a_5\xi_0\gamma_{0X} - a_6\xi\gamma_X + a_7\xi_0\gamma_X - a_8\xi\gamma_{0X}}{|[C^{XY}]|} \right) \end{aligned} \quad (\text{A6.1a})$$

We apply the same way as appendix 4. We can write:

$$p(\xi, \gamma_X | \xi_0, \gamma_{0X}; R, \phi) = \frac{\omega\sigma_X \sqrt{1-\rho^2}}{2\pi\sqrt{E/\sigma_Y^2}} \exp(-A_X\gamma_X^2 - 2B_X\gamma_X - D_X) \quad (\text{A6.2})$$

with

$$\left\{ \begin{aligned} A_X &= \frac{a_9}{2|[C^{XY}]|} & B_X &= \frac{a_7\xi_0 - a_9\xi + a_4\gamma_{0X}}{2|[C^{XY}]|} \\ D_X &= \frac{a_1\xi_0^2 + a_2\xi^2 + 2a_3\xi_0\xi + 2a_5\xi_0\gamma_{0X} - 2a_8\xi\gamma_{0X} + a_{10}\gamma_{0X}^2}{2|[C^{XY}]|} \\ & & & - \frac{\xi_0^2}{2\omega^2} - \frac{\gamma_{0X}^2}{2\sigma_X^2} \end{aligned} \right. \quad (\text{A6.2a})$$

The integration over γ_X gives for the numerator (equation (A3.9));

$$\begin{aligned} I_1 &= \frac{\omega\sigma_X \sqrt{1-\rho^2} \exp[-D_X - \mu(\mu A_X + 2B_X)]}{4\pi A_X \sqrt{E/\sigma_Y^2}} \\ &\quad \cdot \left[1 - e^{\frac{(B_X + \mu A)^2}{A}} \sqrt{\pi} \frac{B_X + \mu A_X}{\sqrt{A_X}} \operatorname{erfc}\left(\frac{B_X + \mu A_X}{\sqrt{A_X}}\right) \right] \end{aligned} \quad (\text{A6.3})$$

and for the numerator we have:

$$I_2 = \frac{\omega\sigma_X\sqrt{1-\rho^2}}{2\pi\sqrt{E/\sigma_Y^2}} \sqrt{\frac{\pi}{A_X}} \int_{-\infty}^{\xi_0+\mu R} \exp\left(\frac{B_X^2}{A_X} - D_X\right) d\xi \quad (\text{A6.4})$$

Setting:

$$\frac{B_X^2}{A_X} - D_X = -A_{1X}\xi^2 - 2B_{1X}\xi - D_{1X} \quad (\text{A6.5})$$

We show that the integration over ξ (equation (A4.4a)) is:

$$I_2 = \frac{\omega\sigma_X\sqrt{1-\rho^2}}{4\sqrt{A_{1X}A_XE/\sigma_Y^2}} \exp\left(\frac{B_{1X}^2}{A_{1X}} - D_{1X}\right) \cdot \left\{ \operatorname{erf}\left[\frac{A_{1X}(\xi_0 + \mu R) + B_{1X}}{\sqrt{A_{1X}}}\right] + 1 \right\} \quad (\text{A6.6})$$

with:

$$\begin{cases} A_{1X} = \frac{a_2a_9 - a_6^2}{2a_9|[C^{XY}]|} \\ B_{1X} = \xi_0 \frac{a_3a_9 + a_6a_7}{2a_9|[C^{XY}]|} + \gamma_0 \frac{a_6a_4 - a_8a_9}{2a_9|[C^{XY}]|} \\ D_{1X} = \xi_0^2 \frac{a_1a_9 - a_7^2}{2a_9|[C^{XY}]|} + \gamma_0^2 \frac{a_{10}a_9 - a_4^2}{2a_9|[C^{XY}]|} + 2\xi_0\gamma_0 \frac{a_5a_9 - a_4a_7}{2a_9|[C^{XY}]|} \\ \quad - \frac{\xi_0^2}{2\omega^2} - \frac{\gamma_{0X}^2}{2\sigma_X^2} \end{cases} \quad (\text{A6.6a})$$

Substituting equation (A6.6) and (A6.3) into (A6.1), the function $g_S(R|F, \theta, \phi)$ is given by:

$$g_S = \frac{1}{\pi} \sqrt{\frac{A_{1X}}{A_X}} \left(\frac{\exp[-D_X - \mu(\mu A_X + 2B_X)] \times \left[1 - e^{\frac{(B_X + \mu A)^2}{A}} \sqrt{\pi} \frac{B_X + \mu A_X}{\sqrt{A_X}} \operatorname{erfc}\left(\frac{B_X + \mu A_X}{\sqrt{A_X}}\right) \right]}{\exp\left(\frac{B_{1X}^2}{A_{1X}} - D_{1X}\right) \left\{ \operatorname{erf}\left[\frac{A_{1X}(\xi_0 + \mu R) + B_{1X}}{\sqrt{A_{1X}}}\right] + 1 \right\}} \right) \quad (\text{A6.7})$$

ACKNOWLEDGMENT

The authors wish to acknowledge the contributions of my colleagues in the preparation of these three chapters, in particular Laurent Ferro-Famil.

REFERENCES

1. Oumansour, K., "Modélisation de la rétrodiffusion des sillages de navires, en imagerie radar polarimétrique," Thèse de doctorat, IRESTE, Nantes, France, 1996.
2. Gjessing, D. T., "Target adaptive matched. illumination radar: Principles and applications," *IEE Electromagnetic Waves Series*, Vol. 22, IEE eds, 1989.
3. Ulaby, F. T., R. K. Moore, and A. K. Fung, "Microwave remote sensing," *Theory to Applications*, Vol. 3, ARTECH House, INC., 1986.
4. Gérard, F., *La Houle, Théorie et Prévision, Météorologie Maritime*, Vol. 117, 4ème trimestre, 5–23, 1982.
5. Papoulis, *Probability, Random Variables, and Stochastic Processes*, 2nd edition, McGraw-Hill Book Company, 1984.
6. Yoshimori, K., K. Itoh, and Y. Ichioka, "Statistical formulation for an inhomogeneous random water surface a basis for optical remote sensing of oceans," *J. Opt. Soc. Am.*, Vol. 11, No. 2, 1994.
7. Appel, J. R., "An improved model of the ocean surface wave vector spectrum and its effects on radar backscatter," *J. of Geo. Res. Oceans*, Vol. 99, 1994.
8. Daout, F., "Etude de la dépolarisation des ondes centimétriques par une surface rugueuse—Application au domaine maritime," Thèse de Doctorat, IRESTE, Nantes, France, 1996.
9. Elfouhaily, T., B. Chapron, K. Katsaros, and D. Vandemark, "A unified directional spectrum for long and short wind-driven waves," *J. of Geo. Res.*, Vol. 102, No. C7, July 15, 1997.
10. Laurent, D., "Contribution à l'étude du comportement polarimétrique de la rétrodiffusion des océans," Thèse de doctorat, IRESTE, Nantes, France, 1993.
11. Wang, H. T., "Temporal and spatial simulations of random ocean waves," *Proceeding of the Fourth Offshore Mechanics and Arctic Engineering Symposium, ASME*, Vol. 1, 72–80, 1985.
12. Fung, A. K. and K. K. Lee, "A semi-empirical sea-spectrum model for scattering coefficient estimation," *IEEE Journal of Oceanic Engineering*, Vol. 7, No. 4, 1982.
13. Yoshimori, K., K. Itoh, and Y. Ichioka, "Optical characteristics

- of a wind-roughened water surface: a two dimensional theory," *Applied Optics*, Vol. 34, No. 27, 1995.
14. Abramowitz, M. and I. A. Segun, *Handbook of Mathematical Functions*, Dover Publications, 1972.
 15. Bourlier, C., J. Saillard, and G. Berginc, "Modeling of the spatial autocorrelation function of the heights of the sea," *Oceans'98 IEEE/OES Conference*, Vol. 2, 904–908, France, 1998.
 16. Olgilvy, J. A., *Theory of Wave Scattering from Random Rough Surfaces*, Bristol, Philadelphia and New York, Adam Hilger, 1991.
 17. Bourlier, C., J. Saillard, and G. Berginc, "Study of the slopes variances of the sea surface," *PIERS 98*, Vol. 2, 585, 1998, France, July 13–17, 1998.
 18. Cox, C. S. and W. H. Munk, "Statistics of the sea surface derived from sun glitter," *J. Mar. Res.*, 13, 198–226, 1954.
 19. Wagner, R. J., "Shadowing of randomly rough surfaces," *J. Opt. Soc. Am.*, Vol. 41, No. 1, 138–147, June 1966.
 20. Smith, B. G., "Lunar surface roughness, shadowing and thermal emission," *J. Geophysical Research*, Vol. 72, No. 16, 4059–4067, Août 1967.
 21. Smith, B. G., "Geometrical shadowing of a random rough surface," *IEEE Trans. Antennas Propagation*, Ap-15, No. 5, 668–671, Sept. 1967.
 22. Sancer, M. I., "Shadow-corrected electromagnetic scattering from a randomly rough surface," *IEEE Trans. Antennas Propagation*, Ap-17, No. 5, 577–585, 1969.
 23. Beckman, P., "Shadowing of random rough surfaces," *IEEE Trans. Antennas Propagation*, Ap-13, 384–388, May 1965.
 24. Brokelman, R. A. and T. Hagfors, "Note of the effect of shadowing on the backscattering of waves from a random rough surface," *IEEE Trans. Antennas Propagation*, Ap-14, 621–627, Sept. 1967.
 25. Ricciardi, L. M. and S. Sato, "On the evaluation of first passage time densities for Gaussian processes," *Signal Processing 11*, 339–357, 1986.
 26. Ricciardi, L. M. and S. Sato, "A note on first passage time problems for Gaussian processes and varying boundaries," *IEEE Transactions on Information Theory*, Vol. IT-29, No. 3, May 1983.
 27. Brown, G. S., "Shadowing by non-Gaussian random surfaces," *IEEE Transactions on Antennas*, Vol. AP-28, No. 6, November 1980.
 28. Kunt, M., "Techniques modernes de traitement numériques des signaux," *Collection Électricité*, 1991.
 29. de Coulon, F., "Théorie et traitement des signaux," *Dunod*, 1984.

30. Gaussorgues, G., "Thermographie infrarouge, principes, technologies," *Applications*, 1989.
31. Papini, F. and P. Gallet, "Thermographie infrarouge, image et mesure," *MASSON*, 1994.
32. Masuda, K., T. Takashima, and Y. Takayama, "Emissivity of pure and sea waters for the model sea surface in the infrared window regions," *Remote Sensing Enviro.*, 24, 313–329, 1988.
33. Saunders, P. M., "Shadowing on the ocean and the existence of the horizon," *J. Geophys. Res.*, 72, 4643–4649, 1967.
34. Wu, X. and W. L. Smith, "Emissivity of rough sea surface for 8–13 μm : modeling and verification," *Applied Optics*, Vol. 36, No. 12, April 1997.
35. Yoshimori, K., K. Itoh, and Y. Ichioka, "Thermal radiative and reflective characteristics of a wind-roughened water surface," *J. Opt. Soc. Am.*, Vol. 11, No. 6, June 1994.
36. Yoshimori, K., K. Itoh, and Y. Ichioka, "Optical characteristics of a wind-roughened water surface: a two-dimensional theory," *Applied Opt.*, Vol. 34, No. 27, September 1995.
37. Hale, G. M. and M. R. Querry, "Optical constants of water in the 200-nm to 200- μm wavelength region," *Appl. Opt.*, 12, 555–563, 1973.